Delft University of Technology

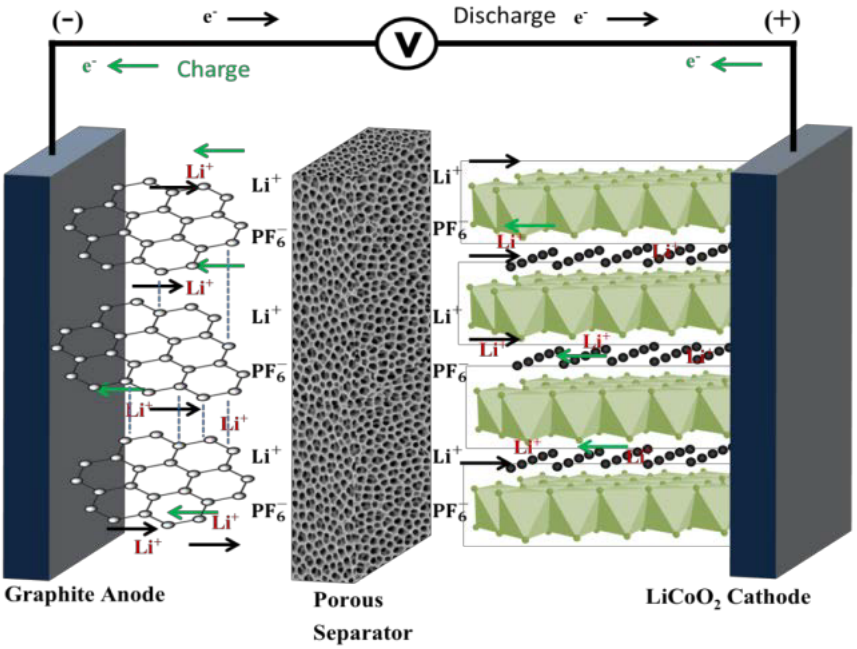

MSc Sustainable Energy technology

Master Thesis

Determining the effect of a varying carbon concentration on the cycling stability of a a-SiC$_x$:H anode

Tim Ammerlaan - 4472969

November 22, 2021, Delft

TU Delft

Determining the effect of a varying carbon concentration on the cycling stability of a a-SiC$_x$:H anode.

by

Tim Ammerlaan

to obtain the degree of Master of Science
at the Delft University of Technology,
to be defended publicly on Wednesday November 3, 2021 at 3:00 PM.

Student number:	4472969	
Project duration:	February 8, 2021 – November 3, 2021	
Thesis committee:	Dr. René van Swaaij	TU Delft, supervisor
	Prof. dr. ir. Arno Smets, ,	TU Delft
	Dr. Gautham Ram Chandra Mouli,	TU Delft
	Dr. Erik Kelder,	TU Delft

TU Delft

Preface

During this thesis I have had a lot of support from various members of the academic world. First I would like to express my gratitude to my supervisor Dr. René van Swaaij. He has introduced my to this thesis topic and has supported me every week, by providing scientific insights and by aiding me to explore different research objectives. His feedback has improved the result of this work tremendously and this research would not have come so far without his help.

Secondly, I would like to thank Dr. Zhaolong Li who helped me during the battery testing process. He has explained every step of the way from cutting the anode of the battery to testing the performance of the battery as a whole. Also I would like to express my gratitude to Prof.Dr.ir. Marnix Wagemaker supporting this project and for allowing this research to use vital resources at the RID and for providing insights during the meetings about the battery tests.

Furthermore, the experimental process during this work would have not been so smooth if it were not for the technicians of the EKL. Therefore I would like to express my gratitude to Martijn Tijssen, Daragh O'Connor and Stefaan Heirman, who have all solved experimental issues and gave technical guidance along the way.

Besides the technicians of the EKL, I want to thank the technicians that supported this research in the battery lab of the SEE group. Frans Ooms and Esther Bijl have helped resolve issues in the process of making the batteries and have given insights on how to improve the assembly process.

For the modeling part I would like to thank Dr. Malte Vogt, he has provided vital insights regarding the COMSOL model and the model would not have come together without his help.

Lastly, I would like to thank my fellow members of the battery group, Raimon van Grootel and Siri Gani. They were there to support me and to give insights in their research process. It was a pleasure to work with them and follow their research progress during this work.

Tim Ammerlaan
Delft, October 2021

Abstract

Lithium-ion batteries are currently most commonly used in most electronic devices. These batteries are used because of their superiority in gravimetric energy and cyclability compared to other battery technologies. The most common anode used in lithium-ion batteries is currently graphite. Graphite has proven to be a very stable cycling material. However, with a specific capacity of 372 mAh/g, there are alternatives with higher specific capacities.

One of those alternatives is silicon, which has a theoretic capacity of 3000 mAh/g. However, a volume change of 200-300% occurs when a pure silicon anode is cycled. Thereby cracking the material and losing the majority of this theoretic capacity. The capacity retention of a silicon-based anode can be increased by various techniques. Of those techniques two are used in this work, alloying the silicon with carbon and creating a porous material.

This research aims to evaluate the effect of carbon concentration and porosity in the hydrogenated amorphous silicon carbide (a-SiC_x:H) on cycling performance of Li-ion batteries when this material is used for the anode. The a-SiC_x:H used in this research is deposited on carbon fiber paper (CFP) using Plasma Enhanced Chemical Vapour Deposition (PECVD). By varying the precursor gas flows used during the PECVD the structure of the a-SiC_x:H is changed and samples with varying porosity and carbon concentration are obtained. These anodes are then tested using coin-cell batteries in a half-cell configuration. The results of a stability test indicated that the sample with an estimated carbon concentration of 8% and a porosity of 29% had the best capacity retention, retaining 61% of the initial 1800 mAh/g during 60 cycles at 0.3C. This result is achieved with the sample having the highest carbon concentration and porosity that was researched in this work, suggesting that both a high carbon concentration and a high porosity value increase the capacity retention of the a-SiC_x:H anode. Individual contributions of the carbon concentration and the porosity to the capacity retention have not been researched. Therefore, conclusions to these individual contributions cannot be drawn.

Contents

1 Introduction

Currently, the primary energy mix of the world is dominated by fossil fuel technologies like coal, gas, and oil. As the world moves to a more renewable future this energy mix will shift towards renewable energy sources like solar and wind energy [1]. The introduction of these renewable energy sources in the energy mix will require adaptations to the energy system as it is currently known. This has to do with the intermittent behavior of the newly introduced energy sources and the carrier in which the energy is stored, which will predominantly be electricity.

By 2050, 65% of the world energy consumed will be generated by renewable energy sources, while only 14% was produced using these sources in 2017. Of this energy that is consumed world wide 86% of the electricity will be produced in a renewable way compared to the 26% in 2018 [2]. The trend of an increasing share of solar and wind energy is shown in Figure 1 [3]. This increase will result in a need to cope with the intermittency of the produced energy by storing the excess energy and retrieving it when there is a shortage of energy. This energy will need to be stored using different energy storage technologies. This can be done using mechanical storage technologies, like compressed air energy storage and flywheels. But this energy can also be stored as chemical storage like storage in chemical bonds such as hydrogen or batteries [4].

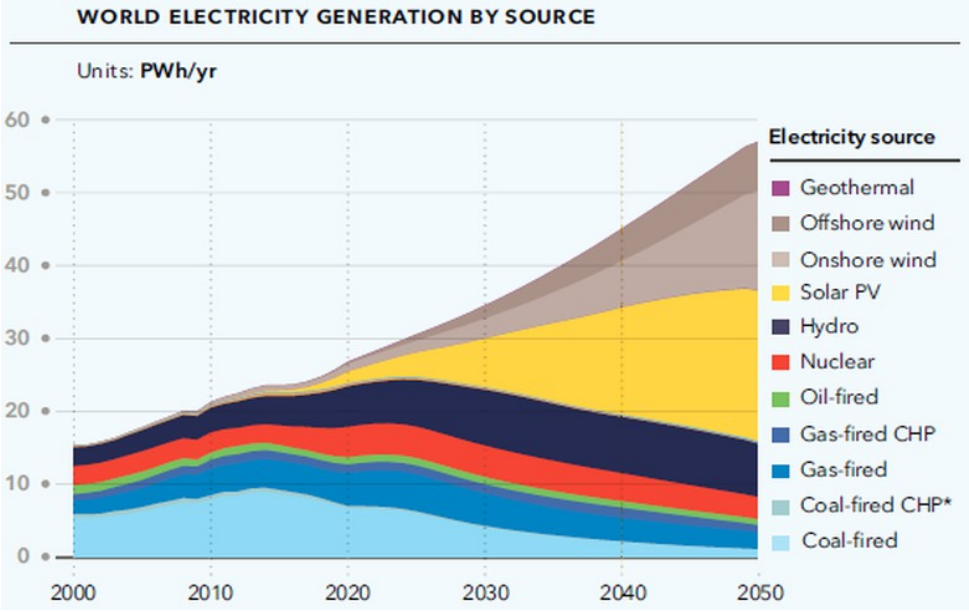

Figure 1: Global electricity generation in 2050 [3].

The sizing possibilities of mechanical storage are limited so most of the energy that is generated by renewable sources will need to be stored using (electro)chemical energy [5]. When energy is stored in chemical bonds it can be stored for longer periods and thereby be used as seasonal storage [6]. Batteries can be used effectively for shorter-term storage. The energy conversion of electricity to chemical bonds has a low efficiency compared to that of energy storage in a battery [7]. Therefore, it is important to store most short-term energy in battery systems.

Among the different types of batteries, the most common and important battery currently used is the lithium-ion battery. This battery is used in all handheld devices because of its superior volumetric and gravimetric energy density while it also has a stable cycling lifetime.

This chapter will firstly elaborate on the principles of lithium-ion battery technology. Secondly, commercial anode materials will be discussed, which is followed by a description of silicon-based anodes. After which an overview of silicon carbide alloys will be given. This chapter is concluded with the objective of this work.

1.1 Lithium-ion batteries

The topology of a lithium-ion battery, while it is connected to an external power source, is shown in Figure 2 [8]. When external power is applied to the battery it will be charged. During this charging process, Li^+ ions will flow through the electrolyte from the cathode side to the anode side where they will recombine with the electrons that flow through the external circuit to form the lithium element between the graphite layers.

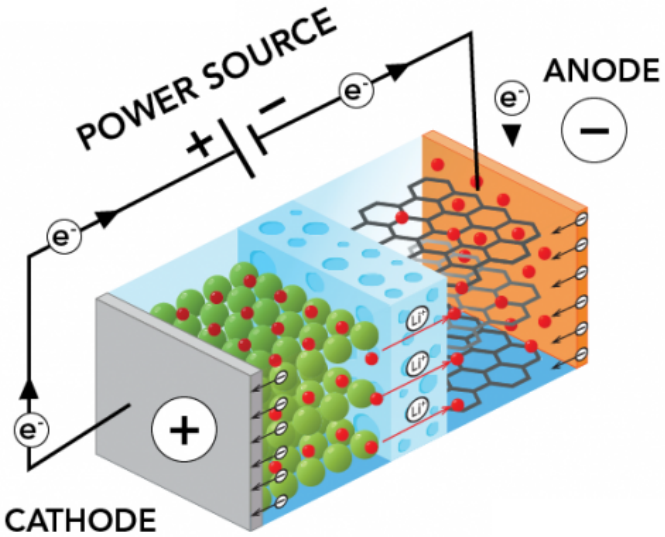

Figure 2: Schematic charging of a lithium ion battery [8].

Popular cathode materials currently are lithium cobalt oxide ($LiCoO_2$) and lithium nickel oxide ($LiNiO_2$) [9], while graphite is currently mostly used for the anode side of the battery [10].

When the external power is disconnected, the battery will start to deliver power. Li has the tendency to form lithium oxide because of its lower Gibbs free energy. This lithium oxide can be formed in the cathode of the battery. Therefore, when no external power is connected, while the anode and cathode are electrically connected by an external device, the battery will be discharged. During this discharge Li^+ ions and electrons will flow through the electrolyte and the external circuit, respectively. This flow will occur from the anode to the cathode side of the battery.

With batteries being used for an increased amount of applications, demand is increasing for lithium-ion batteries with higher volumetric and gravimetric capacities. For example, to increase the range for electric vehicles, a lot of research is done to improve the battery technology. Currently one of the limiting factors is the specific capacity of the anode material graphite, having a specific capacity of 372 mAh/g [11], while the benchmark of next-generation anodes is a specific capacity of more than 1000 mAh/g [12].

Other materials like silicon can provide those levels of specific capacity for the anode of the battery, however, this comes with a significant material stability cost. The working principles and the stability issues of these anode materials will be further elaborated on in the following sections.

1.2 Anode materials

Since the end of the 20th century many different anode materials have been studied, since then only a graphite-based carbon anode has been used commercially. The holy grail for anode materials in lithium-ion batteries is lithium metal itself, with a specific capacity of 3860 mAh/g [13]. However, this has not been commercialized due to dendrite formation and a low coulombic efficiency during the cycling process [13]. Coulombic efficiency is the defined as the of electrons retrieved from an electrode compared to the number of electrons that were introduced to the electrode. Ideally the coulombic efficiency is 100% since any lower coulombic efficiencies result in an exponential decay of the battery.

There are several ways graphite is used in the anodes of batteries, for example using different structures of graphite. Graphite anodes that are commercially used are shown in Figure 3 [14]. This figure shows that the anode structure is built up from layers of graphene between which the lithium ions can intercalate during the charging. When lithium ions are intercalated between the graphene layers they are inserted into the carbon lattice. During this insertion, the lithium-ion recombines with the electron that has traveled through the external circuit [14].

Figure 3**(a)** shows the semicrystalline, on nano-scale, graphite material is shown. This crystallite is also shown in the middle in the middle of the figure, in which the layered structure is visualized. In this part of the figure both the basal plane, parallel to the graphene layers and the edge plane, perpendicular to the graphene layers can be seen. Lithium intercalation will predominantly occur through the edge plane, thus parallel to the basal plane [14]. Figure 3**(c)** shows the stacking of the individual layers of graphene, in an AB form.

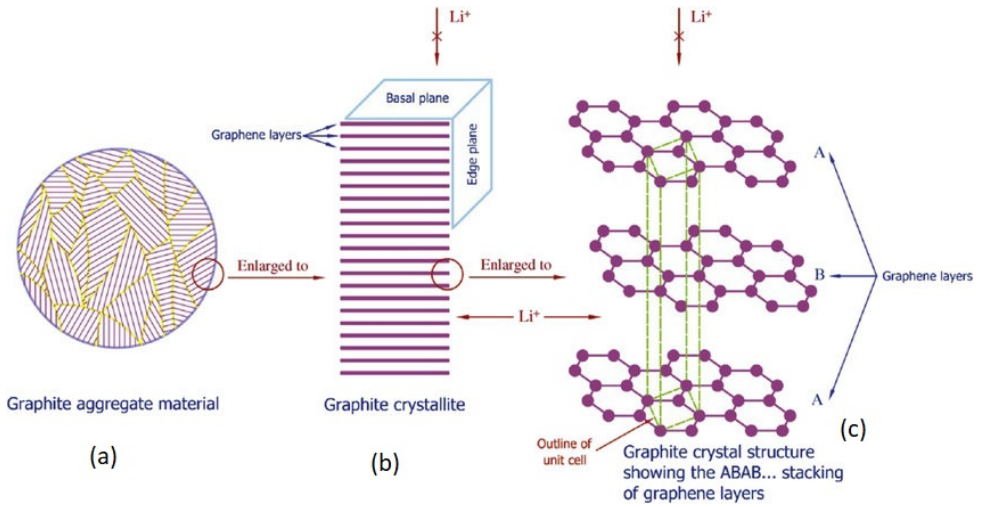

Figure 3: Schematic representation of the graphene layers in a commercial lithium ion battery of a lithium ion battery with **(a)** the aggregate graphite material, **(b)** stacked in a graphite crystallite, **(c)** individual graphene layers [14].

The working of the graphite anode is described in Equation 1.

$$Li^+ + e^- + 6C \leftrightarrow LiC_6 \tag{1}$$

To accommodate the intercalation of one lithium-ion it can be seen that 6 carbon atoms are required. Because many carbon atoms are required to store just a single lithium-ion the amount of lithium that can be stored in the electrode is limited. This explains the fact that the specific capacity of graphite is limited to 372 mAh/g of anode material.

Besides layered graphite, there are also other structures in which carbon-based materials are used in the anode of lithium-ion batteries, for example, carbon nano-tubes. Carbon nano-tubes are essentially graphene sheets that are rolled up to form a tube [15]. An advantage of such a tube is that the lithium ions can reside on both sides of the tube. This, however, does not cause specific capacities to be higher compared to that of layered graphene. The specific capacity of the nano-tubes is in the range of 200 mAh/g [15].

Besides carbon-nano tubes, mesoporous carbon is also an alternative to the stacked graphene layers. This mesoporous structure also has a high surface area with periodically occurring pores in combination with tune-able particle size. Reversible capacities of 500 mAh/g were recorded after 50 cycles using this mesoporous carbon [16].

Finally, hard carbon is also a promising alternative to layered graphene. Hard carbon, opposed to graphite does not have a periodic structure [17]. Despite this lack of periodicity specific capacities of more than 500 mAh/g are achieved with an initial coulombic efficiency of 80% [18].

1.2.1 Formation of SEI

A Solid Electrolyte Interphase (SEI) layer will form during the cycling of the battery. This is most common on the anode side of the battery. SEI formation is caused by the transport of lithium ions through the electrolyte. The number of lithium ions that are transferred during a discharge effectively determines the capacity of the battery. Therefore if the lithium ions react with the electrolyte to form inactive material on the anode the capacity will decrease [19].

The formation of SEI is typically caused by the instability of the electrolyte at the potential of the anode of the battery. However, the formation of this SEI layer is not detrimental for lithium-ion batteries. Lithium-ion batteries can still be cycled at sufficient capacity despite the SEI formation. This is because the layer of SEI is almost impenetrable by the electrolyte, thereby suppressing further growth of the SEI layer. Therefore, once an initial layer of SEI has been formed the formation of further SEI will be negligible [20]. As a result the battery will still be able to be cycled because the lithium ions, unlike the molecules of the electrolyte, can still penetrate the SEI [21].

The formation of such a SEI layer is shown in Figure 4 [22]. It can be seen that the SEI layer prevents further contact of the anode with the electrolyte. Thereby suppressing further growth of the SEI layer, all while the lithium ions can still penetrate the layer for the charge transport to occur.

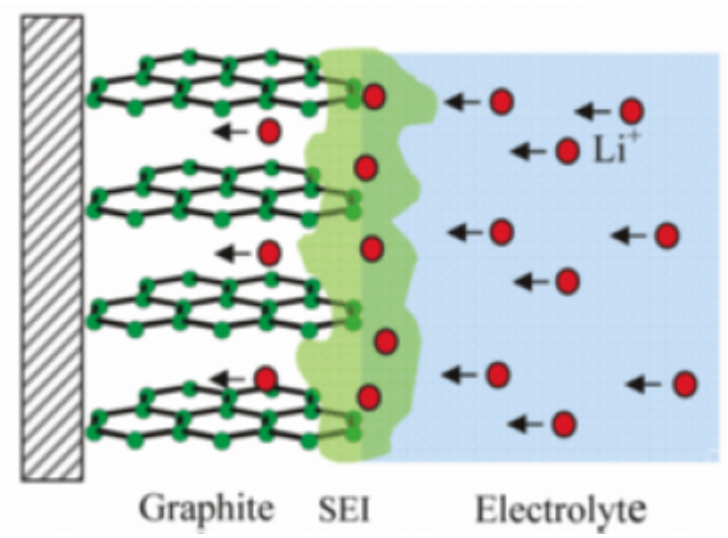

Figure 4: The SEI formation at the interface of the electrolyte and the battery anode [22].

1.2.2 Graphite oxidation

Mildly oxidizing graphite modifies the graphite electrochemical properties. The effect can be seen in two distinct processes, namely the evolution of nano-channels and the creation of a more dense layer of oxides. The presence of nano-channels will enhance the settling of the lithium atoms in the graphite lattice, while the latter results in less decomposition of the electrolyte [23]. The oxidation must be done careful manner, over-oxidating the graphite would result in the opposite effect.

1.2.3 Composites with metals and metal oxides

Besides oxidation, graphite anodes can also be composited with metals. Nickel can, for example, be used in such a composite. The graphite particles will be encapsulated with the nano-sized metal, thereby forming a composite particle. The nickel coating ensures that the active surface between the anode and the electrolyte is minimized and minimizes the co-intercalation of lithium atoms at the edges [24].

Other metals can also be used to enhance the specific capacity of a carbon-based anode. Metals like tin ($Li_{13}Sn_5$) [25], aluminum (Li_9Al_4) [26] and silicon were researched since the beginning of the century. Very specifically silicon is of interest since this metalloid can increase the specific capacity of the anode enormously. The advantages of this increased specific capacity and the issues regarding the volume expansion will be described in the next section.

1.3 Silicon-based anodes

Silicon can also be used as an anode material. With a theoretical capacity of 4200 mAh/g [27], it is a major improvement compared to the 372 mAh/g of a graphite anode. Using silicon as an anode has disadvantages, the main one is the volume change during charging and discharging. This volume change is illustrated in Figure 5 [28]. During the charging process, the volume of the silicon will increase by 300%, while this volume is lost during discharging [29]. Once again a SEI layer will be formed on the anode, just like the case with the graphite anode. But because of the volumetric change during charge and discharge this will become problematic.

In the graphite anode, the SEI formation was suppressed by the initial SEI layer, after this initial layer was formed further formation of SEI was suppressed by this layer. This is not the case when using a silicon anode, the volumetric changes during lithiation and de-lithiation will create new surface area on which the SEI layer can be formed [30]. This will create a cloud of

inactive SEI around the silicon particles. Furthermore, if the silicon is densely packed it will crack during expansion. This can be seen in the figure, the material that splits of from the bulk material results in inactive material, thereby decreasing the capacity of the battery. Therefore, the theoretical initial capacity of 4200 mAh/g can only be achieved during the first cycle of discharge of the battery when a pure silicon anode is used.

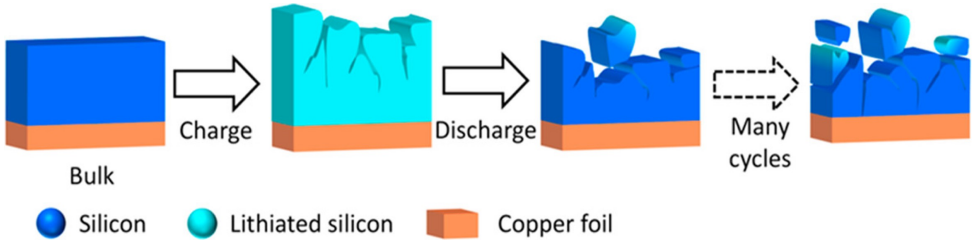

Figure 5: The volume change of silicon during charge and discharge [28].

The volume expansion is caused by the phase change, the reaction that occurs during this transition is described in Equation 2.

$$Si + 4.4Li^{+} + 4.4e^{-} \leftrightarrow SiLi_{4.4} \tag{2}$$

In this equation, it can be seen that theoretically up to 4.4 lithium can be accumulated within the silicon roster ions per silicon atom.

1.3.1 Porous structures

Porous structures can be used to cope with the volume expansion of silicon during charging. In these structures, small silicon particles can expand within the cavities of the material. This is illustrated in Figure 6 [31] in which the de-lithiated state can be seen on the left while the charged and thus lithiated state is shown on the right of the figure. Because of the void space around the silicon atoms, the anode as a whole will not change in volume only the void spaces will be filled.

Porous structures have been researched for quite some years. Porous doped nano-wires showed capacity retention of more than 2000 mAh/g with a charge and discharge current of 0.5 C, for the extent of more than 250 cycles [32]. The best battery having a capacity that was maintained above 1000 mAh/g after 2000 cycles.

A downside to the porous structure of the silicon anode is the area of the anode that is exposed to the electrolyte, on which SEI formation can occur. Research by Lu, in which the outer surface of micro-sized silicon particles was sprayed with a carbon coating. Thereby leaving the porous interior unfilled resulting in a solution for this SEI formation at the surface area. Because of this carbon coating, the SEI formation was mainly limited to the outside of the microparticles. Causing this composite structure to be able to achieve a specific capacity of 1500 mAh/g after cycling a thousand times at a rate of 0.25 C [33].

1.3.2 Nano-structures

Nano-structures can be used to cope with the volume expansion when these structures are smaller than the critical diameter they will not crack under the volume differences. This critical diameter is determined to be 150 nm [34]. This has given rise to several nano-structure variants like nano-powders, -wires, -rods, -tubes, -fibers. Besides the advantage of these nano-sized structures, there is a big disadvantage, the surface area. To have a certain mass for the anode, a large surface area is required when nano-structures are used. This area in turn results in additional SEI formation resulting in a poorer capacity performance while the anode is cycled.

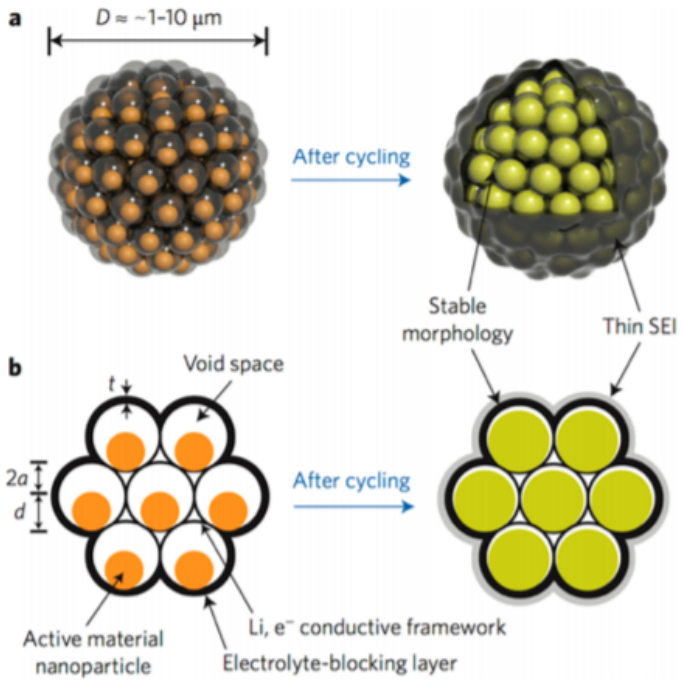

Figure 6: Porous pomegranate structure solution to expanding lithiated silicon [31].

To cope with this large area in which SEI formation will occur, a coating could be applied to the silicon nano-structure to keep the reactivity of the structure in place. This will recreate the SEI which would naturally be formed while maintaining the reactivity of the silicon atoms [35].

1.3.3 Binders

Binders are also a way to cope with the volume change of the silicon atom during charging and discharging, these binders will keep the nano-structures of the silicon bonded to each other to keep a coherent material. Figure 7 illustrates the difference between the case with and without the use of binders. The nano-structures without the binders may fall apart after cycling continuously, while the silicon with the binders keeps its structure and will thereby keep its capacity [28].

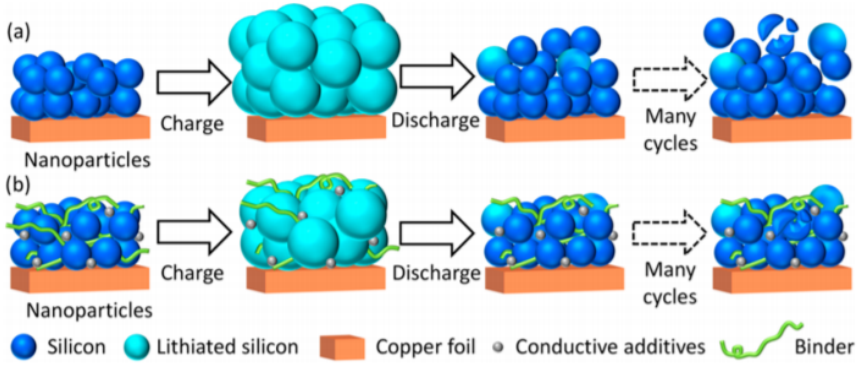

Figure 7: Schematic representation of binders which keep silicon atoms bound to each other [28].

1.3.4 Composites

Lastly, composites are used to cope with the volume change of the silicon. Composites of silicon are often made with different metals like nickel, cobalt and tin. These metals can provide an enhanced electrical conductivity with a stable capacity during cycling. An example, a composite of silicon nano-wires that were tin-doped could maintain a capacity of more than 1000 mAh/g for more than 100 cycles with a current density of 2800 mA/g [36].

Apart from metals, composites of silicon with graphite are also researched [37]. This is due to the high conductivity and the small volumetric change during charge and discharge of graphite. As remarked above, theoretically one silicon atom can facilitate 4.4 lithium ions. However in practice this is only 3.75 lithium ions per silicon atom, because the is a thermodynamically favorable formation [27], while six carbon atoms are required to store one lithium-ion. Therefore the theoretical capacity of graphite is much lower compared to that of pure silicon with a capacity of 372 mAh/g and 3600 mAh/g respectively [27]. By combining both silicon and graphite a composite can be created with a relatively high capacity with better stability during cycling compared to pure silicon.

The volume expansion of different anode materials is characterized in Figure 8, in this figure the volume expansion is compared with the volume-specific capacity of the material. It can be seen that from a specific capacity point of view pure lithium is most efficient. However pure lithium is a unstable and will thus oxidize quickly. Second to lithium is lithiated silicon, however, as is shown in the figure the volume expansion is much higher when compared to lithiated carbon. Using a combination of both silicon and carbon can thus give an anode with both a high specific capacity and limited volumetric changes. This will be further elaborated on in the next section.

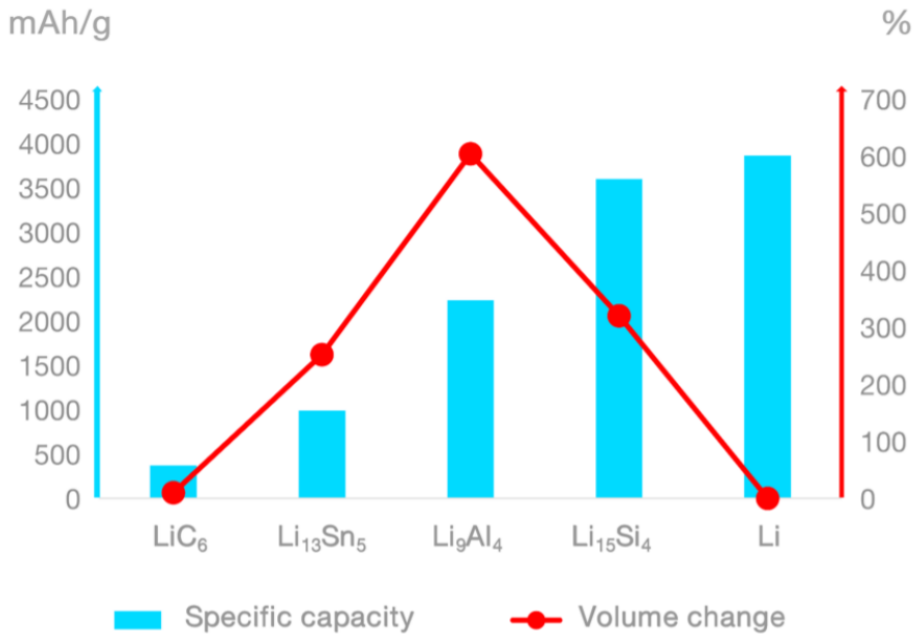

Figure 8: Specific capacities and volumetric expansions of different lithium alloys [38].

1.4 Amorphous silicon carbide alloys

Amorphous silicon carbide (a-SiC$_x$:H) can be used as an anode in a lithium-ion battery to benefit from the high specific capacity of silicon of 4200 mAh/g, while furthermore having superior structural stability from the carbon compared to pure silicon. A schematic representation of such a a-SiC$_x$:H alloy is shown in Figure 9 [39], which the silicon and carbon atoms form an amorphous structure causing the intercalation vacancies to be randomly organized. In this figure the silicon atoms are depicted in grey/green, the carbon atoms in black while the hydrogen atoms are white.

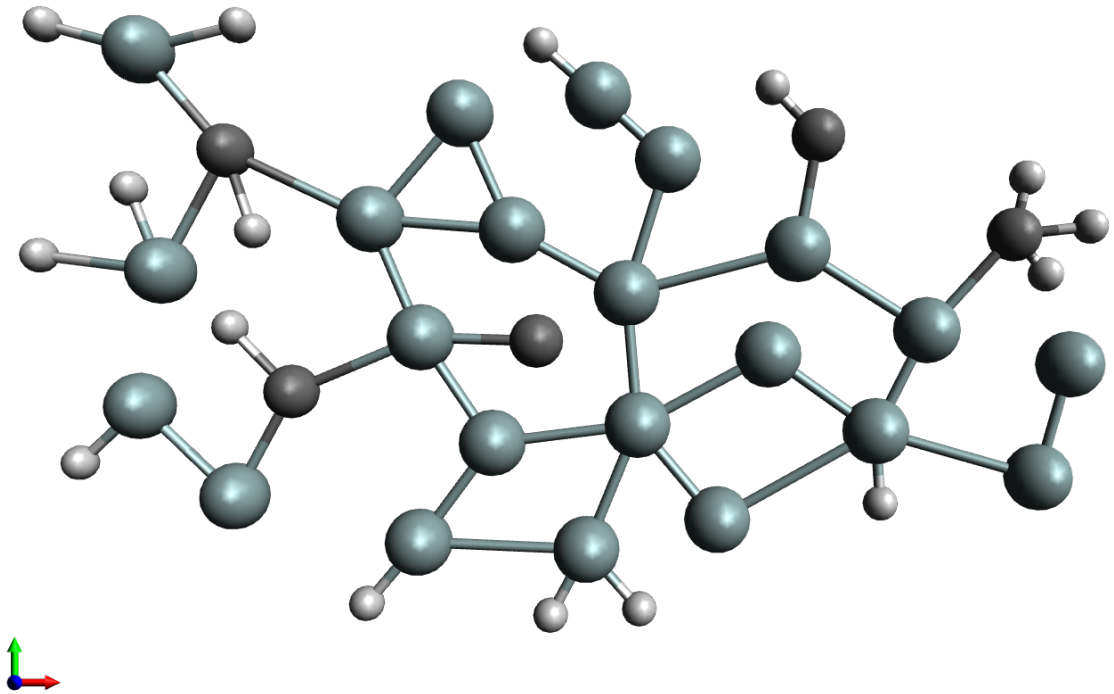

Figure 9: Schematic representation of silicon carbide.

According to Zhang et al.[40] the reactions in the amorphous silicon carbide material can be described using equations 3 and 4.

$$\mathrm{SiC} + 4\mathrm{Li}^+ + 4\mathrm{e}^- \leftrightarrow \mathrm{Li}_4\mathrm{C} + \mathrm{Si} \tag{3}$$

$$\mathrm{Si} + 3.75\mathrm{Li}^+ + 3.75\mathrm{e}^- \leftrightarrow \mathrm{Li}_{3.75}\mathrm{Si} \tag{4}$$

In these equations it can be seen that there there are two reversible reactions that occur during the charging and discharging process of the battery. Firstly, there is a conversion reaction between silicon carbide which forms silicon, after which this silicon is alloyed with lithium ions during the charging process. The study by Zhang et al. resulted in a specific capacity of only 309 mAh/g [40].

According to Huang et al., this low specific capacity can be attributed to the reversibility of the Equation 3, therefore they suggest that equation to be like is displayed in Equation 5, with y being smaller than 1 [41]. This equation emphasizes the irreversibility of the initial reaction in which the silicon is produced. This reaction would occur more spontaneously because of the lower Gibbs free energy. After Equation 5, Equation 4 would occur during the cycling process.

$$\mathrm{SiC} + x\mathrm{Li} + + x\mathrm{e}^- \rightarrow \mathrm{Li}_x\mathrm{Si}_y\mathrm{C} + (1-y)\mathrm{Si} \tag{5}$$

The creation of a-SiC$_x$:H was always hard to avoid because of the strong tendency of silicon and carbon atoms to bond. In recent years the potential of the a-SiC$_x$:H as part of the materials used in lithium-ion batteries has been reported. Huang et al. have shown an initial specific capacity of 917 mAh/g of which 376 mAh/g was left after 100 cycles were completed [41].

Another example is the work done by Zhang et al., in which silicon/carbon nano-tubes were made as an anode material. The synthesizing of the nano-tubes is a difficult process and the interaction is weak between the silicon and the carbon nano-tubes. This was resolved by using silica as a reactant via a magnesium reduction. This resulted in a capacity of 1100 mAh/g and retention of the capacity of nearly 84% after cycling 200 times [40].

These research results have proven that the use of a-SiC$_x$:H as an anode material can be a viable option. Thereby increasing the specific capacity of the anode compared to when purely graphite is used. However, the fade in capacity should be minimized to have a stable anode.

2 Objective of this work

This work will focus on depositing a-SiC$_x$:H layers on carbon fiber paper (CFP). The aim of this research is to evaluate the effect of a varying carbon concentration on the cycling stability of the material. The a-SiC$_x$:H will be deposited directly on the CFP and tested in coin-cell batteries. The CFP can be used as the anode of the coin-cell battery, making this a relatively simple process.

To determine the specific capacity of the deposited a-SiC$_x$:H the capacity contributions of both the CFP and the deposited a-SiC$_x$:H have to be taken into account. An assumption is made that the specific capacity of both materials is used during the cycling of the battery, which is verified by the use of a varying mass load of a-SiC$_x$:H.

The anode material will be placed in a coin-cell battery to evaluate the initial capacity and capacity retention of the material. Alloys with a varying carbon concentrations will be tested and the differences between these alloys will be highlighted.

This will be done based on previous work by Wang [38] who deposited a-SiC$_x$:H on CFP and achieved a capacity retention of 58.8% with a mass load of 1.2 mg/cm^2 after 10 cycles. This sample consisted of a carbon concentration of 7.2% and a porosity of 33%.

3 Experimental procedures

In this chapter the deposition and characterization of hydrogenated amorphous silicon carbide (a-SiC$_x$:H) is described and how this material is incorporated in a coin-cell for battery testing. These a-SiC$_x$:H layers have been made using different gaseous mixtures and deposition powers. By varying the deposition conditions the composition and porosity of the layers deposited onto the substrate is altered, each contributing differently to the overall performance of the battery. During this research, the a-SiC$_x$:H anodes were deposited using the AMOR machine located in the Else Kooi Lab of the Delft University of Technology. The deposition process and the substrate preparation are described in Section 3.1. The substrates that are used in this work are discussed in Section 3.2, while the coin-cell battery assembly process is described in Section 3.3.

3.1 Sample deposition

In order to fabricate the anodes the a-SiC$_x$:H needs to be deposited on the desired substrate. For this project, Plasma Enhanced Chemical Vapour Deposition (PECVD) was used. In this process precursor gases react on a preheated substrate and form a thin layer on this substrate. The energy required for dissociating the precursor gasses into growth particles is provided by radiofrequency electromagnetic waves. Therefore the deposition can occur at a lower substrate temperature. The composition of the deposited layer and the deposition rate is highly dependent on the deposition power and the mixture of the gases used. Therefore the deposition settings are carefully reviewed before depositing a sample.

Since the results of this research are based on the findings of previous work done by Wang [38] the conditions of that research have to be reproduced. Reproducing these findings will not simply be achieved by using the same deposition settings as were used before. This will not result in an exact match of the deposition environment that was achieved during the previous research because the PECVD machine used in both research work, the AMOR, has been dismantled and reassembled in between the deposition periods. Besides that, the settings of the AMOR also drift during periods of use thereby causing a shift in absolute deposition settings.

In order to do the reproduction of the depositing environment used in the previous research three depositions are made on Corning glass. During these depositions, the gas mixture is the same as used during the previous research. Also, the substrate temperature and the deposition pressure are kept constant. The deposition power, however, is varied, first a deposition is performed using the same deposition power as the previous work. After which two deposition are performed, one with an increment of 0.5 W of deposition power and one with a reduction of 0.5 W of deposition power.

3.1.1 Plasma Enhanced Vapour Deposition

A schematic representation of the PECVD is shown in Figure 10 [42], the plasma provides the energy required for breaking up the gaseous mixture to form the desired a-SiC$_x$:H. In the schematic representation, the showerhead PECVD configuration is shown, the metal holder is positioned on the grounded electrode with the substrate facing down. This ensures that dust particles that are generated in the plasma will not fall onto the substrate. The holder with the substrate is heated to the processing temperature of the deposition chamber by the heater located on top of the chamber, while the grounded electrode provides an electrical ground for the holder. The powered electrode is located below the substrate and uses the RF-generated energy to create the plasma required for cracking the precursor gasses. The vacuum pump that keeps the chamber in a vacuum is located on the right while the precursor gases enter the chamber from the bottom.

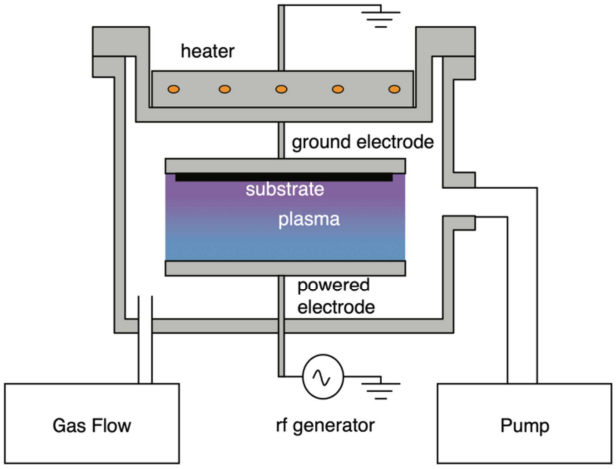

Figure 10: The schematic setup of the PECVD machine used to deposit the anodes in this research [42].

AMOR specifications

As mentioned in the introduction of this chapter, all of the depositions are done using the AMOR deposition tool located in the cleanroom 10000 in the Else Kooi Laboratory. This machine consists of five vacuum chambers. Four of these are used for depositing either n-/ p-doped or intrinsic material, while the last chamber is used to flip the holders and substrates. Because this research requires very different deposition conditions and deposition duration solely chamber four of the AMOR is used, in order to ensure that the photovoltaic research is not affected by the deposition for the anodes. The technical specifications of chamber four can be seen in Table 1.

Table 1: Technical specifications deposition machine AMOR.

AMOR specifications	**Values**
Chamber used	4
Electrode distance	21 mm
Type of electrode	Showerhead
Area of electrode	144 cm^2

When the substrate is heated up to the correct temperature the gas lines are purged to prevent previously used gas flows to be introduced in the chamber when the plasma is on. After the gas flow is cleaned out the gas flows that are used for the deposition are introduced. Furthermore the pressure and thereby the position of the gas flow valve are tuned before lighting the plasma.

The gases used during the deposition are silane (SiH_4), methane (CH_4) and phosphine (PH_3). Silane is used to retrieve the silicon precursor, while methane is used to retrieve the carbon that is desired in the a-SiC_x:H. Lastly, phosphine is used to dope the material, increasing both conductivity and porosity [43].

In order to make a comparison between the different depositions, some deposition settings are fixed, for example, deposition pressure and substrate temperature. But also the total partial pressure of the silane and methane and phosphine is kept constant. In Table 2 all of the constant conditions are described. These fixed deposition settings are equivalent to the settings used in the prior research and thereby make a comparison between the results of both pieces of research possible. In the table ϕ_{CH_4} and ϕ_{PH_3} are the flow rate, in standard cubic centimeter per minute (sccm), of the methane and silane respectively, while ϕ_{SiH_4} is the flow rate of the dopant phosphine.

Table 2: Deposition specifications used during research.

Deposition parameters	Values
$\phi_{CH_4} + \phi_{SiH_4}$	40 sccm
ϕ_{PH_3}	11 sccm
Pressure in chamber	0.7 mbar
Temperature of substrate	180 °C

In order to make samples with a varying carbon concentration, the partial pressures of the precursor gas flows are varied. Since the combined partial pressure of silane and methane is kept constant a methane flow fraction can be defined, as shown in the equation below. In here R is the fraction methane relative to the combined methane and silane flow rate.

$$R = \frac{\phi_{\mathrm{CH_4}}}{\phi_{\mathrm{CH_4}} + \phi_{\mathrm{SiH_4}}} \tag{6}$$

The variation of the methane flow fraction causes a change in carbon concentration. If this methane flow rate is increased the carbon concentration in the deposited anode will also be increased. The carbon concentration is not solely dependent on the relative methane flow fraction and other factors such as the deposition power used also play a key role. Since the deposition power is also varied in order to achieve similar deposition conditions as the previous research both the deposition power and the relative methane flow rate will determine the actual carbon concentration. In this work, the carbon concentrations of Wang [38] are assumed when similar deposition rates and thus similar deposition conditions are achieved.

The relative methane flow fraction used in this research are 0.5, 0.6, 0.7, 0.8, with estimated carbon concentrations of 0.2% , 2% , 5% and 8 % respectively.

3.2 Substrates

During this research different substrates have been used. First to determine the correct deposition settings in order to reproduce the results of the previous research the a-SiC$_x$:H is deposited on Corning glass.

The depositions on Corning glass are not used as anodes in the coin cells during the battery testing. The anodes which are used in the battery tests are deposited on CFP. This is due to its small thickness and shape ability to be cut into the desired size. Besides these practical dimensional aspects of the substrate, it is also a material that can be lithiated. Therefore this electrochemical capacity has to be taken into account during the battery experiments.

Corning glass

Corning glass is used to determine the deposition conditions which is similar to the previous research by determining the rate of material deposition. Three depositions are done with a varying deposition power, each of these depositions is analyzed using Scanning Ellipsometry (SE), which is further elaborated on in Section 4.1.

Using a model within the library of the SE, of amorphous silicon deposited on glass, the thickness of the deposition can be determined. Since the deposition is timed the deposition rate can be determined when the deposition thickness is known. By interpolating these rates between the different deposition powers the desired deposition power can be determined. The properties and the preparation of the Corning glass are described in Table 3.

Table 3: Corning glass substrate properties and preparation.

Dimensions	10 cm x 10 cm with 0.7 mm thickness, split into 3 pieces of roughly 3.3 cm x 10 cm
Application	Performing measurements using Spectroscopic Ellipsometry
Substrate preparation	First the Corning glass is subsided for 10 minutes in an ultrasonic bath of acetone. Secondly the Corning glass is subsided for 10 minutes in an ultrasonic bath of isopropyl alcohol.

Carbon fiber paper

The a-SiC$_x$:H that is used in the coin cells that are tested during this research is deposited on carbon fiber paper (CFP). This is done due to its noncontaminative nature, unlike copper or nickel foil of which processing with silicon can pose serious issues in the EKL cleanroom, and the easy-to-process nature of the material.

The CFP is not pre-treated, unlike the Corning glass and the deposited layer will simply attach to the carbon fibers in the substrate. The a-SiC$_x$:H will be deposited in the porous structure of the substrate. The thickness of the deposited of the a-SiC$_x$:H is low compared to the thickness of the substrate. This thickness of deposited a-SiC$_x$:H is in the order of several microns while the substrate has a thickness of 127 microns [44].Because of this surface area within the substrate nearly all a-SiC$_x$:H is deposited in the porous structure of the carbon fibers. Thereby the porous structure of the fibers will not be filled. Therefore no layer of a-SiC$_x$:H will be formed on top of the substrate.

The structure of the CFP is very porous, which will be visualized by the Scanning Electron Microscopy images. Because of this porous structure it was assumed that a part of the deposition would be deposited on the holder underneath the CFP. To evaluate if this was indeed the case a piece of aluminum foil was placed beneath the substrate, cut to the exact size of the CFP.

Table 4: CFP properties and preparation.

Dimensions	Cut to the desired size, generally, 5 cm x 4 cm
Application	Performing battery tests by using the substrate as anode in coin cells
Substrate preparation	No special preparation is done before deposition

The substrates used in this research were prepared before deposition, and mounted onto a 10 cm by 10 cm metal holder. To ensure that the layer thicknesses was homogeneous over the substrate, the substrate was mounted at the center of the holder, as the deposition is fairly homogeneous in the center of the holder and falls off near the edges of the holder. The glass substrates were sized so they could be mounted using the backplate of the holder, as is shown in Figure 11a, while the CFP needed to be taped to the holder using heat-resistant tape as is shown in Figure 11b.

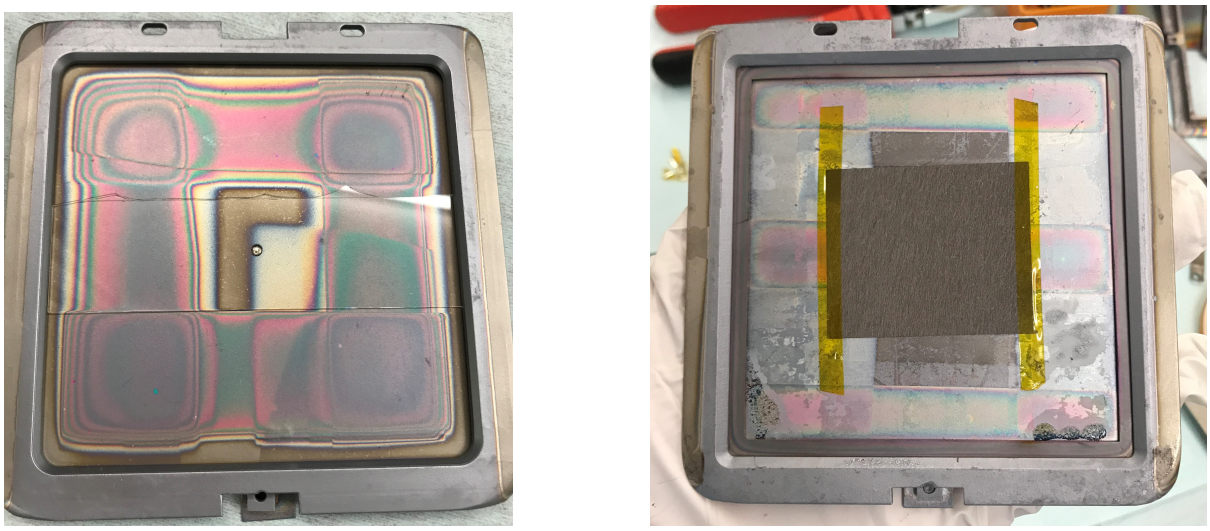

(a) **(b)**

Figure 11: Metal holder with mounted substrates before deposition, **(a)** Corning glass substrate and **(b)** the CFP.

Aluminum foil

To determine the transmission through the CFP during deposition aluminum foil is placed behind the CFP. The aluminum foil is cut to the same size as the CFP in order to ensure that all of the deposited a-SiC$_x$:H will have passed through the CFP. Like the CFP, the aluminum foil is not exposed to any cleaning solutions. Dust or other particles are removed from the material by a pressurized nitrogen gun. The properties and preparation of the aluminum foil are described in Table 5.

Table 5: CFP properties and preparation.

Dimensions	Cut to the desired size, generally 5 cm x 4 cm to match CFP size
Application	Determining transmission of CFP
Substrate preparation	Excess dust and other particles are removed by pressurized nitrogen

The transmission of the a-SiC$_x$:H through the CFP is illustrated in Figure 12. In Figure 12a the backside of deposited CFP is shown, it is clear that there is a color difference and that this has to do with the deposition. This difference can also be observed in Figure 12b in which the metal holder is shown after deposition.

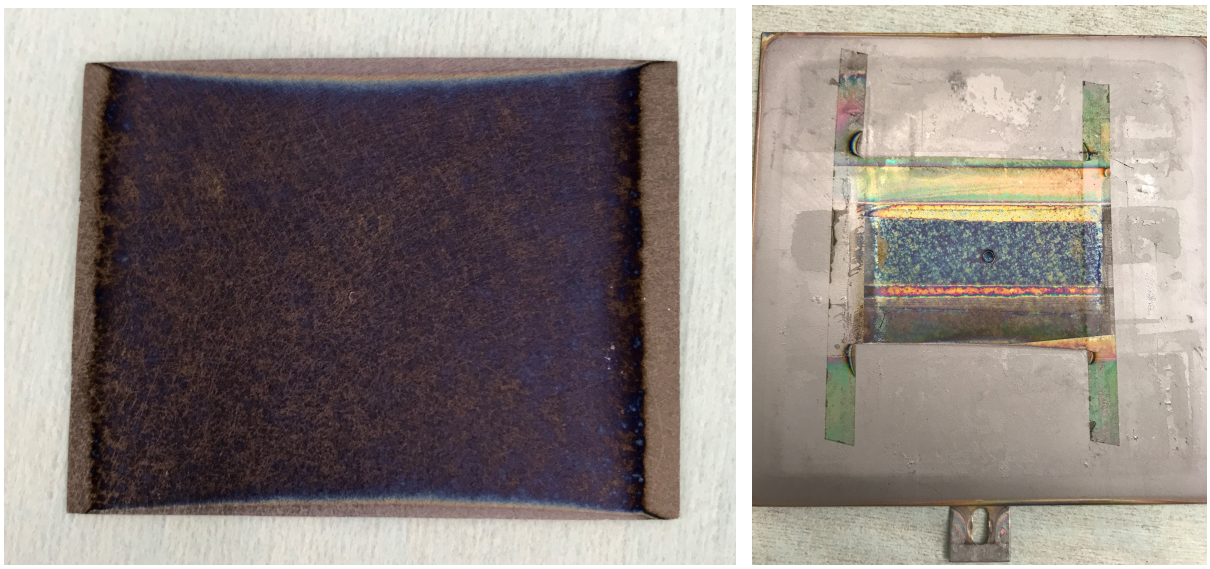

(a) **(b)**

Figure 12: (a) Transmission of a-SiC$_x$:H through CFP seen from back of substrate,**(b)** a-SiC$_x$:H deposited onto the metal holder.

a-SiC$_x$:H deposition

By using conditions with a similar deposition rate and optical bandgap as previous research by Wang it was assumed a similar material composition would be achieved given that the same gas mixture and pressure were used while deposition. Only the deposition power itself was varied in order to match the deposition rate of the previous research. All deposition were carried out at low powers ranging from 2.6 to 3.3 W, while the previous research results were computed using the deposition power of 3 W. Therefore similar conditions and thus material properties can be assumed.

This research aims to vary the carbon concentration using different gas mixtures. As described earlier the total flow of methane and silane combined is 40 sccm while the flow of phosphine is kept constant at 11 sccm. The specific flows of the methane and silane are varied in order to produce samples with a varying carbon concentration. This is shown in Table 6, in which the different partial pressures and the resulting carbon concentration are shown. The carbon concentrations that are shown in this table have been determined during prior research by Wang [38].

Table 6: Partial pressures silane and methane and the corresponding carbon concentration.

Partial pressure SH4	Partial pressure CH4	Carbon concentration
20 sccm	20 sccm	0.2%
16 sccm	24 sccm	2%
12 sccm	28 sccm	5%
8 sccm	32 sccm	8%

With these varying flows not only the carbon concentration is changed but also the porosity of the sample. Unfortunately, due to time constraints, the effect of a solely changing porosity could not be tested with a constant carbon concentration. Therefore the effect of a variation in carbon concentration could not be tested fully orthogonal.

3.3 Coin-cell assembly

In order to evaluate the performance of the deposited anodes they are tested in a coin-cell. Coin-cells are widely used for powering a multitude of appliances and are also commonly used in half-cell experiments in which either the performance of a battery anode or cathode is tested. In this research, the electrode which is to be tested, the a-SiC$_x$:H anode, is used as the cathode of the battery, while a lithium metal plate is used as the anode material in the battery.

Previously in this report, the a-SiC$_x$:H deposition has been described as the deposition of the anode of the battery, while in fact the a-SiC$_x$:H is used as the cathode material in the half-cell test. The role of an electrode in a lithium-ion battery is either that of a cathode or an anode, which electrode performs which role is dependent on their reduction potential. The anode consists of the electrode with the lower reduction Li/Li$^+$ potential, while the cathode has thus the higher reduction potential.

In commercial batteries metal oxides such as Lithium Nickel Cobalt Aluminum Oxide (NCA) [45] or Lithium Cobalt Oxide ($LiCoO_2$) are used as electrodes. These have a reduction potential around 4 V Li/Li$^+$ while this is only 0.4 V for the a-SiC$_x$:H electrode [46]. Therefore the a-SiC$_x$:H electrode would function as the anode in a conventional commercial battery.

This is not the case in the half-cell test used in this work, the lithium plate electrode has a 0 V reduction Li/Li$^+$ potential and therefore the reduction potential of the a-SiC$_x$:H is higher and thus the a-SiC$_x$:H will be the cathode in the half cell test. Therefore the terminology of the deposited electrode is changed from anode to cathode in this research. This will however not change any of the previously discussed mechanisms with regards to capacity fade and electrode reactions.

The coin cells that are used for the half cell battery tests are constructed at the Reactor Institute in Delft using one of the onsite located gloveboxes. This construction process will be elaborated on in the following part.

First the deposited anode is cut into the desired circular shape, this is done using an anode clipper as is shown in Figure 13. This circle has a radius of 6.35 mm and thus an area of 126.7 mm^2. This area will later be used to determine the areal capacity of the anode. The process of this clipping is shown in Figure 14. First, several anodes are clipped from the deposited substrate, after which each anode is weighed separately.

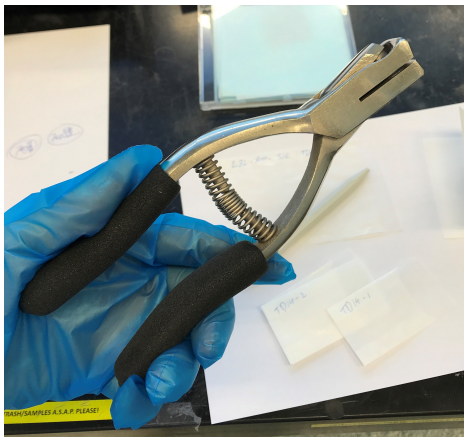

Figure 13: The 12.7 mm diameter electrode clipper used to cut the anode.

The anode is weighed on a scale to determine the weight of the combined substrate and deposition. When the mass of the bare CFP is known the weight of the deposited a-SiC$_x$:H can be determined with an accuracy of $\pm$ 0.014 mg, as is shown in Equation 7.

$$
\begin{aligned}
m_{SiC} &= m_{total} - m_{CFP} \\
\Delta m_{SiC} &= \sqrt{(\Delta m_{total})^2 + (\Delta m_{CFP})^2} \\
\Delta m_{total} &= \Delta m_{CFP} = 0.01 mg \\
\Delta m_{SiC} &= \sqrt{(0.01)^2 + (0.01)^2} = 0.014 mg
\end{aligned} \tag{7}
$$

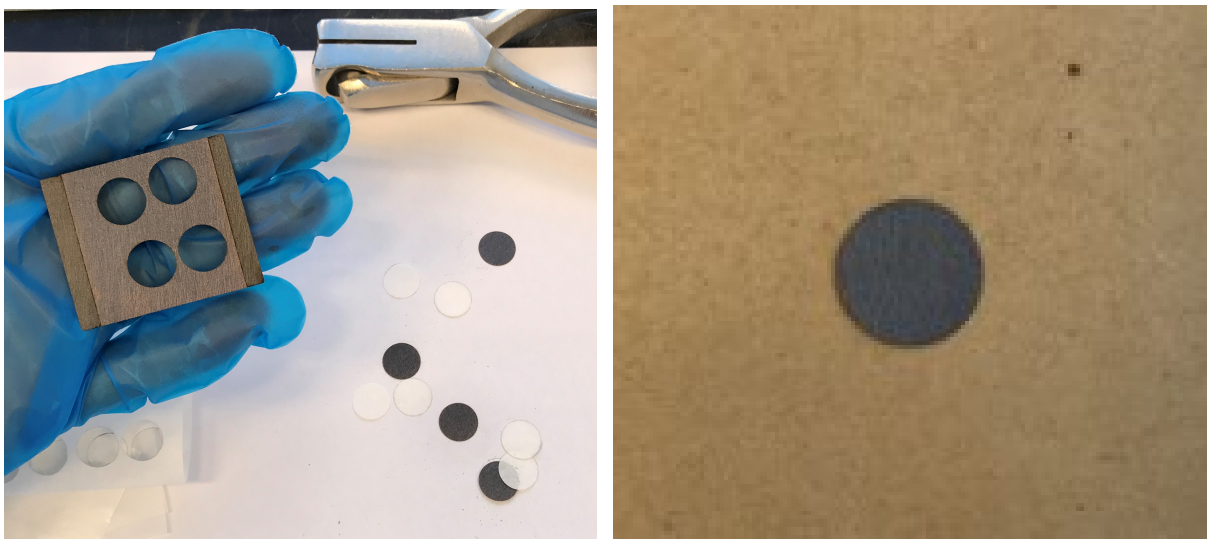

(a) **(b)**

Figure 14: The process of clipping the anodes to be used in the battery tests, **(a)** Anodes are clipped from the deposited substrate and **(b)** a single anode which is used in the coin cell during half cell experiments.

After the weighing the anodes are dried in a vacuum oven, this in order to ensure that all of the humidity in the sample is evaporated since this can be harmful to other battery samples which are constructed in the glovebox.

Once the samples are dried they are entered into the glovebox and the coin-cell battery is assembled. The different components of this coin cell are shown in Figure 15 [47].

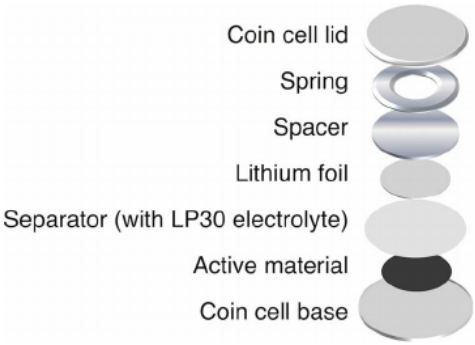

Figure 15: The different components of the coin cell assembled during the half cell test [47].

First the deposited cathode is placed on the coin cell base after which a minor part of the electrolyte is added on top of the cathode. This ensures both adhesion and conduction to the separator and also to fill the porous structure of the cathode with electrolyte.

After the separator is placed the remaining electrolyte is added on top of it after which the lithium metal plate is placed. The battery processing is finished with a metal spacer plate and a spring after which the coin cell lid is placed on top. The coin cell is then crimped using the coin cell crimper shown in Figure 16.

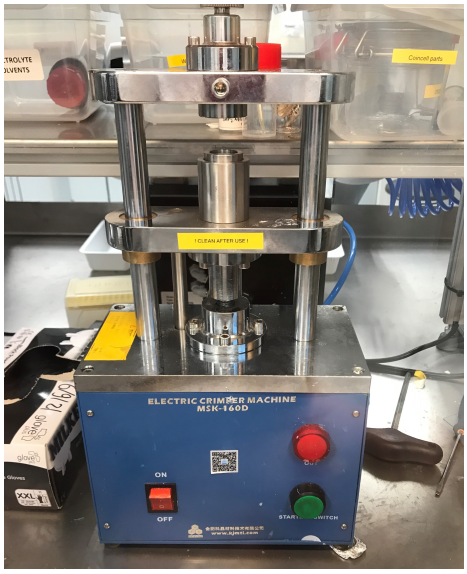

Figure 16: The coin cell crimper MSK 160D used to crimp the coin cell.

4 Measurement setup

In order to evaluate the material properties and cycling capability of the batteries, several measurements are performed. Material characteristics such as refractive index and porosity are deduced from Spectroscopic Ellipsometry which is elaborated on in Sections 4.1, 4.2 and 4.3. The transmission of the carbon fiber paper (CFP) is discussed in Section 4.4. A closer look at the structure of the substrate is taken using a scanning electron microscope in Section 4.5. Lastly, the testing of the deposited anodes using half cell tests is discussed in Section 4.6.

4.1 Spectroscopic Ellipsometry

To measure the deposition thickness at certain deposition power and gas distribution spectroscopic ellipsometry is used. Since this deposition has been running during a timed period the rate of deposition of the a-SiC$_x$:H can be determined. Reproduction of the previous research is assumed when the same deposition rate is observed while using the same gas mixture and pressure settings. Furthermore the optical bandgap is used to get a rough measurement of the composition of the material. When both the deposition rate and the optical bandgap measurement match that of the previous research similar deposition conditions are assumed.

The measurement in this work is performed using the J.A. Woollam M2000DI, which can be seen in Figure 17. The J.A. Woollam covers a 193 up to 1690 nm wavelength range and has a rate of data acquisition of 0.05 seconds. Furthermore, it can estimate thicknesses of samples from a few nanometers up to 18 mm [48]. During the spectroscopic ellipsometry measurement, a beam of light is reflected by the deposited substrate onto the receiver. This characterization technique has several benefits.

(a) **(b)**

Figure 17: The spectroscopic ellipsometry machine used in this research to determine deposition rate, **(a)** the light source and polarizer head and the detector head with sample stage, **(b)** the J.A. Woollam power source.

First of all the measurement is done within one minute, therefore many measurements of different depositions can be made in a short time which allows evaluation many samples. Thereby allowing to tune the deposition power accordingly in order to recreate the deposition conditions of the previous research.

Secondly, the measurement is non-evasive thus it does not change the integrity of the evaluated sample, making it possible for further characterization to be done using the same sample.

Finally, a multitude of characterization aspects can be determined using a single measurement, such as deposition rate, by evaluating the thickness after a specified deposition time.

But also the optical properties such as refractive index and the bandgap of the material can be determined. Furthermore, the porosity of the deposition that is evaluated can be determined, in this work this is done using the Bruggeman Effective Medium Approach [49]. This approach will be discussed in Section 4.3.

4.1.1 Working principle of spectroscopic ellipsometry

Light is an electromagnetic wave that consists of two different components, an electrical component and a magnetic component. These two waves traverse space with a phase difference of 90 degrees and are schematically represented in Figure 18 [50].

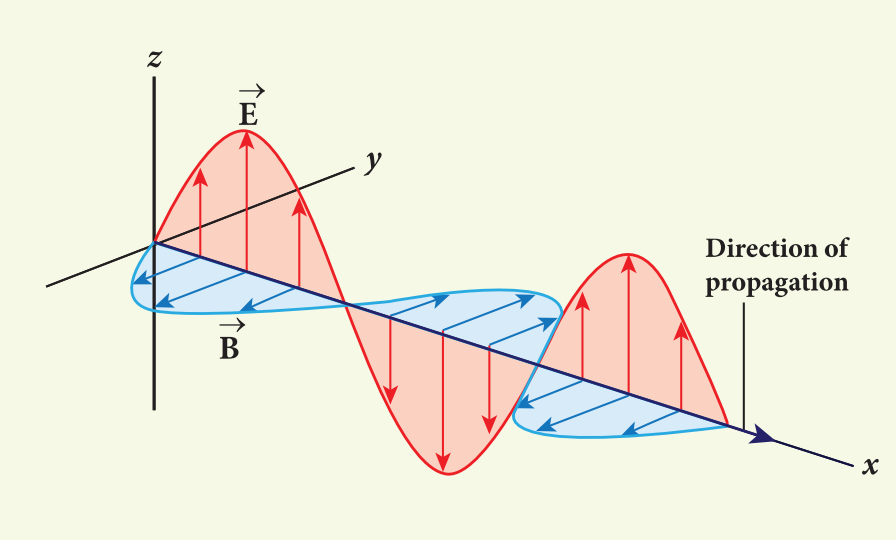

Figure 18: Schematic representation of light consisting of electromagnetic waves [50].

Linearly polarized light is emitted from the polarizer head. Once the light interacts with the surface of an object it can either be reflected or absorbed, in this research the reflected electromagnetic wave is of interest since this wave is received by the receiver of the J.A. Woollam. When the linearly polarized light interacts with the surface of the substrate the polarization is changed. This change in polarization is measured by the detector head.

The complex reflection coefficients $\widetilde{r_p}$ and $\widetilde{r_s}$ are used in to determine the change in polarization. These reflection coefficients are defined as follows [51]:

$$\widetilde{r_p} = \left(\frac{\widetilde{E_r}}{\widetilde{E_l}}\right)_p = \frac{n_t \cos\theta_i - n_i \cos\theta_t}{n_i \cos\theta_t - n_t \cos\theta_i} \tag{8}$$

$$\widetilde{r_s} = \left(\frac{\widetilde{E_r}}{\widetilde{E_l}}\right)_s = \frac{n_i \cos\theta_i - n_t \cos\theta_t}{n_i \cos\theta_i - n_t \cos\theta_t} \tag{9}$$

In these equations, $\widetilde{r_p}$ and $\widetilde{r_s}$ are Fresnel coefficients which are solutions to the boundary problems at the material interface. Furthermore, $\widetilde{E_i}$ and $\widetilde{E_r}$ represent the incident and reflected electric field respectively, while θ_i and θ_t and n_i and n_t are the angles of incidence and transmission of the light.

The variables that are estimated to model the substrate are γ and Δ. When taking the ratio of these complex reflection coefficients they are retrieved [52].

$$\frac{\widetilde{r_p}}{\widetilde{r_s}} = \frac{\frac{|E_{out}|}{|E_{in}|}}{\frac{|E_{out}|}{|E_{in}|}} e^{i(\delta_p - \delta_s)} = \tan(\psi) e^{i\Delta} = \rho \tag{10}$$

From the ellipsometry measurement the complex refractive index, N, of the material can be deduced. This complex refractive index can be described using the following equation.

$$N = n + ik \tag{11}$$

In here n is speed of light inside the film as a function of wavelength, while k is the extinction coefficient. This extinction coefficient is dependent on the absorption coefficient of the material and wavelength. It is a measure of the amount of light that is absorbed in the material. The values of n and k are always related to each other and are always positive.

From the complex refractive index the complex dielectric function can be determined. This complex dielectric function is the square of the complex refractive index and can be described using

$$\tilde{\epsilon} = \epsilon_1 + i\epsilon_2 \tag{12}$$

In this equation ϵ_1 can be negative for some metals in some parts of the wavelength range, while ϵ_2 is always positive in order to be a physically feasible model. This physical feasibility should be taken into account when analyzing spectroscopic ellipsometry data.

4.2 Determination of deposition rate

To determine the layer thickness Δ and ψ is retrieved from the SE setup in the Complete EASE software. From the SE measurement, the ψ and Δ data are retrieved for 5 different angles of light. In Figure 19 the data of the two parameters are shown for a sample with 0.2% carbon concentration. The Δ parameter is shown in green, while the ψ parameter is shown in red. The model that is used to match the data is represented by the dotted.

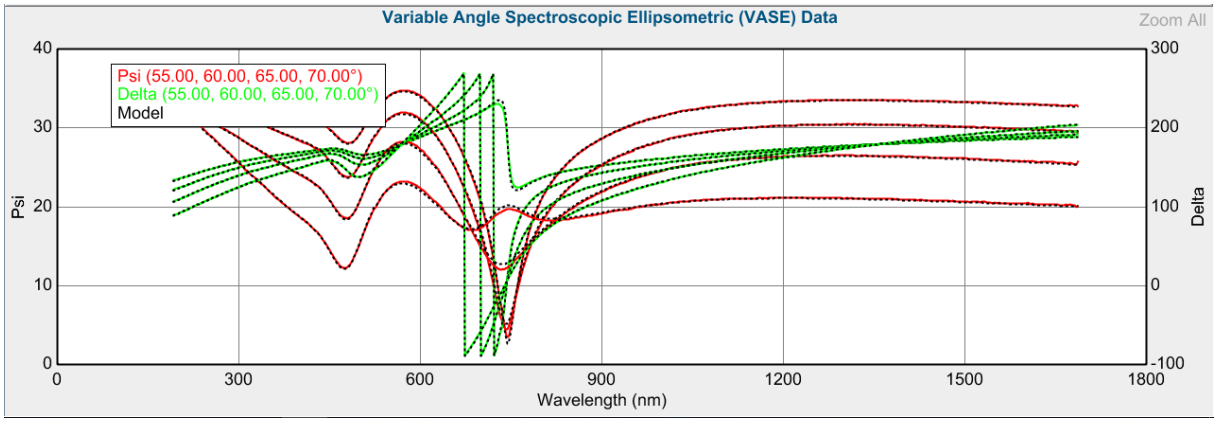

Figure 19: The measured Delta and Psi data of the 0.2% carbon sample.

The model used in this research, amorphous silicon on glass without backside reflection, is a model that is standard in the Complete EASE library. The parameters of this model are shown on the right of Figure 20. The Mean Square Error (MSE) is shown on the left, this value needs to be below 20 for the model to be a good representation of reality.

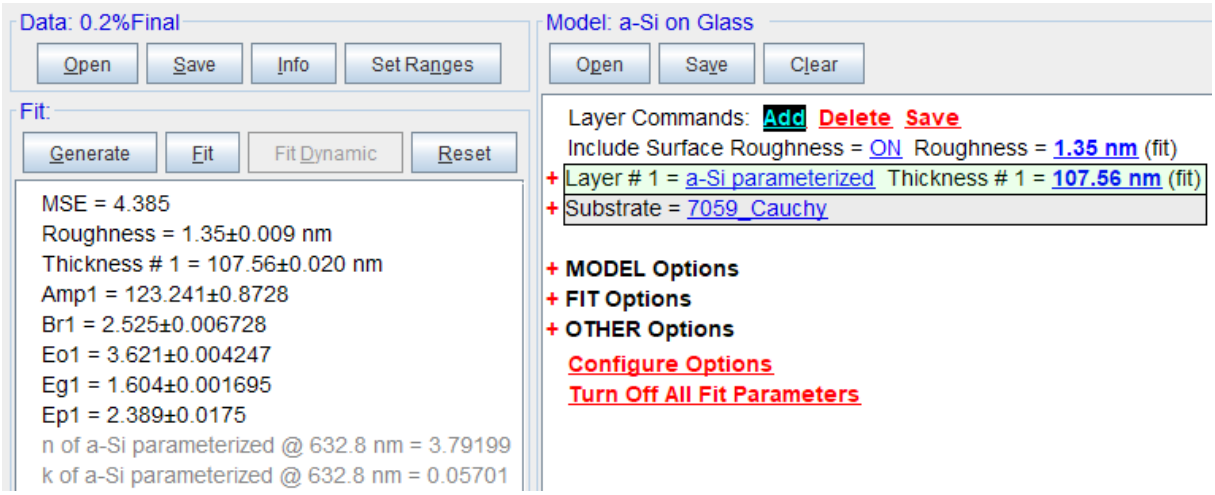

Figure 20: The model in used to match the data and the MSE that corresponds with the data.

For the data presented in Figure 20 the MSE is, 4.385 which means that the model used is a good representation of reality for this set of parameters. Therefore an estimation of the thickness of the a-SiC$_x$:H layer can be made and this is shown on the right of the figure. In this case, the thickness of the layer is 107.56 nm with an estimated roughness of 1.35 nm.

The model used in the library is based on pure amorphous silicon on glass, this results in a good fit for the samples with low carbon concentration but will differ more when substrates with higher carbon concentrations are tested. However, since the estimated carbon concentrations do not exceed 8% the model still gives a good fit to the measurement data to determine the thickness of the layer and the optical properties of the sample. These optical properties are then used to determine the porosity of the sample using the Bruggeman Effective Medium Approach, which is elaborated on in the next section.

4.3 Porosity determination using Bruggeman Effective Medium Approach

A schematic representation of a heterogeneous material is displayed in Figure 21. The Bruggeman Effective Medium Approach (EMA) is based on the theory that the properties of two heterogeneously mixed phases can be determined by evaluating the properties of each component [53].

In this thesis the two phases are described as voids and bulk material. Since the Bruggeman EMA treats both phases equally the voids and bulk material can either be of material A or B in Figure 21. The fraction of voids compared to the fraction of the bulk material will determine the type of material structure that is observed. When one phase is dominant the separated-grain structure will be observed, while the aggregated structure will be observed when these fractions are in the same order of magnitude.

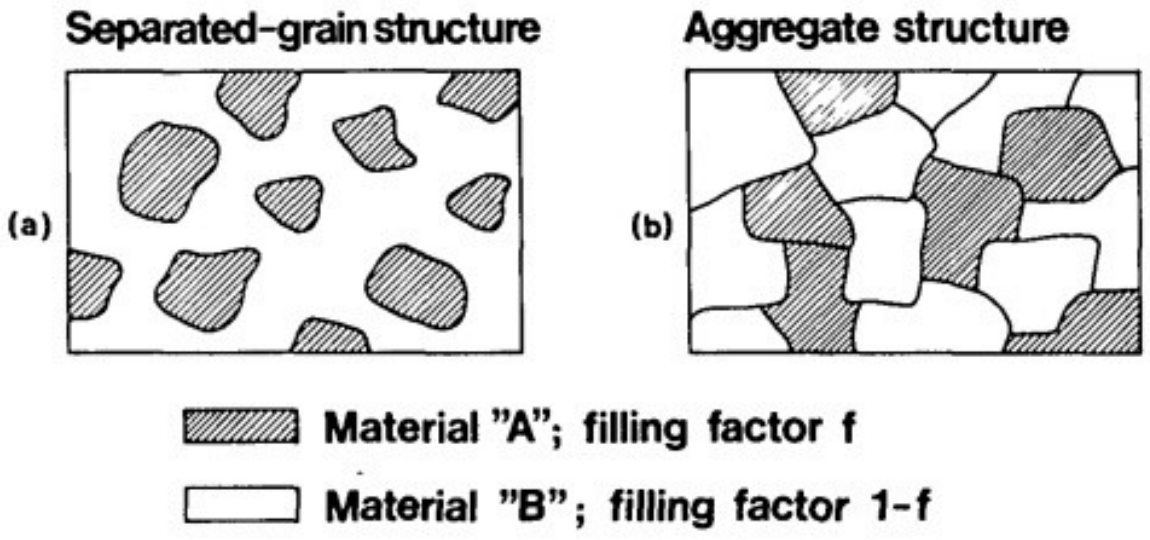

Figure 21: Heterogeneous material that can be described used the Bruggeman EMA **(a)** with separated-grain structure or **(b)** aggregate structure [49].

The Bruggeman EMA uses the data that is retrieved in the far-infrared region of the measurement [53]. In this work the far-infrared region is defined as the region which starts when the value of k is zero. To determine the porosity the measured data is first structured in order to be used in Equation 13 [54].

$$(1-p)\left(\frac{n_i^2-n_a^2}{n_i^2+2n_a^2}\right)+p\left(\frac{1-n_a^2}{1+2n_a^2}\right)=0 \tag{13}$$

In this equation, the n_i represents the intrinsic refractive index of silicon, which is the square root of the relative permittivity (3.4 [55]). Since the samples that were evaluated were not solely made from silicon also the permittivity of the alloying element carbon has to be taken into account. This was done by assuming a linear relationship between the permittivities of both materials, which in turn showed a good resemblance while evaluating stoichiometric a-SiC_x:H as is displayed in Figure 22.

In this figure, the linear trend between the permittivity of silicon, with a corresponding carbon fraction of 0, and the permittivity of carbon, which in turn corresponds with a carbon fraction of 1 is displayed. The permittivity of stoichiometric SiC is 6.2 [56]. This linear estimation is plausible because the linear trend is in line with the permittivity of stoichiometric SiC. Furthermore, since only low carbon concentrations are used the error made using this estimation is limited.

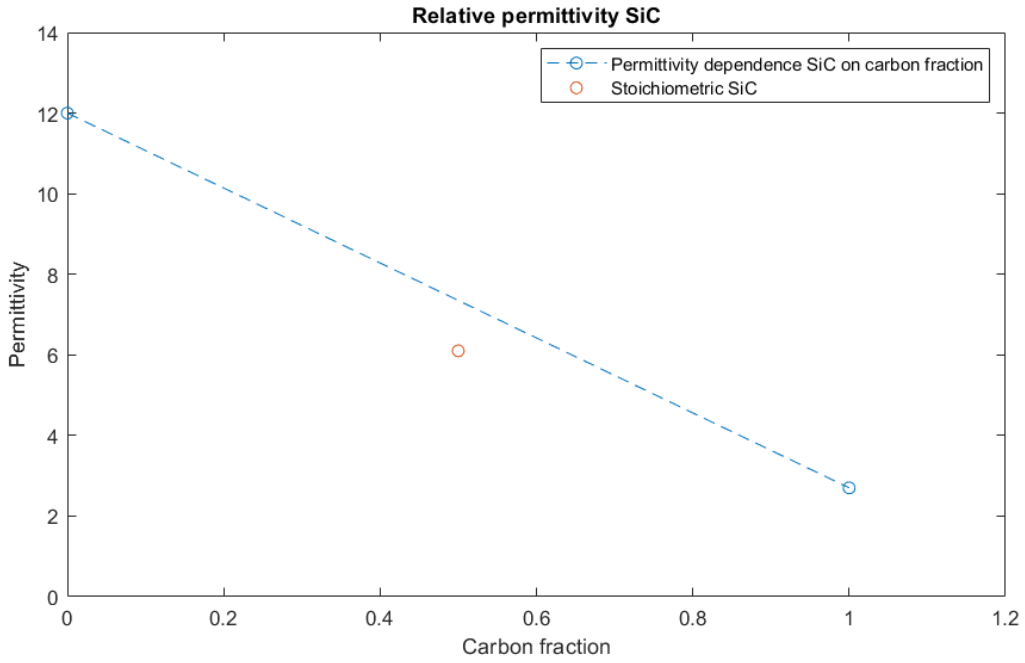

Figure 22: The linear permittivity estimate compared with the stoichiometric permittivity of SiC.

The n_a of Equation 13 represents the measured refractive index of the deposited substrate in the far-infrared region of the wavelength range..

As described using Figure 22 the n_i is dependent on the sample composition, using the linear approach of the permittivity, which is in the square of the refractive index, and incorporating the estimated carbon concentration will lead to the value for this parameter. The permittivity of silicon and graphite is assumed to be 12 [57] and 2.7 [58] respectively.

Lastly, p represents the void volume fraction which will be referred to as the porosity of the sample. The n_a is determined using the optical parameters retrieved by the spectroscopic ellipsometry, an example of such retrieved data is shown in Figure 23.

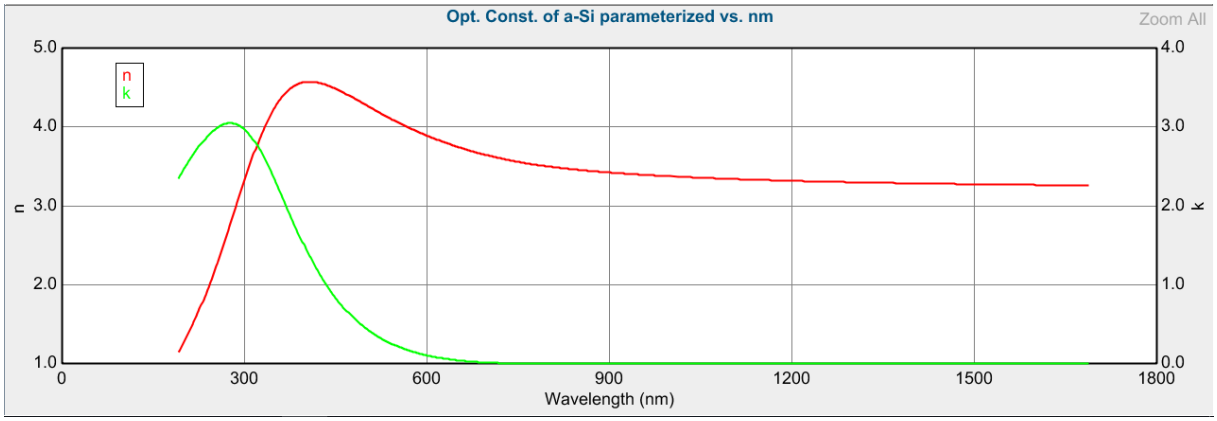

Figure 23: The optical parameters retrieved from the Complete EASE software.

4.4 Transmission of CFP

The CFP has a porous structure, therefore part of the deposition will be deposited on the metal holder beneath the substrate. To determine the transmission of the substrate a mass measurement pre and post-deposition is done. The transmission of the CFP is determined by the mass that is deposited on the Al foil which is placed underneath the CFP during the deposition. The ratio of the mass deposited on the Al foil compared to the total deposited mass (on both the CFP and the Al foil) is determined to be the transmission. Therefore the mass of both the Al foil and the CFP have to be measured. The scale used in this research is displayed in Figure 24

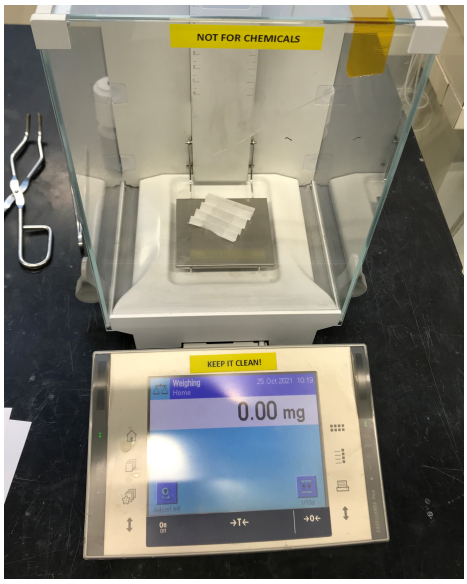

Figure 24: The scale used to measure the substrates before and after depositions.

In Figure 25 both the aluminum foil and the carbon fiber substrate are shown after deposition. The color difference that is caused by the deposited a-SiC$_x$:H is visible on both the CFP and the Al foil.

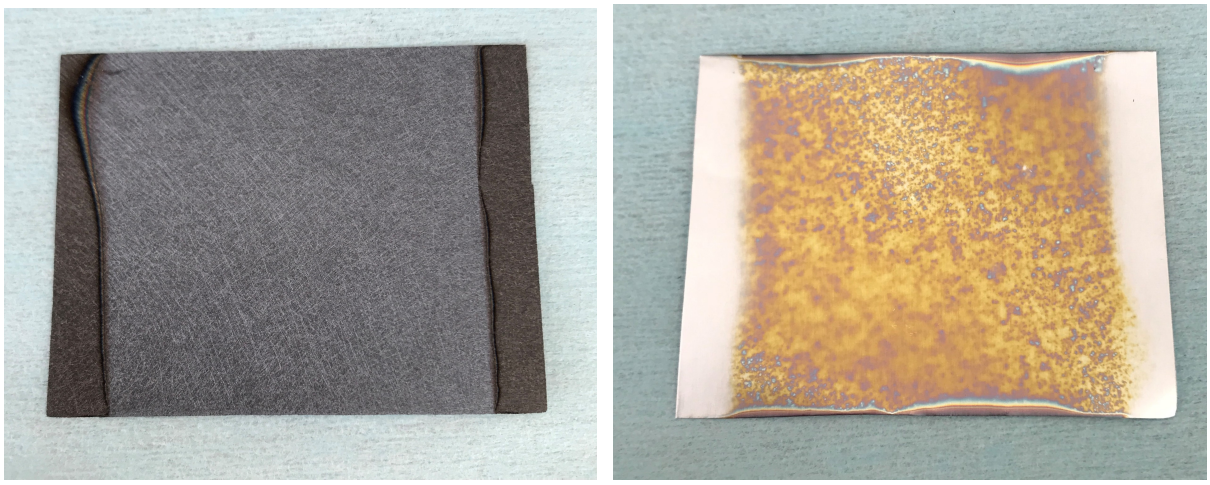

(a) **(b)**

Figure 25: (a) Deposited a-SiC$_x$:H on both the CFP, **(b)** the transmitted a-SiC$_x$:H through the substrate on the Al foil.

4.5 Scanning Electron Microscopy

To evaluate the structure of the CFP with and without deposited a-SiC$_x$:H the substrate is evaluated under a scanning electron microscope. Also, the structural change of charging and discharging of the a-SiC$_x$:H electrode is evaluated using this technology, thereby comparing structural changes in the material. The microscope used in this work is the Hitachi Regulus 8230 which is shown in Figure 26 [59].

Figure 26: The overview of the scanning electron microscope used in the research [59].

4.6 Battery testing

When the batteries are assembled they are tested to evaluate the performance of the anode as a whole. As mentioned before this is done by doing a half-cell test, as opposed to the test of a regular battery with both a cathode and anode this test is only focused on the anode. During this test, the a-SiC$_x$:H carbide anode acts as the cathode of the battery, this is because it is coupled with a pure lithium metal electrode. This lithium electrode has a lower oxidation potential, being -3.04 V [60] compared to the a-SiC$_x$:H , being 0.4V [46].

The capacity of the lithium metal anode is greater than the capacity of the a-SiC$_x$:H cathode. This causes the a-SiC$_x$:H cathode to be the limiting factor during cycling. Therefore only the performance of the a-SiC$_x$:H is tested during the cycling of the coin-cell batteries.

In order to determine the capacity of the a-SiC$_x$:H the battery is charged and discharged in a battery bank, which is shown in Figure 27. In Figure 27a the room where 100 different batteries can be cycled is shown. For this research 6 so-called channels were available for the cycling of the coin cells. The coin cells are cycling using holders specifically made for this purpose, one of which is shown in Figure 27b.

The battery is charged and discharged based on the the theoretic capacity of the cathode. To determine this rate of charging and discharging the specific capacities of the CFP and a-SiC$_x$:H are taken into account. The specific capacity of the carbon fiber substrate is 350 mAh/g [61], while the deposited a-SiC$_x$:H has a specific capacity of 3000 mAh/g. The respective mass contributions of the CFP and the deposited a-SiC$_x$:H are taken into account in combination with the respective capacities to determine the cycling rate of the battery.

(a) **(b)**

Figure 27: The coincell cycling setup used during this research with **(a)** the battery cycling room and **(b)** a individual coin cell test setup.

4.6.1 Battery rate test

To determine the rate capability of the battery a rate test is used. During this test, the battery is charged and discharged at different rates. Initially, the battery is conditioned by cycling it at 0.05C, after which it is cycled at 0.1, 0.2, 0.3, 0.5, 1 and 0.1 C. During these cycles it can be observed that the amount of energy that can be stored in the battery diminishes with increasing rate of charge. The last cycles of 0.1 C can be compared with the initial cycles of 0.1 C in order to evaluate the effect that the cycling has on the capacity of the battery. During this test the battery is cycled with a constant current. When a voltage of 1.5V is reached the battery has been completely charged, while a voltage of 0.01V indicates that the battery is completely discharged.

4.6.2 Battery stability test

Besides determining the capability of charging and discharging the battery, the stability of the material while experiencing a greater number of cycles is researched. This is done using five initial cycles of 0.05C, after which the battery is charged and discharged using a C-rate of 0.3. At this rate the battery is subjected to 100 cycles in order to evaluate the aging effect and thus the stability of the anode material while it is repeatedly exposed to a substantial charge and discharge rate. In order to compare the data of the stability test with the data of the rate test, the batteries are also cycled using a constant current in the same voltage window.

5 Material characterization

To be able to compare different depositions individual depositions are characterized and differences between depositions are highlighted. With a varying precursor gas flow composition and deposition power both the porosity and the carbon concentration of the deposited sample will change. One of the factors that influences these differences is the deposition rate. This deposition rate and the properties on which this deposition rate depend are discussed in Section 5.1. One of the effects of the variation of the precursor gasses and deposition power is a change in porosity of the sample. This variation in porosity and the trend of increasing porosity with an increase in carbon concentration is discussed in Section 5.2.1.

Besides the characterization of the deposition, the substrate itself can also be characterized. This is done by evaluating the substrate using a Scanning Electron Microscope (SEM) in Section 5.2.2. The transmission of the carbon fiber paper (CFP) substrate is characterized by determining what fraction of the deposited hydrogenated amorphous silicon carbide (a-SiC_x:H) passes through the substrate onto the metal holder behind it. The results of this characterization are elaborated on in Section 5.2.3.

5.1 Deposition rate

The rate of deposition during the PECVD depends on the mix of precursor gasses and the deposition power and deposition pressure used, and to a smaller extent on the substrate temperature. This section will focus on the effect of the gas mixture and deposition power. The precursor gas mixture influences the deposition rate because of the energy that is required to break the atomic forces between the molecules of the precursor gasses.

The variation in deposition rate is also shown in Figure 28. In this figure, the deposited mass-load per square centimeter on the CFP is displayed. Since samples in the order of 1 mg/cm^2 are required these deposition times are in a different order of magnitude compared to the depositions discussed on Corning glass.

In the figure, it can be seen that the mass load of a-SiC_x:H increases linearly with deposition time. Besides the relative methane flow rate fraction, the deposition power plays an important role in the deposition rate. This can be observed by comparing the curve of the 2.6W 0.2% carbon concentration with the 6W 0.2% carbon concentration curve, both depositions use a precursor flow rate of 20 sccm CH_4 and SiH_4. The difference in deposition rate is, however, clear: the mass-load of the 2.6W sample increases by 1.85×10^{-3} $mg/cm^2/min$, while this is 7.25×10^{-3} $mg/cm^2/min$ for the 6W sample.

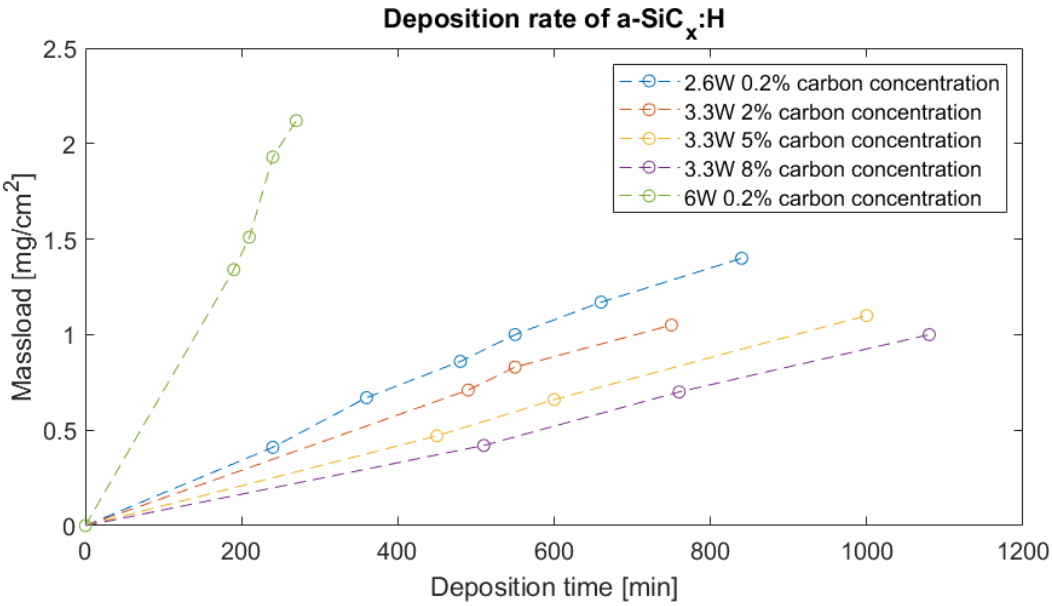

Figure 28: Mass load of deposited a-SiC$_x$:H on the carbon fiber substrate.

Besides the importance of the deposition power the effect of a varying methane precursor flow can be observed, this is displayed in Figure 29. When evaluating the 2% carbon concentration sample with the 8% carbon concentration sample it can be deduced that the 2% carbon concentration sample has a higher deposition rate. This sample reaches has a deposition rate of 1.4×10^{-3} mg/cm^2/min, while the 8% sample has a deposition rate of 0.9×10^{-3} mg/cm^2/min. This complies with the depositions on Corning glass during which the depositions of high carbon concentration resulted in lower deposition rates compared to the samples with lower carbon concentrations.

The deposition rate of four different carbon concentrations is shown during a deposition of 15 minutes on Corning glass. The depositions with a methane flow fraction of 0.6, 0.7 and 0.8 sccm are made with the same deposition power, 3.3W. The methane flow fraction, R, is defined as

$$R = \frac{\phi_{CH_4}}{\phi_{CH_4} + \phi_{SiH_4}}, \tag{14}$$

in here ϕ_{CH_4} is the flow of methane and ϕ_{SiH_4} is the silane flow. Each increase in flow rate decreases the deposition thickness that is measured and thereby the deposition rate of the sample.

The deposition with the methane flow fraction of 0.5 is deposited with a lower deposition power, 2.6W therefore this sample can not be used to make conclusions about the influence of the methane flow rate for the deposition rate.

The energy required to break the bonds of the methane precursor gas is higher, the average bond strength of C-H is 415.5 kJ/mol [62], while the average bond strength of the silane precursor gas Si-H bond is only 384.15 kJ/mol [63]. Therefore an increase in the methane flow rate decreases the deposition rate.

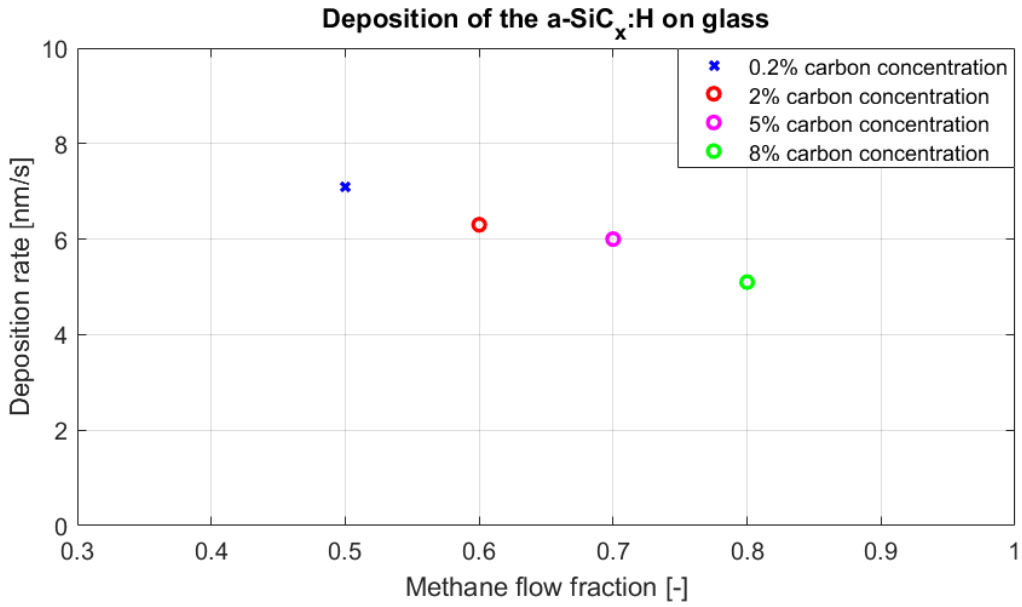

Figure 29: Deposition rate of a-SiC$_x$:H on the Corning glass.

5.2 Deposition results

5.2.1 Porosity

To determine the porosity of an anode a deposition on Corning glass is done, after which it is evaluated using SE as described in Section 4.1. Using the wavelength-dependent n and k values of this measurement in the far-infrared region, when the value of k is zero, an estimate can be made of the porosity using the Bruggeman Effective Medium Approach [53].

The porosity of the different carbon concentrations varies with the composition of the material. A trend can be observed, samples with a higher carbon concentration also have a higher porosity value. This is shown in Figure 30.

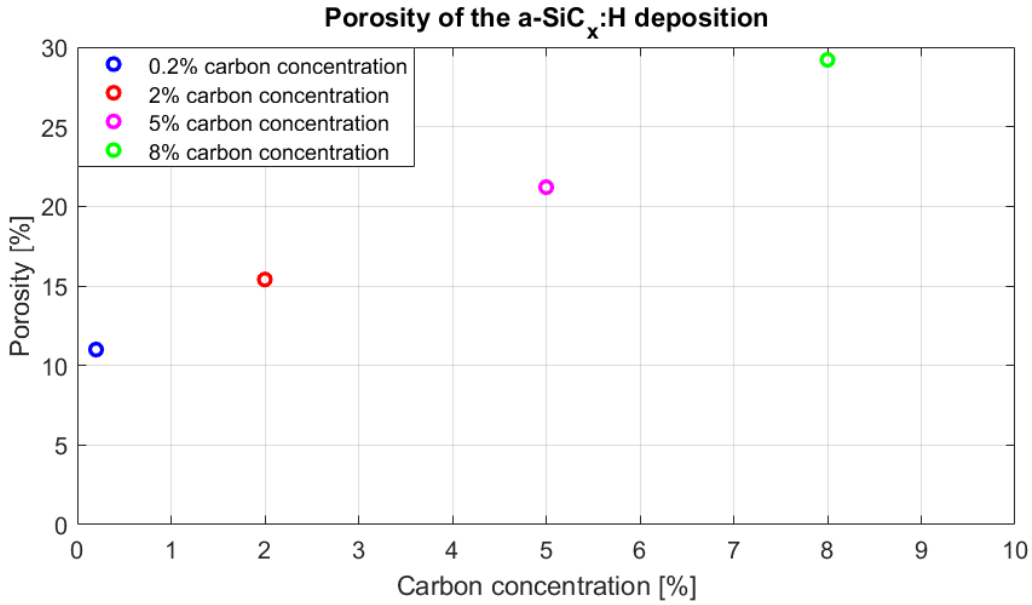

Figure 30: The porosity of the deposited a-SiC$_x$:H as a function of the carbon concentration of the sample.

The increase in porosity with the increase of carbon concentration is important to take into account when evaluating the performance of the batteries. Since the carbon concentration and the porosity both trend up when a higher methane flow fraction is used the change in performance of the battery cannot only be attributed to the increase in carbon concentration. The increase in porosity increases the internal surface area of the a-SiC$_x$:H.

5.2.2 Structure of CFP

The CFP has a very porous structure. A picture of the CFP made using the SEM is shown in Figure 31a, using a magnification of 1000. The fibers have a diameter of approximately 10 µm and create a rough mesh on which the a-SiC$_x$:H is deposited on. This deposited a-SiC$_x$:H on the fibers can be seen in Figure 31b.

Since this picture, which is representative for a larger surface area, is taken from the top side of the substrate it may be concluded that very little material onto the fibers.

Furthermore, it can be concluded that the deposited a-SiC$_x$:H is not homogeneously attached to the carbon fibers, it clusters at certain parts of the mesh. This suggests that the a-SiC$_x$:H does not attach to the carbon fibers directly, since it would be divided more homogeneously on the fibers if this were the case, but grows from previously deposited a-SiC$_x$:H.

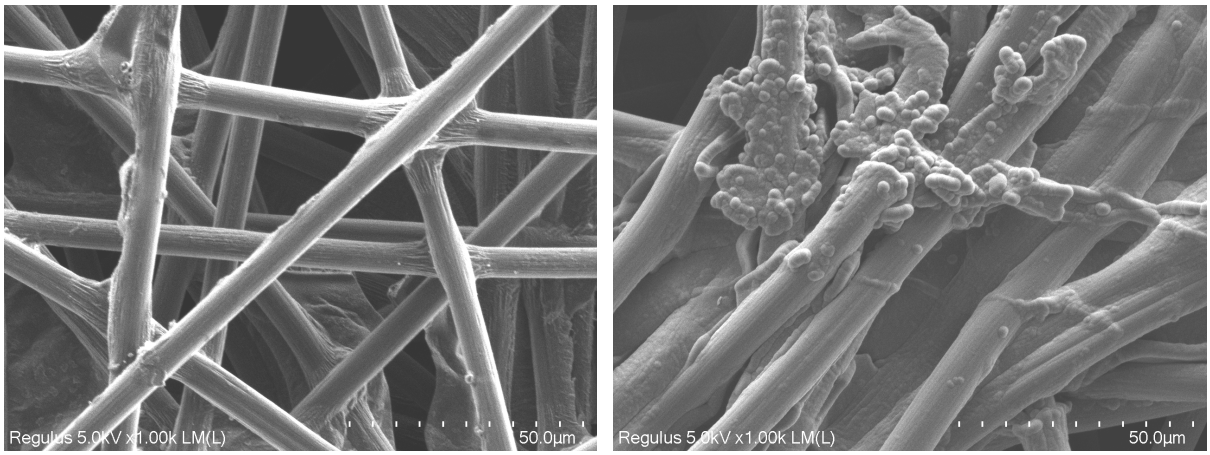

(a) **(b)**

Figure 31: SEM images of **(a)** bare CFP and **(b)** CFP with a-SiC$_x$:H deposited on it.

5.2.3 Transmission through CFP

The CFP has a porous structure as shown in the SEM pictures in Section 5.2.2. In order to determine the transmission of CFP for growth particles during a-SiC$_x$:H deposition, the CFP was mounted on top of Al foil. The transmission of the CFP is determined using the mass difference before and after deposition on both substrates. Therefore both substrates are weighed before and after deposition and the mass difference measured on the Al foil is considered the total mass transmission of the CFP.

From the SEM images we conclude that not a compact a-SiC$_x$:H layer is deposited on top of the substrate. Most of the a-SiC$_x$:H will be deposited within the porous structure of the substrate or on the metal holder underneath the substrate.

The results of the mass transmission experiment are displayed in Figure 32. In this the mass loading is plotted as a function of deposition time. Both the mass load in the CFP and on the Al foil are displayed. It can be noticed that practically all of the a-SiC$_x$:H is deposited within the CFP.

Using the ratio of deposited a-SiC$_x$:H on the Al foil compared to the total deposited a-SiC$_x$:H, being the a-SiC$_x$:H deposited in the CFP and on the Al foil, the transmission coefficient, $Tdep$, can be determined. This ratio is described in Equation 15 in which $a-\mathrm{SiC}_x:\mathrm{H}_{\mathrm{Al}}$ is the mass of the deposited a-SiC$_x$:H on the aluminum foil and $a-\mathrm{SiC}_x:\mathrm{H}_{\mathrm{Al+CFP}}$ is the total deposited a-SiC$_x$:H.

$$Tdep = \frac{a-\mathrm{SiC}_x:\mathrm{H}_{\mathrm{Al}}}{a-\mathrm{SiC}_x:\mathrm{H}_{\mathrm{Al+CFP}}} \tag{15}$$

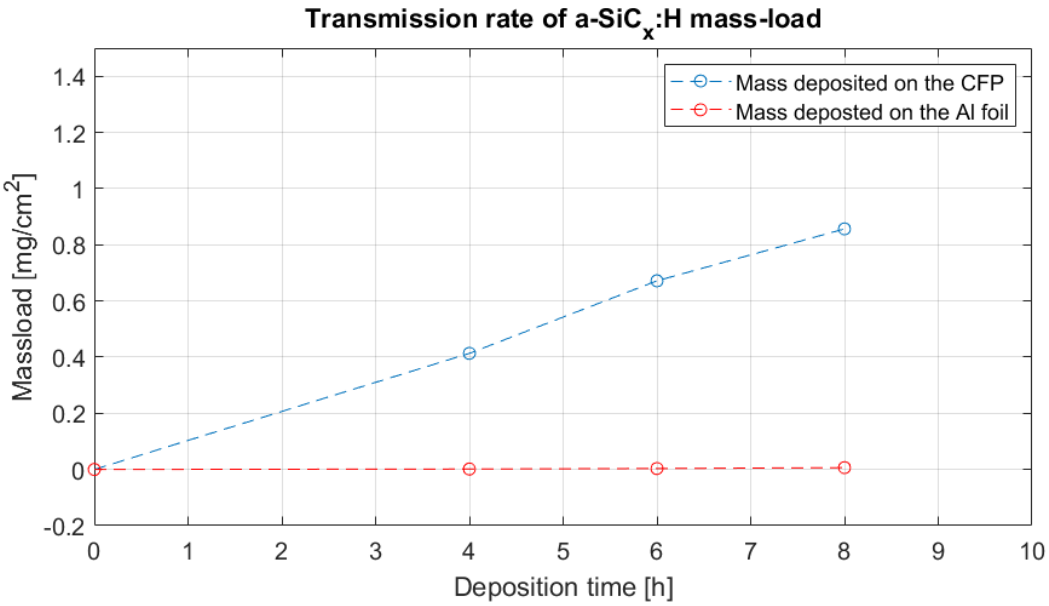

Figure 32: a-SiC$_x$:H deposited on both the CFP and aluminum foil.

Figure 32 shows the transmission of a-SiC$_x$:H through the sample is low when being compared to the deposition of a-SiC$_x$:H on the CFP itself. To emphasize this the transmission of the a-SiC$_x$:H a closer look is taken to evaluate the transmission of the CFP, this is shown in Figure 33. In this figure, it can be noticed that the transmission through the CFP is only a fractional part of the total deposition in the order of 0.75% for an 8 hour deposition.

Furthermore it can be noticed that the transmission is not linearly distributed over the complete deposition range. It can be observed that for the first 4 hours there is less transmission through the CFP compared to when an additional 4 deposition hours are added. This suggests that during the initial hours of the deposition the a-SiC$_x$:H does not penetrate to the back of the substrate, while this becomes the case for deposition periods that extend over 4 hours.

Care must be taken when making concluding remarks about Figure 33 because of the minimal mass-loads that are visible, especially when being compared to the total mass deposited during that deposition period. However, the most important conclusion that can be drawn is that more than 99% of the a-SiC$_x$:H is deposited on the CFP.

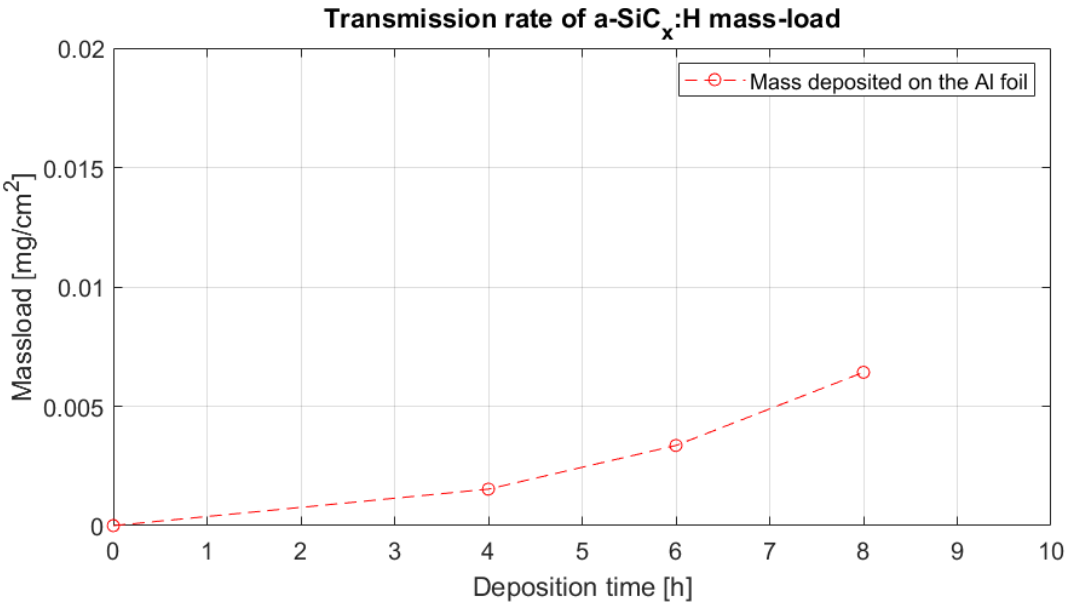

Figure 33: a-SiC$_x$:H deposited on the aluminum foil.

6 Battery test results

Various battery tests have been performed to evaluate the potential of hydrogenated amorphous silicon carbide (a-SiC$_x$:H) as an anode material. The result of these test will indicate which properties the a-SiC$_x$:H require to become a viable electrode material. First of all, the specific capacity of the deposited a-SiC$_x$:H must be characterized. This is done using a model described in Section 6.1.

Furthermore, the material should withstand cycling at specific rates, these rates range from 0.1C, charging and discharging for 10 hours, up to 1C, when charging and discharging occurs within 1 hour. During this rate capability test, the electrodes are exposed to these currents and their stability at these currents is evaluated. The results of the rate tests of the bare carbon fiber paper (CFP) electrode and the deposited a-SiC$_x$:H electrode are is discussed in Sections 6.1.2 and 6.1.3 respectively.

Besides having a stable cycling battery during the rate test the stability during longer periods must be evaluated. This stability is evaluated during a stability test. In these tests, the battery is cycled for 100 cycles at the theoretic 0.3C rate and the results of these tests are discussed in Section 6.2.

6.1 Characterizing specific capacity

The capacity of the battery can be divided into the capacity of the CFP and the deposited a-SiC$_x$:H in the anode, this is illustrated with

$$A_c = C_{CFP} \times m_{CFP} + C_{\text{a-SiC}_x\text{:H}} \times m_{\text{a-SiC}_x\text{:H}} \tag{16}$$

In this equation A_c is the areal capacity of the battery as a whole in mAh/cm^2. C_{CFP} and $C_{\text{a-SiC}_x\text{:H}}$ are the specific capacities of the CFP and the deposited a-SiC$_x$:H respectively in mAh/g. m_{CFP} and $m_{\text{a-SiC}_x\text{:H}}$ are the mass loading in the total anode of the substrate and the a-SiC$_x$:H respectively in g/cm^2.

Based on this equation it can be deduced that the capacity of the deposited a-SiC$_x$:H can be estimated by varying the amount of deposited a-SiC$_x$:H. To verify this equation a test with four different mass loads of a-SiC$_x$:H is performed. The results of a charge and discharge cycle at 0.1C, meaning 10 hours of charge and 10 hours of discharge according to the theoretical capacity of the combined substrate and deposition. This theoretical capacity consists of 350 mAh/g for the CFP [64] and 3000 mAh/g for the deposited a-SiC$_x$:H, used from experience.

For the depositions with higher carbon concentrations, this specific capacity is lower since the specific capacity of the carbon itself is in the order of 350 mAh/g as opposed to the 3000 mAh/g of the deposited silicon. However, to cycle the batteries with a similar mass-load at an equal rate they are charged and discharged the maximum theoretic capacity of 3000 mAh/g.

Furthermore, the capacity of the CFP is a substantial part of the total capacity of the anode. This causes the differences in theoretical capacity between samples with different carbon concentrations to reduce, since the capacity of the CFP is constant for these samples. Therefore the effect of using the theoretic capacity of 3000 mAh/g does not result in major test differences between the different samples.

6.1.1 Internal surface area CFP

An important assumption in the model displayed in Equation 16 is that the deposited a-SiC$_x$:H does not influence the capacity of the CFP. Therefore the theoretic capacity of both the CFP and the deposited a-SiC$_x$:H is used. This assumption can be validated by determining an estimate of the internal surface area of the CFP. After which an estimate can be made of the fraction of that surface area which will be covered by the deposited a-SiC$_x$:H.

In this estimate, the area of the substrate consists solely of the area of cylindrical carbon fibers with a 10 μ m diameter. An electrode of the CFP has a mass of 12.26 mg, when taking into account the density of the CFP, 0.5 g/cm^3, this equates to a volume of 0.025 cm^3 of CFP.

The surface area of the CFP can be defined as the surface area of a carbon fiber multiplied with the number of fibers that are in the substrate. Using the density and volume of the CFP the following relation can be deduced

$$\rho_{CFP} \times V_{CFP} = \frac{1}{4}\pi D_f^2 L \rho_g f_b \tag{17}$$

in here ρ_{CFP} and V_{CFP} are respectively the density and volume of the CFP, while D_f and L are, respectively, the diameter and the length of a carbon fiber. Furthermore ρ_g is the density of graphite and f_b are the total number of fibers.

The area of a single fiber can be defined as

$$A_f = \pi D_f L_f \tag{18}$$

Taking this into account and defining A_t as the total internal surface area, being $A_f \times f_b$, Equation 17 can be rewritten to

$$\rho_{CFP} \times V_{CFP} = \frac{1}{4} A_t D_f \rho_g \tag{19}$$

This can then be rewritten to the surface area per volumetric area of CFP in the following way.

$$\frac{A_t}{V_{CFP}} = \frac{4\rho_{CFP}}{D_f \rho_g} \tag{20}$$

Using this the surface area per volumetric are of CFP is estimated to be 900 cm^2/cm^3. In combination with the volume of the CFP the total internal surface area of the CFP is estimated to be 22 cm^2.

The amount of deposited a-SiC$_x$:H is dependent on the mass load of this a-SiC$_x$:H. A mass load of 1mg/cm^2 is assumed for this validation, this corresponds to a total a-SiC$_x$:H mass of 1.27 mg. Taking into account the density of silicon of 2.33 g/cm^3 this equates to a volumetric area of 5.4×10^{-4} cm^3.

The study for the transmission suggested that nearly all deposited a-SiC$_x$:H was deposited within the substrate with only 0.75% being deposited on the metal holder behind the substrate. This suggests that the distribution of the a-SiC$_x$:H is not uniform throughout the layers of the substrate. Because there is only marginal transmission through the substrate most of the a-SiC$_x$:H will be deposited in the top layers of the substrate. Therefore an exponential distribution is assumed for the deposition of a-SiC$_x$:H, this is illustrated in Figure 34. In this figure, an estimate of the probability that a deposited a-SiC$_x$:H particle is deposited in the substrate layer or below it is shown. This probability is 100% for the top layer of the substrate since all deposited a-SiC$_x$:H will either be deposited on this layer or be deposited deeper in the substrate. This probability decreases when moving from the top to the bottom of the substrate.

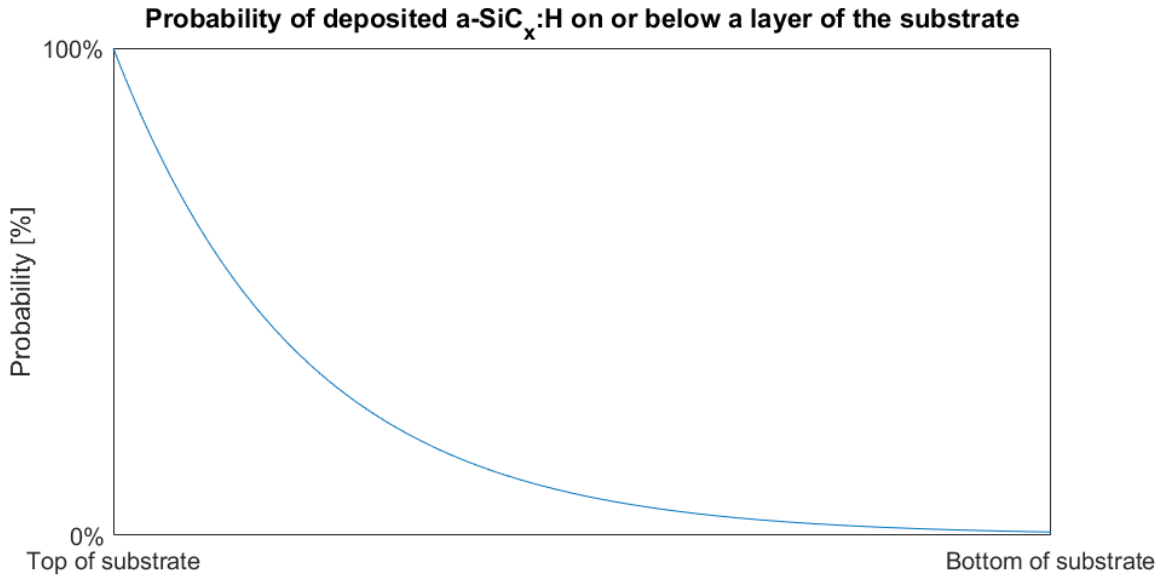

Figure 34: A schematic representation of the probability that a-SiC$_x$:H is deposited on or below the substrate layer.

Because of this exponential distribution most a-SiC$_x$:H will be deposited in the top part of the substrate, while this decreases deeper into the substrate. Even with this distribution of a-SiC$_x$:H only a fraction of the surface area of the fibers is filled with a-SiC$_x$:H deposition. From the SEM pictures, it can be estimated that the deposited a-SiC$_x$:H structures have an average thickness of 2μm. Using this observation only 12% of the fibers would be uniformly covered by the a-SiC$_x$:H. Because the a-SiC$_x$:H only covers a fraction of the total CFP surface area it can be assumed that both the theoretic capacity of the CFP and the deposited a-SiC$_x$:H can be utilized during the cycling of the battery.

6.1.2 Rate cycling CFP

The capacity of the CFP is determined using a rate test. The first part of the test consists of testing the CFP without any deposition at various rates based on the theoretic capacity. Thereby using the mass of the bare CFP anode and multiplying with its theoretic capacity to obtain the 1C charge and discharge current. The coin-cell is first cycled with two installation cycles of 0.05C, after which it is cycled for five cycles at 0.1, 0.2, 0.3 and 0.5C. This is shown in Figure 35, the vertical lines indicate the sections where a change in C-rate is made. After 17 cycles the battery is cycled at 1C for ten cycles after which the final ten cycles occur at 0.1C. These last ten cycles can be compared to the initial five 0.1C cycles to evaluate the loss in capacity that occurred during the cycling at the higher rates used in the test.

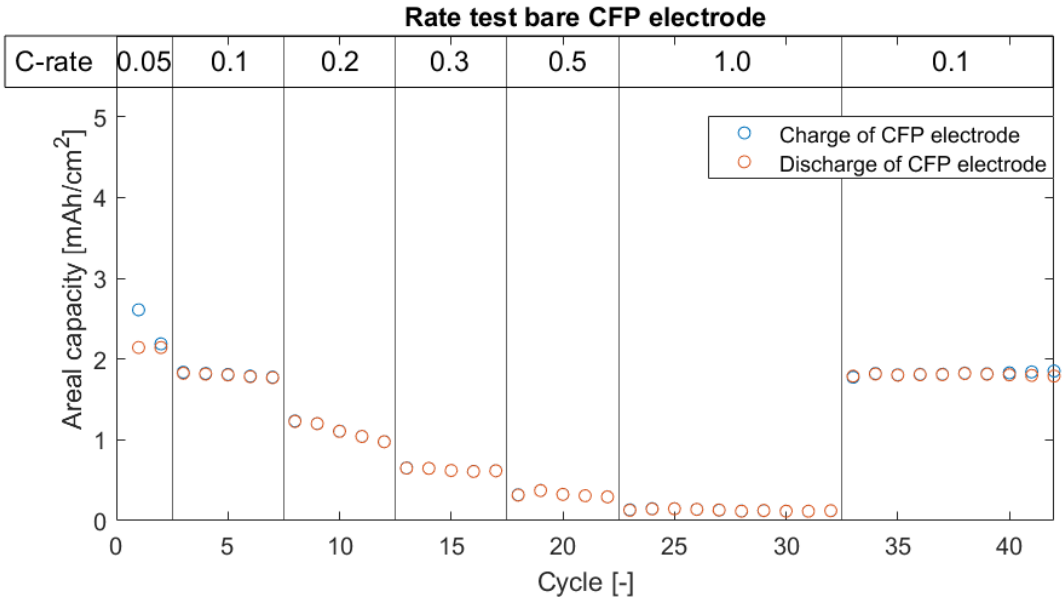

Figure 35: Cycling of the CFP electrode with various C-rates.

The CFP has a relatively stable capacity which it retains during the cycling at a specific rate. However, the capacity of the anode decreases when the anode is exposed to a higher C-rate, because the lithium has less time to be introduced and extracted from the electrodes. Therefore the insertion of the ions is not as homogeneous at high C-rates when compared to lower C-rates.

6.1.3 Rate cycling a-SiC$_x$:H and CFP

Besides the bare CFP, the deposited CFP is exposed to the same rate test. The results of this rate test are shown in Figure 36. It can be seen that the initial cycles have a stable descending capacity. This is especially visible for the cycles of 0.1C during which the capacity fades gradually. However, more variation can be noticed when evaluating the 0.2C and higher C-rates.

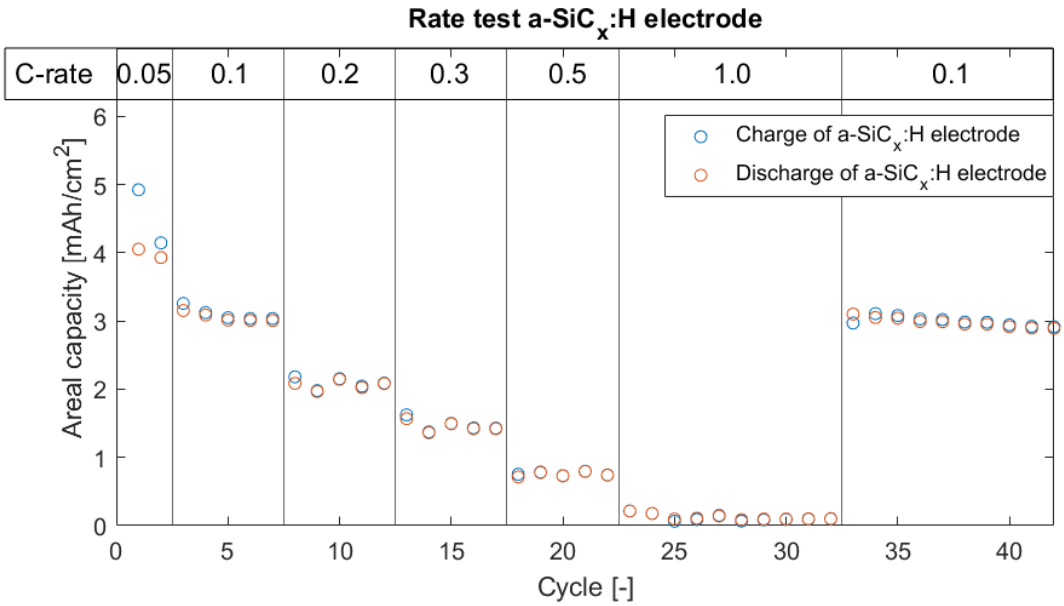

Figure 36: Cycling of the a-SiC$_x$:H with a 0.2% carbon concentration electrode at various C-rates.

For the 1C rate it can be observed that the capacity of the whole battery is very small, with areal capacity values of 0.10 up to 0.21 mAh/cm^2 during a discharge cycle. This is due to the effective rate of charging, and thereby rate of lithiation which is only 30 minutes during a cycle. According to the theoretic capacity value this should be 60 minutes. However, because the theoretic capacity of the battery is not reached for these C-rates.

The material itself is stable since the capacity of the material during the final cycles of 0.1C is in line with the capacity measured during the initial 0.1C cycles with only a difference of 0.11 mAh/cm^2 between the final cycles of both parts of the test.

6.1.4 a-SiC$_x$:H mass load variation

To evaluate the specific capacity of the deposited a-SiC$_x$:H, samples with a different mass load using the same deposition conditions are deposited. The result of the initial five cycles at 0.1C, after two installation cycles of 0.05C, is shown in Figure 37. Each data point represents the capacity of a single cycle of the electrode. It can be seen that with an increasing amount of deposited a-SiC$_x$:H the capacity of the anode is increased. Furthermore, it can be deduced that there is a fade in capacity between different cycles.

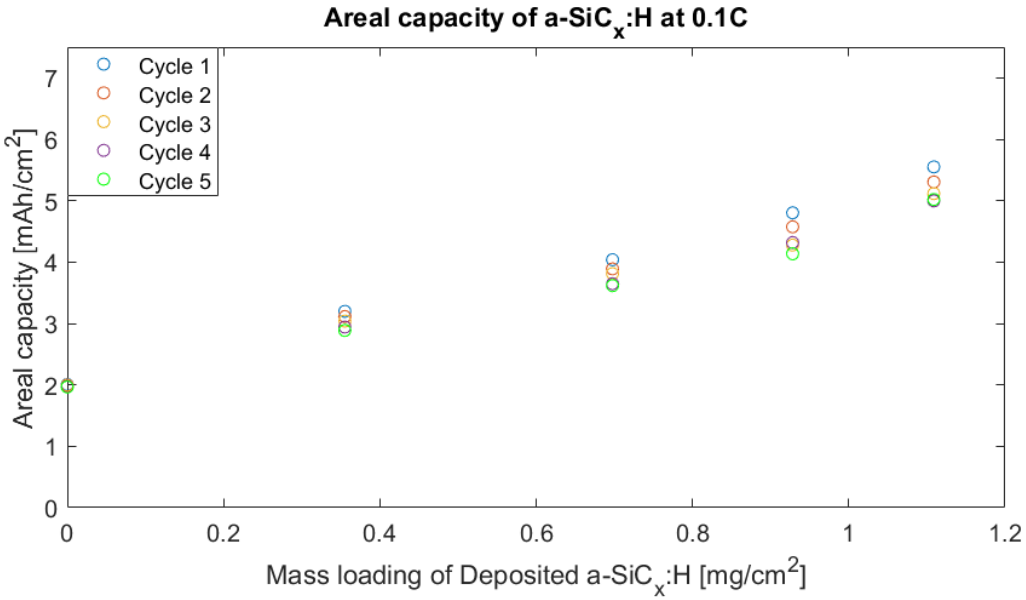

Figure 37: Variation in the mass load of deposited a-SiC$_x$:H

The capacity fade of the deposited a-SiC$_x$:H between cycles increases with increasing mass-load. For the mass-load of 1.2 mg/cm^2 the capacity difference between the initial and fifth cycle is 0.6 mAh/cm^2, a capacity fade of 14%. Nearly all capacity fade can be attributed to the fade of the a-SiC$_x$:H , because the fade of the bare CFP is only 0.04 mAh/cm^2 between the first and the fifth cycle.

The linear trend that was assumed in Equation 16 is displayed in Figure 38. This linear trend between the cycles seems to hold for different a-SiC$_x$:H mass-loads during the 0.1C rate. The slope of this trendline can be seen as the specific capacity of the a-SiC$_x$:H using the relation of Equation 16. Therefore the model of the capacity of the a-SiC$_x$:H electrode that is described in this equation is used for the remainder of the experiments.

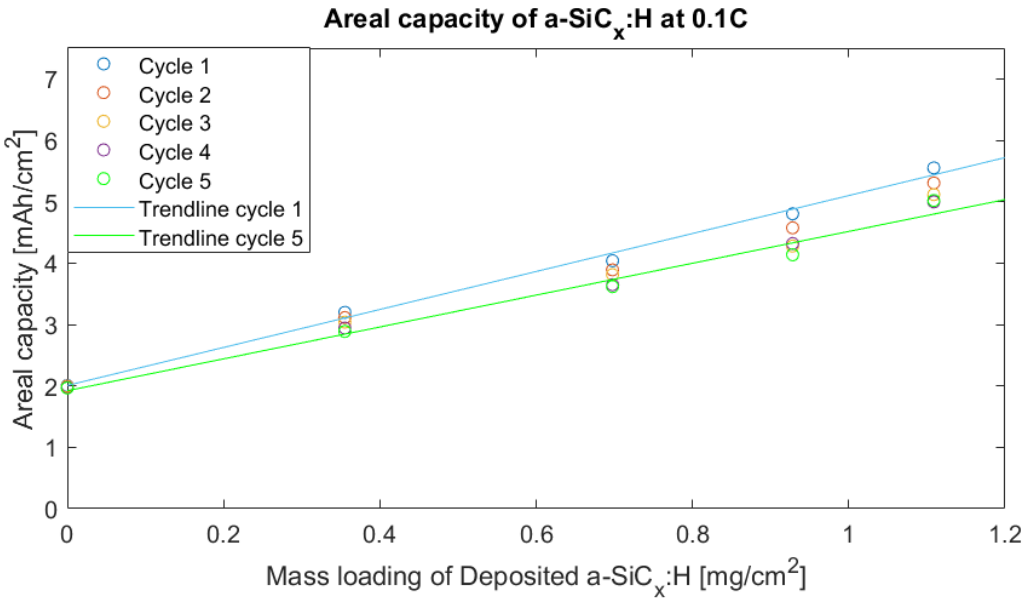

Figure 38: Variation in mass load of deposited a-SiC$_x$:H including linear trendlines between the measured capacities.

To combat the capacity loss of the a-SiC$_x$:H various strategies have been explored. One of which is the increase of the number of installation cycles of 0.05C from the initial two to five. A sample with a deposited a-SiC$_x$:H mass loading of 0.57 mg/cm^2 is cycled with these five installation cycles. The result of these additional cycles is displayed in Figure 39. When the two trendlines of the figure are interpolated the capacity of a sample with a mass loading of 0.57 mg/cm^2 can be estimated. This interpolation is used to highlight the differences between using two and five installation cycles. The areal capacity during the first cycle of is estimated to be 3.8 mAh/cm^2 with a fade to the fifth cycle of 0.36 mAh/cm^2. Two observations from this result are made, first is the stability during cycling.

When the battery is cycled with 5 installation cycles instead of 2 cycles the capacity fade between cycles is smaller and only deviates 0.10 mAh/cm^2 between the first and fifth 0.1C cycle. This deviation between the first and fifth cycle mass-load is 0.36 mAh/cm^2 according to the trendline estimation. This is a reduction of roughly 70% in capacity loss compared to the fade of those respective cycles when only two installation cycles were used.

Secondly, it can be noticed that the initial capacity that is achieved during cycling is higher. The initial cycle of the 0.57 mg/cm^2 sample has a capacity of 4.3 mAh/cm^2 while this is only 3.8 mAh/cm^2 for the trendline sample which is only subjected to two installation cycles. This increase in capacity is attributed to a more stable SEI formation on the electrode during the installation cycles, this SEI layer should be as stable as possible to achieve the highest levels of capacity, which in turn results in a increased capacity retention during cycling [65].

With the introduction of these additional cycles, the performance of the battery is increased, the initial capacity that is measured is higher while the capacity retention is also increased. Therefore these three additional installation cycles are used during the experiments of which the results will follow in this chapter.

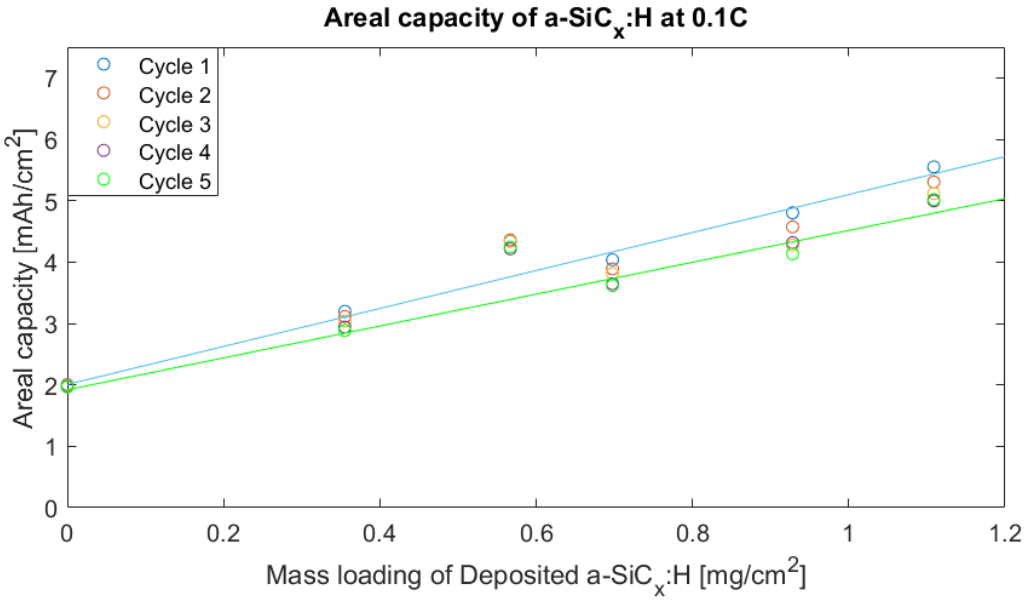

Figure 39: Additional installation cycles result in a greater initial capacity and a better retention of that capacity.

6.1.5 Rate capability 1 mg/cm^2

For this work a comparison is made between samples with a mass load of 1 mg/cm^2 for different carbon concentrations. First the rate capability of these samples is measured and the results are shown in Figure 40. From this figure, it can be deduced that the initial capacity of the samples with the 0.2% carbon concentration is the highest with a measured capacity of 4.3 mAh/cm^2 after 5 cycles of 0.1C. However, the capacity of this battery also fades faster, relative to the samples with the higher carbon concentration. This is especially visible at 0.2C and 0.3C during which the measured capacity of the 8% carbon concentration deteriorates 0.3 mAh/cm^2 while this is 0.6 mAh/cm^2 for the 0.2% carbon concentration sample. Hereby an initial estimate can be made that the samples which have a relatively high carbon concentration will operate at a more stable capacity level, having less capacity fade.

However, for the 0.5C rate the capacity of the tested batteries fluctuates while the capacity that is measured during the 1C rate is only 5-10 % of the capacity that was measured during the 0.1C rate. This indicates that for all samples the lithiation of the material is an issue at a rate of 1C. Therefore a C-rate of 0.3C was chosen for the stability experiments, during which the different batteries still have a consistent capacity. These stability experiments will be discussed in Section 6.2.

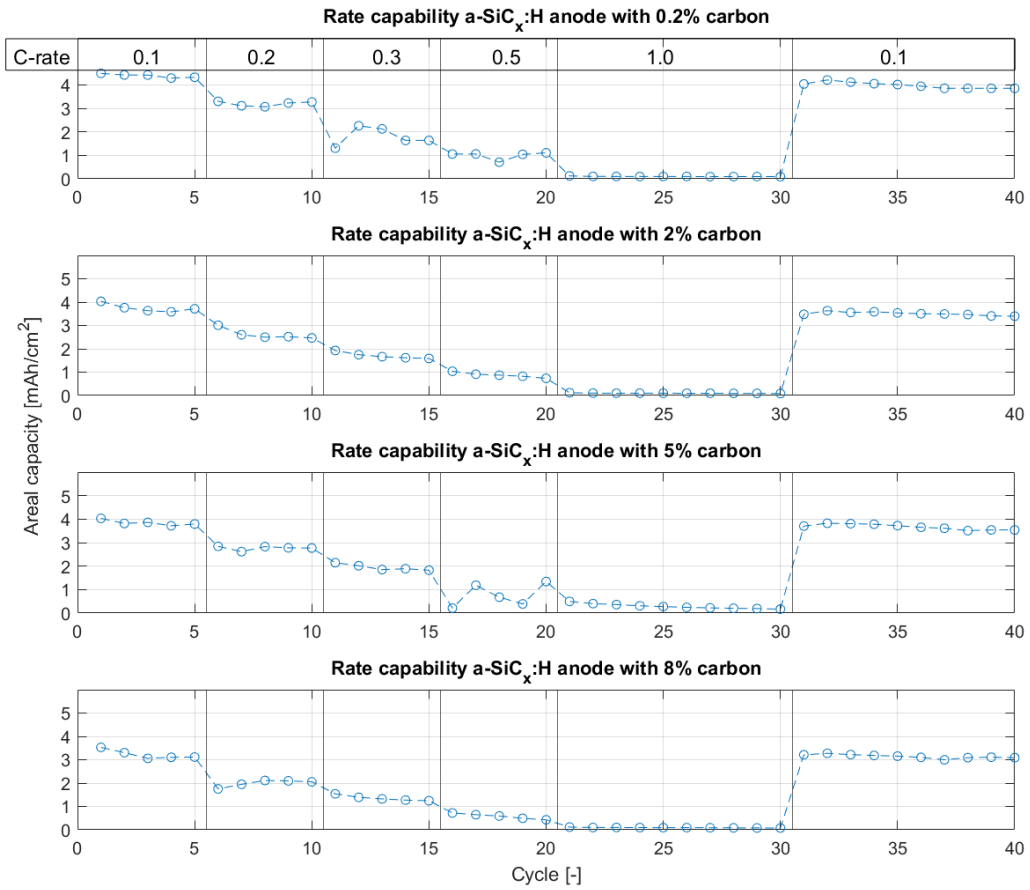

Figure 40: The performance of the different anodes during the rate capability test.

6.2 Stability experiments

After validating the model of Section 6.1 for the specific capacity of the deposited a-SiC$_x$:H during 0.1C charge it was important to see how this capacity would change with an increasing (dis)charge rate during more cycles. Therefore a stability test was designed. During this test the anode was cycled 100 times at 0.3C after being cycled for five cycles at 0.05C.

This test was performed using samples of a similar mass load of 1 mg/cm^2 with a varying carbon concentration. The carbon concentrations sampled were in the order of 0.2%, 2%,5% and 8% carbon concentration.

The results of these experiments are displayed in Figure 41. It can be observed that the lower carbon concentrations initially have the highest capacity, whereas the samples with a higher carbon concentration seem to have a more stable capacity. This can be deduced from the fade in capacity between cycle 5, when the capacity is stable after an initial drop, and 64, after which the capacity of the 0.2% carbon concentration sample drops off. This fade in capacity of the battery as whole is 36 % for the 0.2% sample, while this is only 13 % for the 8% sample.

An important note is that for some samples, for example, the sample with 8% carbon concentration, the capacity oscillates while fading. This oscillation is caused by temperature variations in the measurement room and can thus not be attributed to the fade of the battery [66].

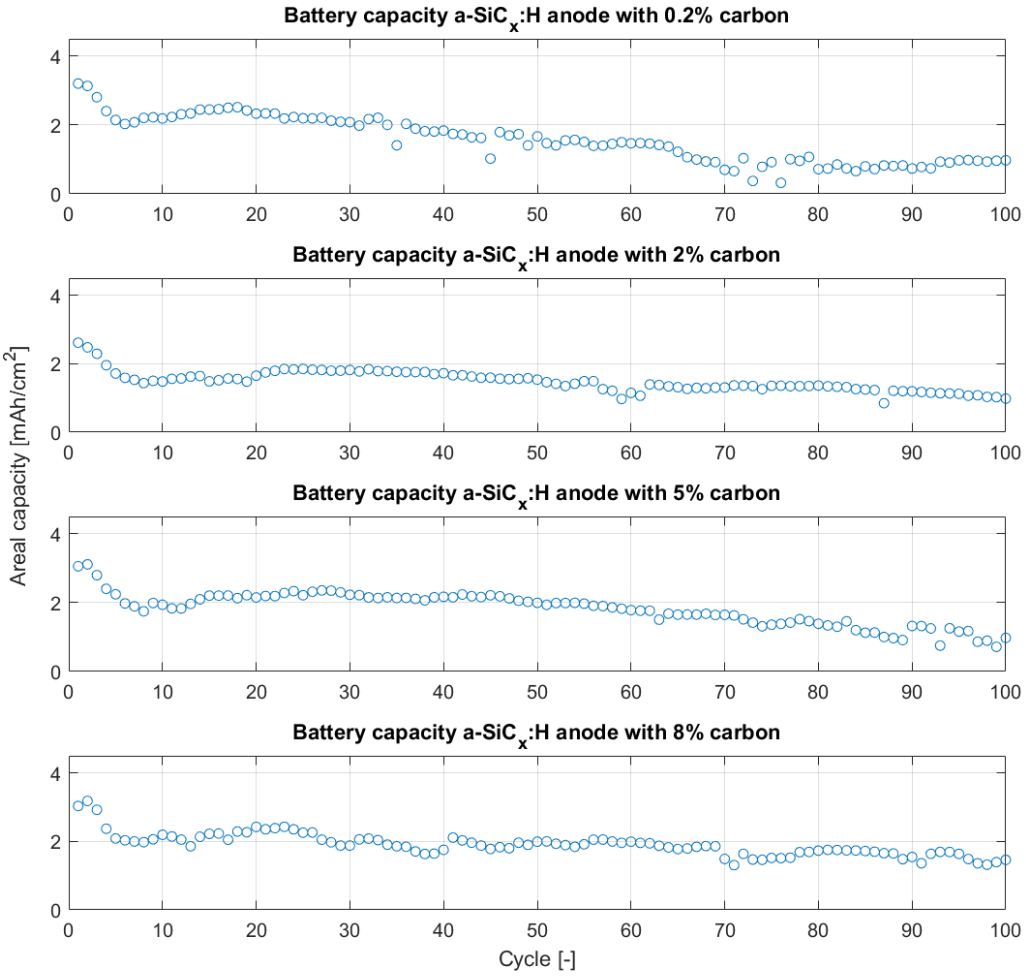

Figure 41: The measured battery capacity with various a-SiC$_x$:H carbon concentrations.

The capacity of the battery consists of both the capacity of the CFP and the deposited a-SiC$_x$:H anode. To evaluate the performance of the a-SiC$_x$:H these need to be separated from one another. Therefore the capacity of the CFP that was measured during the rate test is used to distinguish both capacities.

The fade in capacity of the CFP is relatively small in comparison to the fade in capacity of the deposited a-SiC$_x$:H. From the data of the rate test it can be concluded that the capacity of the CFP is 0.73 mAh/cm^2 at 0.3C. The rate test showed that the fade in the capacity of the CFP is marginal when it is compared to the fade in the a-SiC$_x$:H. Because of this and because the bare CFP has not been exposed to the stability test the fade is assumed to be zero. Because of this assumption the capacity of the a-SiC$_x$:H will be slightly underestimated compared to when the capacity fade of the CFP is taken into account.

When the capacity of the CFP is plotted in combination with the the total capacity of the battery it can be seen that the capacity of the deposited a-SiC$_x$:H drops off after having a substantial initial capacity. This can be seen in Figure 42, for all samples this capacity has decreased more than 50% after 80 cycles compared to the initial cycles. This can be mostly seen in the capacity of the 0.2% carbon concentration anode, while the anode with the 8% carbon concentration keeps the most capacity after being cycled 100 times. The figure also shows the large decay of all anodes, initially having more than two-thirds of the total capacity of the battery down to having a fraction of the capacity of the CFP.

The 8% carbon concentration sample retains the most capacity from the samples tested with a measured capacity of 1.8 mAh after 100 cycles, in comparison the CFP has a capacity of 0.93 mAh. Therefore the capacity of the deposited a-SiC$_x$:H is still 48% of the capacity of the total battery. In contrast, the capacity of the 0.2% sample is 1.2 mAh on average during the final 10 cycles of the test, this is only 22% of the capacity of the battery as a whole.

However, it is important to note that all batteries are cycled with a constant current, which is based on the theoretic capacity of the battery. When the battery is cycled with 0.3C the battery is theoretically cycled with 3.33 hours of charge and discharge cycles, in practice however this time is much shorter, in the order of 1.5-2 hours. Taking into account the data of Figure 36, in which it is shown that the capacity of the battery decreases when it is exposed to a higher cycling rate this effectively means that decay of the battery is not only due to internal structure changes but also due to in effect cycling the battery at a higher C-rate.

This in turn implies that the capacity of the CFP is smaller because of the higher (dis)charge rate. However, this change in capacity is not taken into account because of limited CFP test results. Therefore the capacity of the CFP is slightly overestimated while the capacity of the a-SiC$_x$:H is slightly underestimated. This becomes most prominent for the last 30 cycles of the test.

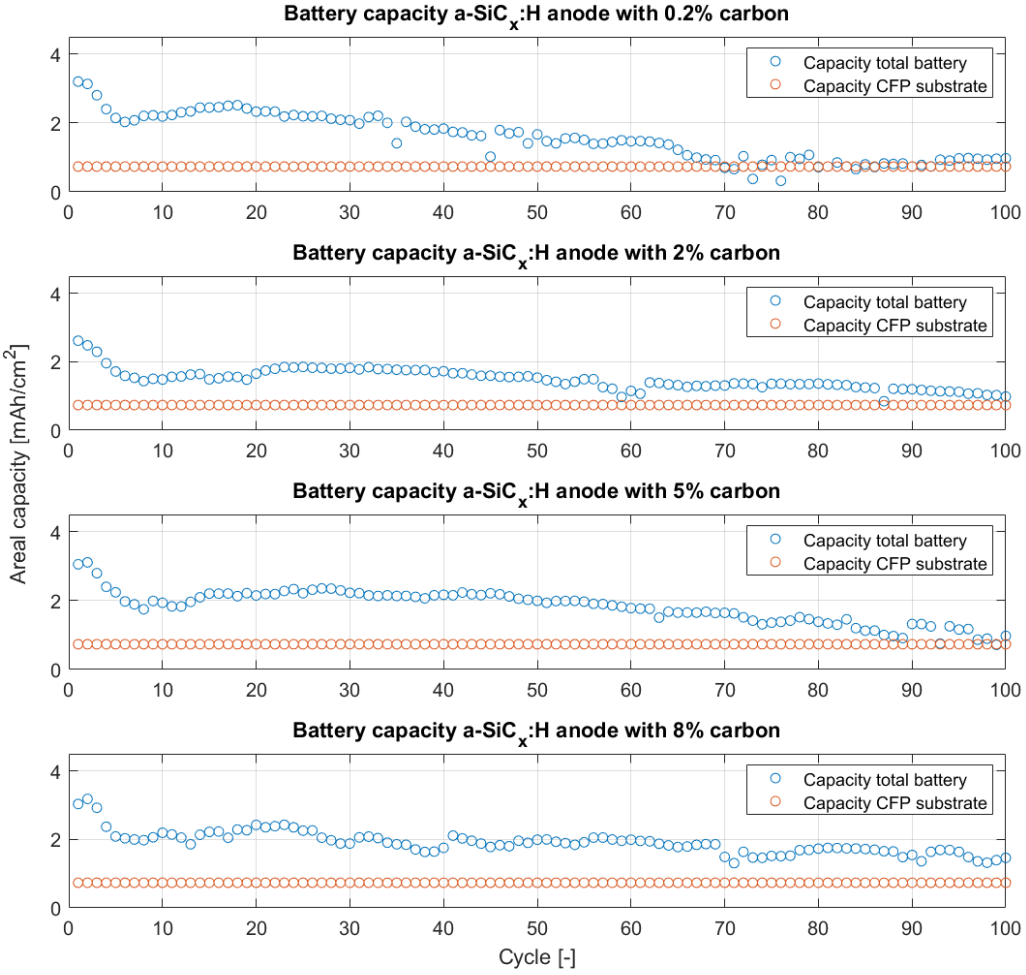

Figure 42: The measured battery capacity with various a-SiC$_x$:H carbon concentrations including the separate CFP capacity.

The trend of a higher initial capacity with a faster decay for the samples with the lower carbon concentrations is also visible in the calculation of the specific capacities of the respective anodes. This specific capacity is determined using the difference in mass between a deposited anode and a bare CFP anode. Using a scale with an accuracy of 0.01mg the specific capacity can be determined with a relative error of 0.014mg.

With an initial specific capacity of 3170 mAh/g, the 0.2% carbon concentration anode has the highest specific capacity of all anodes. However, this specific capacity fades the most during cycling, as can be seen in Figure 43. In this figure, the change in specific capacity of the four tested samples is visualized. The error margin that results from the mass measurement is smaller than the marks used in the figure, therefore they are not displayed. The specific capacity fades similarly as the capacity fade in the whole battery, thus including the CFP. This is because the capacity fade in the CFP is assumed to be zero during the cycling.

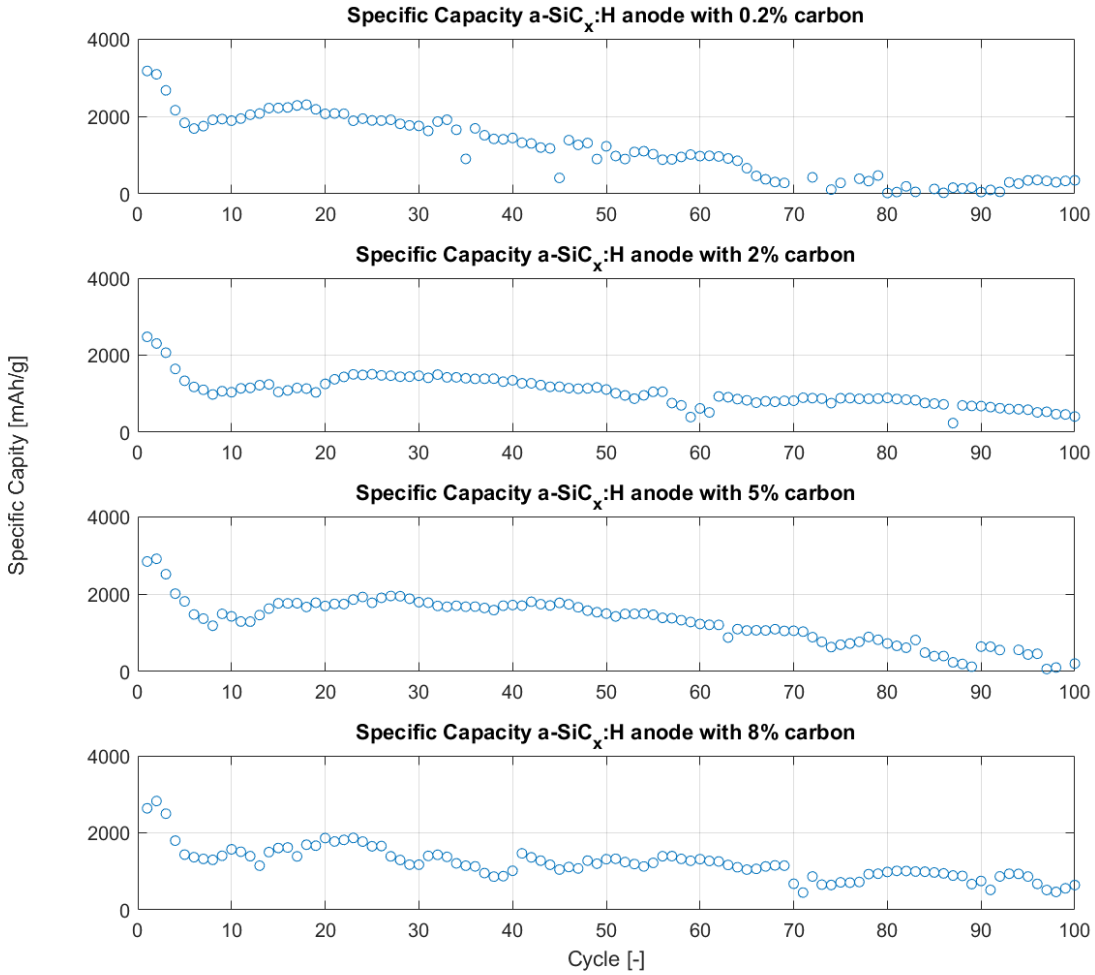

Figure 43: The specific capacity of the various a-SiC$_x$:H carbon concentrations tested during the stability test.

From Figure 43 it can be deduced that the a-SiC$_x$:H anode specific capacity of the 0.2% carbon concentration sample is nearly completely faded during the last 30 cycles with only 10% of the initial specific capacity that is retained.

The 2% carbon concentration sample has better capacity retention with a capacity of 15% of the specific capacity after cycling 100 times.

The specific capacity of the 5% carbon concentration is well retained during the initial 50 cycles of the test after which it decays at a quicker rate. This causes the battery to have a capacity retention of roughly 13% on average during the last 10 cycles. Thereby not outperforming the 2% carbon concentration sample. However, during the initial 50 cycles this sample does outperform the tested 2% carbon concentration sample. Thereby supporting the observation that an increased carbon concentration aids the stability of the battery and therefore increases capacity retention.

The 8% carbon concentration sample retains the highest specific capacity from all samples tested. With a capacity retention of 21 % during the final 10 cycles of the test the performance of this sample is significantly better when being compared to the other test samples. Thereby an initial conclusion can be drawn that for a stable cycling material a carbon concentration in the order of 8% or more is required to have a stable cycling material.

6.2.1 Charge and Discharge cycles

Individual charge and discharge cycles give an insight into the differences in the cycling process between the different samples. All samples are cycled using the same boundary conditions, the most important boundary conditions are the voltage levels of a completely charged and discharged battery.

According to the experiments, a battery is completely charged when the battery reaches a voltage level of 1.5 V. On the contrary, the battery is completely discharged when a voltage level of 0.01 V is reached. A representation of such a voltage cycle is displayed in Figure 44. In this figure, the first 0.1 C cycle, after five installation cycles, of the CFP is displayed. In this figure the charge cycle can be recognized by the increase in voltage level with increasing capacity. The discharge cycle follows an opposite relation, with a decrease in voltage while the capacity is discharged.

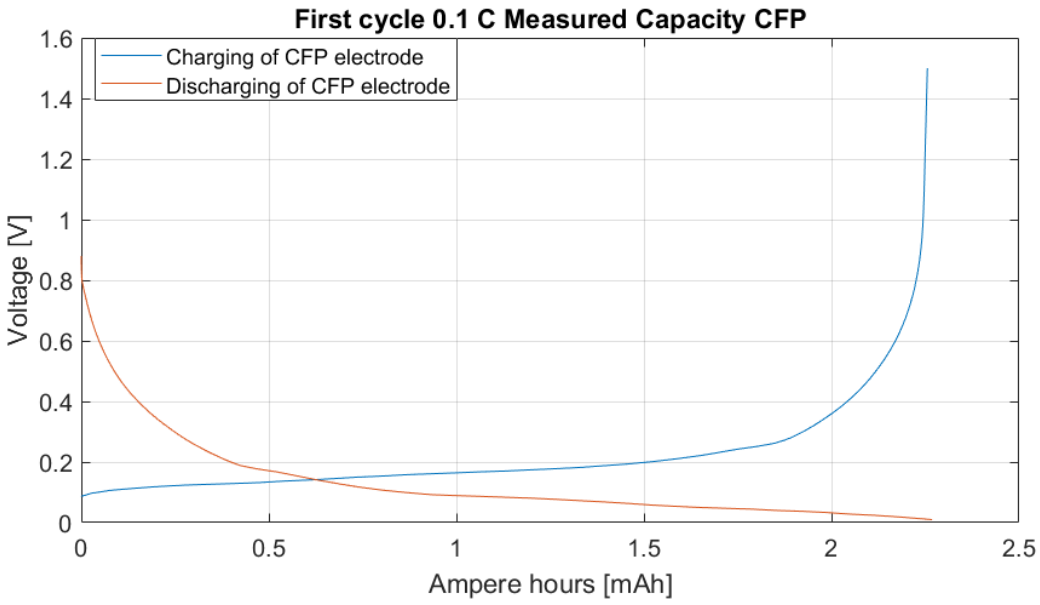

Figure 44: The initial 0.1C charge and discharge cycle of the CFP electrode.

From the figure, it can be deduced that most of the capacity is charged into the battery in the voltage window of 0.1 V to 0.3 V whereafter the voltage in the battery rises steeply to reach the completely charged voltage of 1.5 V. During the discharge it can be observed that discharge does not start with the fully charged voltage level of 1.5V. This is because of the rest period that the battery is subjected to after complete charging. During this period no external current is applied and the battery reaches a stable voltage. When the battery is discharging it can be

observed that 80% of the capacity is retrieved in the voltage window from 0.2 V to 0.01 V.

Furthermore, it can be noticed that the battery does not have a voltage plateau and thereby a fixed operating voltage. This is ascribed to the lithium alloying mechanism that occurs during charging and discharging. At each stage of lithiation, the Si- and Li-ions form a solid solution phase, resulting in a gradually decreasing voltage curve.

In Figure 17 the charging and discharging cycles are shown for the CFP as well as for the coin cells of CFP with deposited a-SiC$_x$:H. When a charging and discharging cycle of a CFP with deposited a-SiC$_x$:H is compared to the bare CFP discharge curve, it can be observed that the capacity that is stored in the CFP is only a fraction of the total capacity. Furthermore, it can be noticed that the charging of the deposited substrate occurs in the voltage window of 0.1 V up to 0.6 V, which is an extension of the voltage window of the bare CFP during cycling. It should be noted that the axis of this figure covers a greater capacity compared to the charging and discharging cycles of the CFP.

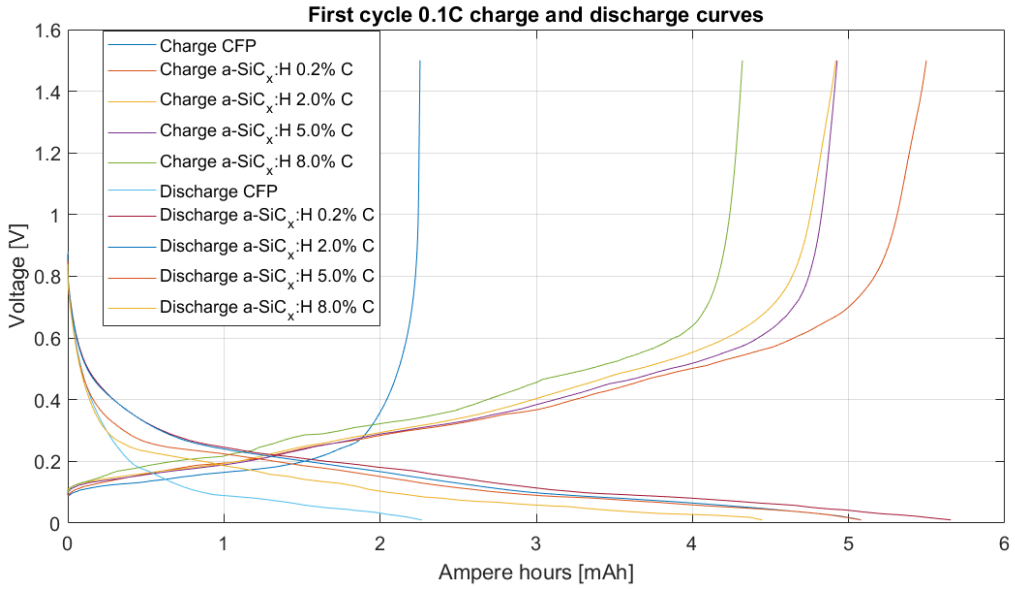

Figure 45: The charging and discharging curve of the initial 0.1C cycle of the rate test.

Besides the differences between the bare CFP and the deposited CFP there are also differences between the different deposited electrodes. The first difference that can be observed is the difference in capacity in the charging voltage window from 0.1 to 0.6 V. The 0.6 V is reached at the highest capacity by the 0.2% carbon concentration sample, therefore the most energy can be stored in this sample. The 8% carbon concentration stores the least amount of energy. In this case, the sample with 2% carbon concentration has a similar capacity when compared to the 5% carbon concentration sample.

In Figure 46 the same batteries are shown during the fifth 0.1 C cycle, it can be seen that the charging curves of the different batteries have shifted towards the left of the figure, this shift represents the fade in capacity. The capacity of all samples fade, but with this limited data set conclusions about stability can not be drawn. For example, the sample with an 8% carbon concentration fades the most in this case while this is assumed to be the most stable material.

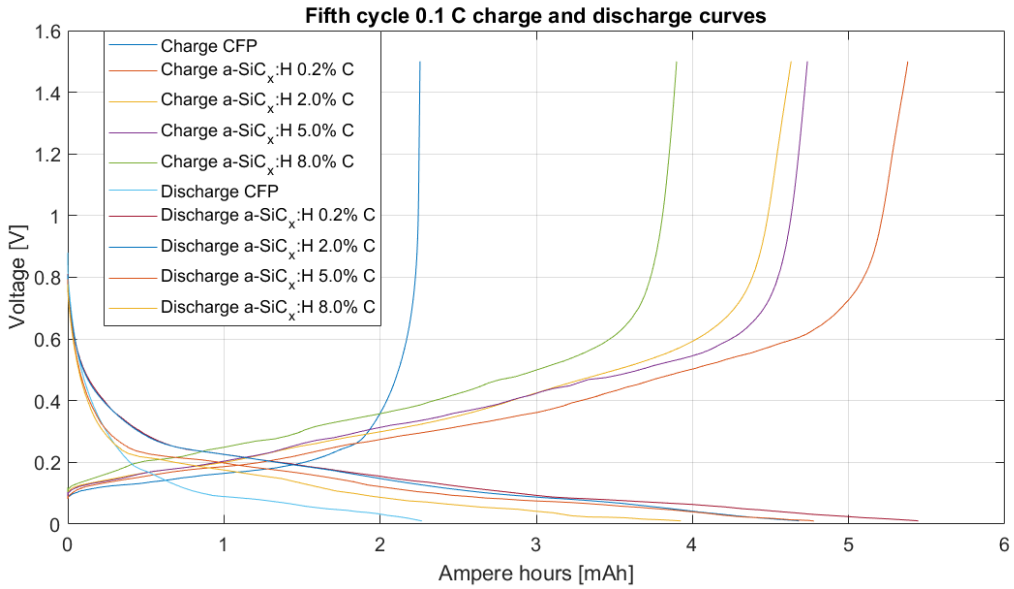

Figure 46: The charging and discharging curve of the fifth 0.1C cycle of the rate test.

To evaluate the stability of the samples the charging and discharging curves of the stability test are evaluated. The cycles that are analyzed are cycles 5 and 64. During the fifth cycle, all samples have reached a stable capacity level after the initial drop in capacity, while the capacity fade of the batteries follow a similar trend up to cycle 64, after which the 0.2% anode capacity drops off sharply. In Figure 47 the charging and discharging curves of the fifth cycle is shown, when the capacity becomes stable. Compared to the charge and discharge curve of the batteries cycled at 0.1C it can be noticed that the maximum capacity is lower, in general a decrease of 23%. This decrease highlights the effect of a different C-rate on the capacity of the battery.

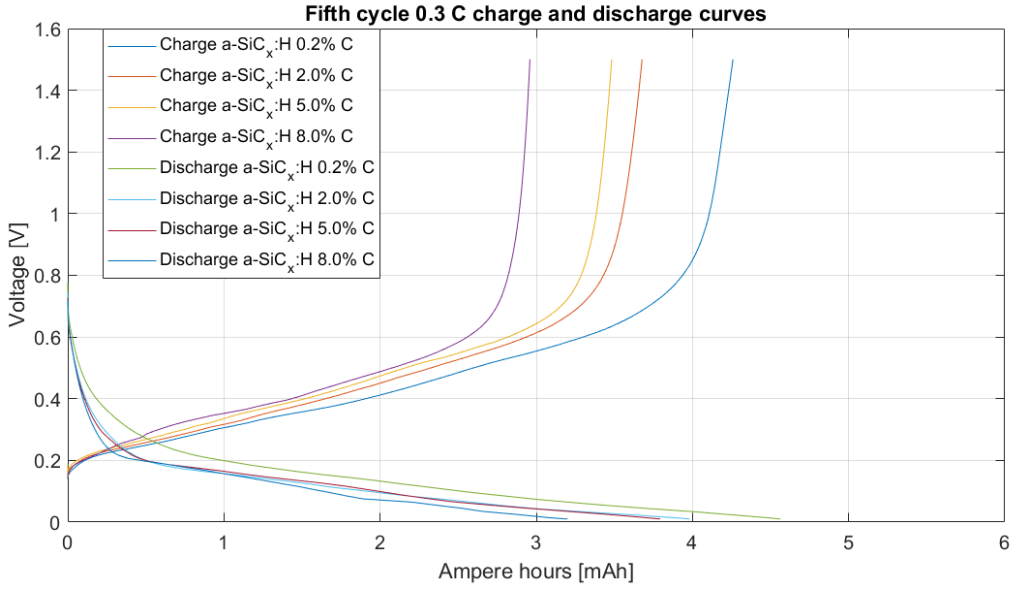

Figure 47: The charge and discharge curve of the fifth 0.3C cycle of the stability test.

When the 64th cycle is compared to the fifth cycle it can be observed that the reduction in capacity measured of all batteries is almost 50%. The smallest decay in capacity is that of the 8% carbon concentration sample, whose capacity decreases 35%, while the largest decays in capacity are that of the 0.2% and the 2% carbon concentration samples. The voltage window during which the battery is charged and discharge of the 64th cycle is similar to that of the fifth cycle, however the amount of energy that is introduced and retrieved from the battery is significantly smaller.

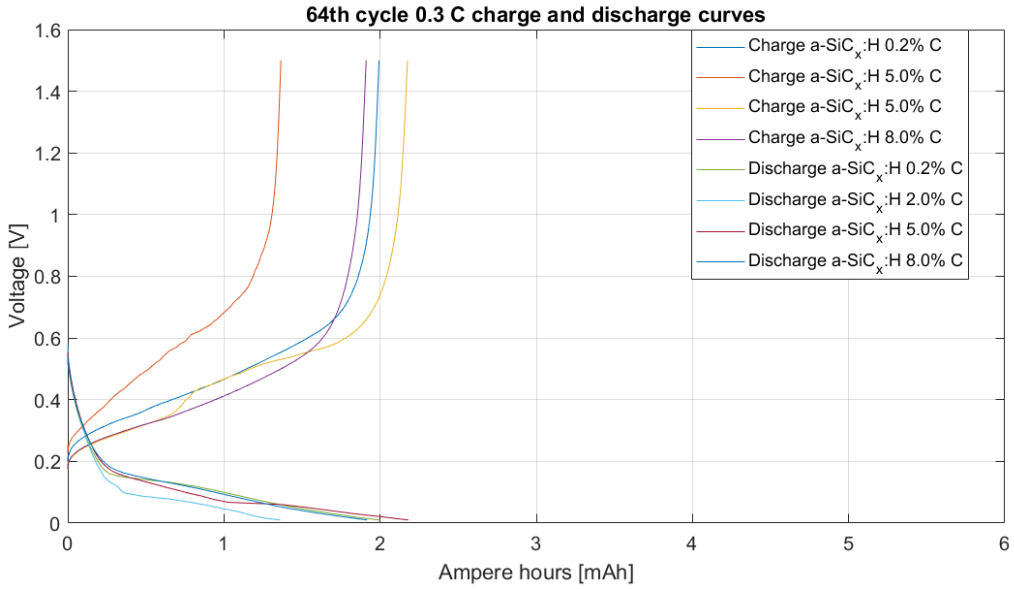

Figure 48: The charge and discharge curve of the 64th 0.3C cycle of the stability test.

The results indicate that a battery with a high carbon concentration, in this case, the 8% sample has a better capacity retention when compared to batteries with low carbon concentrations, in this work 0.2% and 2%. Because only limited amounts of coin-cell batteries have been cycled conclusions on absolute capacity retention cannot be made due. However, the trend that the capacity fades less when the carbon concentration is increased from 0.2% to 8% is clear.

Lastly, it is once again important to note that during these experiments the porosity of the samples differs with varying carbon concentrations. This has to be taken into account when drawing definitive conclusions about the material with the least capacity fade.

7 COMSOL model

As shown in the experimental section of this thesis hydrogenated amorphous silicon carbide a-SiC$_x$:H can be a viable option as an anode material in lithium-ion batteries. However, due to time limitations, only a limited number of experiments can be done in the given timeframe. Each battery experiment takes several weeks when taking into account the 5 installation cycles of 0.05C and the test cycles themselves.

Therefore, to estimate the potential of this material further, a COMSOL model is made in which a representation of the experimental setup is made. This will allow for a greater variety of material properties to be observed and tweaked more easily. Also, longer cycling times and a greater variety of (dis)charging speeds can be assessed. Furthermore individual parameters of the model can tuned. During the experiments individual parameters, like the fraction of carbon and the porosity of the sample, were dependent. These can be decoupled in the model to evaluate the individual effect on the capacity of the battery of these parameters.

7.1 Model definition

The COMSOL model used in this research is a combination of two models from the COMSOL libraries, which are '1D Lithium-ion battery Model for Capacity Fade' [67] and '1D Lithium-Ion Battery with Multiple Intercalating Electrode Materials' [68]. The capacity fade model, as the name suggests, explores the fade in capacity of a lithium-ion battery due to extended cycling. This model can be evaluated for both a great number of cycles and single-cycle behavior. The multiple intercalating electrode material model is focused on the battery performance when varying the composition of materials in one of the electrodes. In this case, this is a variation in the material of the cathode with components of silicon and a graphite anode. This way both material of the a-SiC$_x$:H cathode are represented in the model, with the carbon fiber paper (CFP) and the carbon concentration of the a-SiC$_x$:H being represented by the graphite anode and the silicon of the a-SiC$_x$:H by the silicon anode.

The principles and equations of the 1D capacity-fade model will be discussed in Section 7.1, whereafter the principles of the 1D multiple intercalating materials will be discussed in Section 7.1. Next, the individual parts and boundary conditions of the model are described.

1D capacity-fade model

The 1D capacity-fade model that is used as a basis of the COMSOL simulations is displayed in Figure 49. In this figure, the three main parts of the battery model are shown, the porous a-SiC$_x$:H cathode, the separator, and the lithium metal anode. The parameters of the a-SiC$_x$:H cathode can be altered to represent the cathodes used during the experiments.

Figure 49: The 1D COMSOL battery model, consisting of a porous a-SiC$_x$:H cathode, a separator and a lithium metal anode [38].

The 1D capacity-fade model is based on three main equations that describe the electrochemical reactions during charging and discharging of the battery. First the current density of the solid electrolyte interface, i_{SEI} (in A/m^2) is calculated using the following equation [67]:

$$i_{loc,\text{SEI}} = -(1+HK)\frac{J_{i_{Ioc,1C,ref}}}{\exp\left(\frac{\alpha\eta_{\text{SEI}}F}{RT}\right) + \frac{q_{\text{SEI}}fJ}{i_{Ioc,1C,ref}}} \tag{21}$$

In Equation 21 the following parameters are used:
HK is the dimensionless expansion factor.
$J_{i_{Ioc,1C,ref}}$ is the dimensionless exhange current density for the parasitic SEI reaction.
α is the transfer coefficient for electrochemical reduction reaction.
η_{SEI} is the overpotential, in reference to the equilibrium potential of 0V versus lithium.
F and R are the Faraday and the gas constant respectively.
T is the temperature at which the battery is cycled.
q_{SEI} is the local accumulated charged due to SEI formation.
f is the lumped non dimensional parameter which is based on the properties of the SEI film.

This result is used in Equation 22 to calculate the formation rate of the solid electrolyte interface layer, $\partial c_{SEI}/\partial t$ [67]:

$$\frac{\partial c_{\text{SEI}}}{\partial t} = -\frac{v_{SEI} i_{I_{loc,\text{SEI}}}}{nF}, \tag{22}$$

in here, v_{SEI} is the stoichiometric coefficient of the SEI species in the reaction, and n is defined as the number of electrons that take part in the reaction. This rate of formation of the solid electrolyte interface is proportional to the rate of consumption of Li^+ ions [69]. The result is then used to calculate the Li^+ consumption (in C/m^2) that is related to the capacity loss of the battery [67]:

$$q_{\text{SEI}} = \frac{Fc_{\text{SEI}}}{A_v}. \tag{23}$$

In here, q_{SEI} is the local accumulated charge due to the formation of SEI, while A_v is the electrode surface area.

1D lithium-ion battery with multiple intercalating electrode materials

Previous modeling work by Wang [38] simplified the simulations by only taking into account the contribution of the silicon in the a-SiC$_x$:H. In this way he was able to only use the 1D capacity-fade model. By varying certain parameters the effect of porosity and carbon concentration were implemented, but the CFP was neglected during modeling.

To improve the simulation of the performed experiments the multiple intercalating-electrode-material model is added. Using the 1D lithium-ion battery with multiple intercalating-electrode-material model an electrode consisting of multiple materials can be simulated. In the experiments of this research, the cathode of the half-cell test is a-SiC$_x$:H deposited on CFP. To represent this in the model a fraction of the porous cathode is made from graphite, while the remainder of the porous electrode is made from silicon.

The porosity of the electrode is defined as the volume fraction of electrolyte that is in the cathode. The carbon concentration, in combination with the CFP, is defined as the volumetric fraction of graphite in the electrode.

Electrolyte

The electrolyte used in this model is the $LiPF_6$ in a 1:1 volume ratio, which is also used during the experiments. This electrolyte is predefined in the COMSOL library and can be imported directly into the model. The electrolyte used in the experiments also contains some additives

such as vinylene- and fluorethylane carbonate. In the model, the concentration of the electrolyte is set to be 1000 mol/m^3, which is similar to the experimental concentration.

In the experiments, the electrolyte is placed in contact with both the anode and the cathode of the battery and thus also with the separator. Therefore the electrolyte is set to be present in every domain of the battery model, thereby thus in the porous cathode and the separator. The concentration of the electrolyte is described by [70]:

$$N_+ = \left(-D_2 + \frac{2k_2 t_+ t_- RT}{c_+ z_+ F^2}\right)\left(1 + \frac{\partial \ln(f_\pm)}{\partial \ln(c_2)}\right)\nabla C_+ - \frac{k_2 t_+}{z_+ F}\nabla\phi_1 \tag{24}$$

$$N_- = \left(-D_2 + \frac{2k_2 t_-^2 RT}{c_- z_- F^2}\right)\left(1 + \frac{\partial \ln(f_\pm)}{\partial \ln(c_2)}\right)\nabla C_+ - \frac{k_2 t_-}{z_- F}\nabla\phi_1 \tag{25}$$

In these equations the following parameters are used:
N_+ is the positive ion molar flux in the electrolyte.
N_- is the negative ion molar flux in the electrolyte.
D_2 is the Li^+ diffusivity in the electrolyte.
k_2 is the ionic conductivity.
t_+ is the transport number of the positive ions.
t_- is the transport number of the negative ions.
c_+ is the positive ion concentration.
c_- is the negative ion concentration.
z_+ is the charge number of the positive ions.
z_- is the charge number of the negative ions.
$f_\pm$ is the average molar activity constant.
$\nabla\phi_1$ is the electrical potential of the cathode.
c_1 is the Li^+ ion concentration in the cathode.

The current density in the electrolyte is displayed in the following

$$i_l = (-\sigma_1 \nabla\phi_1) + \frac{2\sigma_1 RT}{F}\left(1 + \frac{\partial \ln(f)}{\partial \ln(c_1)}\right)(1 - t_+)\nabla \ln(c_1). \tag{26}$$

In here, i_l is the electrolyte current density and σ_1 is the stress in the Si electrode [71].

Cathode

During the half-cell test the cathode is made up of a-SiC$_x$:H . This material is not included in the COMSOL library. However, using the multiple intercalating-electrode-material model an electrode consisting of both carbon and silicon can be simulated. Both the carbon in the a-SiC$_x$:H and the CFP substrate is taken into account when determining the total fraction of carbon in the electrode.

The total volume fraction of carbon in the electrode is determined by taking the mass of the CFP and determining the volume of the carbon fibers. The volume of the deposited a-SiC$_x$:H is determined using the mass-load of the sample. A mass load of 1 mg/cm^2 used to determine this volume. The carbon concentration of the a-SiC$_x$:H can be simulated by adding the volume fraction of the a-SiC$_x$:H to the volume fraction of the CFP.

At the cathode of the model lithiation reactions 27 and 28 occur:

$$x\mathrm{Li}^+ + \mathrm{Si} + x\mathrm{e}^- \rightarrow \mathrm{Li}_x\mathrm{Si} \tag{27}$$

$$\mathrm{Li}^+ + \mathrm{e}^- + 6\mathrm{C} \leftrightarrow \mathrm{LiC}_6 \tag{28}$$

Besides this lithiation of the porous electrode, the parasitic formation of the Solid Electrolyte Interface (SEI) layer is simulated using the following relation

$$S + \mathrm{Li}^+ + \mathrm{e}^- \rightarrow P_{SEI} \tag{29}$$

In here, S is the electrolyte, and P_{SEI} is the SEI that is formed in the reaction with the electrolyte

The Li^+ insertion and diffusion into the cathode is described by the Baker-Verbrugge law. The chemical reaction between Si and the Li^+ ions is described by the Butler-Volmer equation [72].

$$i_c = i_0 \left[\exp\left(\frac{\alpha_a \eta F}{RT}\right) - \exp\left(\frac{-\alpha_c \eta F}{RT}\right) \right] \tag{30}$$

In here:
i_c is the transfer current density at cathode/electrolyte interface
i_0 is the exchange current density at cathode/electrolyte interface
α_a is the negative charge transfer coefficient
α_c is the positive charge transfer coefficient
η is the over-potential
The over-potential is described as:

$$\eta = \phi_2 - \phi_3 - U, \tag{31}$$

in which ϕ_2 and ϕ_3 are the potentials of the solid phase and the electrolyte phase, respectively. U is the equilibrium potential of the silicon and graphite composite [73].

Time-acceleration factor

To model the cycling process for a higher number of cycles a time-acceleration factor is introduced. This time-acceleration factor τ is introduced in the SEI formation reaction in the following equation [67]:

$$(\tau - 1)S + (\tau - 1)\text{Li(s)} \rightarrow (\tau - 1)P_{SEI}. \tag{32}$$

By using this time acceleration factor the number of cycles per computation is increased. If simulation of singular cycles is desired this factor should be decreased to 1. While simulating 30 cycles at once can be done with a value of 30 for τ.

Anode

During experiments the anode is made out of a lithium metal plate. In the COMSOL model, a representation of this lithium metal plate is made using an electrode surface. The reactions that occur on this anode are

$$Li^+ + e^- \rightarrow Li \tag{33}$$

$$Li \rightarrow Li^+ + e^- \tag{34}$$

Like the reaction kinetics of the cathode, the reaction kinetics of the anode can be described using the Butler-Volmer equation [72]:

$$i_a = i_0 \left[\exp\left(\frac{\alpha_a \eta F}{RT}\right) - \exp\left(\frac{-\alpha_c \eta F}{RT}\right) \right] \tag{35}$$

In here:
i_a is the transfer current density at anode/electrolyte interface
i_0 is the exchange current density at anode/electrolyte interface
α_a is the negative charge transfer coefficient
α_c is the positive charge transfer coefficient
η is the over-potential

7.1.1 Boundary conditions

No flux

Li^+ ions cannot move through the current collector at the boundary between the electrode and the current collector. Therefore a no-flux boundary condition is applied:

$$N_+ = N_- = 0 \tag{36}$$

Insulation

As electrons do not enter the electrolyte the boundaries and interfaces of the electrolyte have an insulation boundary condition. $\vec{i_l}$ and $\vec{i_s}$ represent the current at the surface of the electrolyte and the electrode. $\vec{n}$ is the normal vector perpendicularly oriented to the electrolyte and the electrode surface.

$$-\vec{n} \cdot \vec{i_l} = 0 \tag{37}$$

$$-\vec{n} \cdot \vec{i_s} = 0 \tag{38}$$

Cycling

During the simulation the battery is charged and discharged. The current with which the battery is cycled is determined to be 0.3C. Furthermore, the battery is initially discharged, as was done during the experiments.

Electrode surface

The lithium metal anode is simulated as a lithium electrode surface. This is done because the lithium metal is highly conductive for electrons and for the diffusion of Li^+ ions. This results in the effect that the thickness of the lithium anode can be ignored. Therefore, the anode can be modeled as a surface electrode.

7.1.2 Modeling

After the model was built, it was desired to validate the results that were retrieved during the experiments. This was done both using singular cycles and batches of multiple cycles. This was done by varying the time-acceleration factor parameter in the model. The value of this parameter was varied between 1 and 10 to simulate single cycles and 10 cycles at once.

A limitation of this factor is the total computation time. So if individual cycles are desired there is a limited amount of cycles that can be evaluated. Therefore, this parameter is changed in correspondence with the total number of cycles parameter.

Unfortunately due to the complexity of the model and the time constraints that are associated with this thesis the model has so far not been able to generate results that could be used in this research.

8 Discussion

The results of this research suggest that hydrogenated amorphous silicon carbide (a-SiC$_x$:H) could be used as an anode material in batteries. However, more research is required to validate this and to find a material composition that can retain its capacity even better. To find this material composition multiple anodes will need to be cycled.

The results of this research indicate that the sample with a carbon concentration of 8% and a porosity of 29% had the highest capacity retention, while the sample with a carbon concentration of 0.2% and porosity of 11% had the lowest retention of capacity.

The capacity retention of the battery as a whole, a-SiC$_x$:H and carbon fiber paper (CFP), is displayed in Figure 50. These cycles are chosen because all samples still have significant capacity during cycle 64, the capacity of the sample with 0.2% carbon concentration depletes to a marginal capacity in the following cycles. This fade in capacity is not representative when compared to the first 60 cycles, making a comparison in the retention of capacity unfair. The capacity retention is defined as the fraction of capacity that is retained from the fifth to the 64th cycle. From this figure, it can be deduced that an increase in carbon concentration in the sample increases the capacity retention. The data displayed is that of the first 60 cycles after which the initial capacity is assumed to be stable, being after 5 cycles.

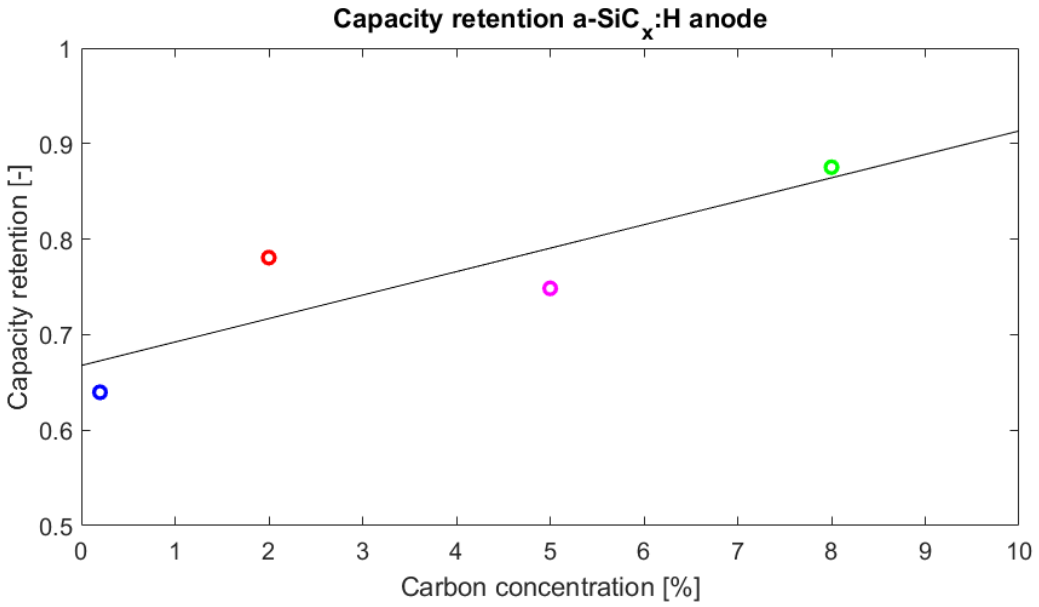

Figure 50: The capacity retention as a function of carbon concentrations from cycles 5 - 64.

With this increase in carbon concentration, the porosity of the material is also increased, experimental work by Wang [38] concluded that porosity has marginal effect on the capacity. However the experimental work in that research was limited, so in this work the possible effect of increased capacity retention by increased porosity is taken into account. Therefore the increase in capacity retention cannot be fully attributed to the increase in carbon concentration. The capacity retention as a function of porosity is displayed in Figure 51. In this figure, a similar ascending trend is visualized as was seen in the relation between capacity retention and carbon concentration. Because of time constraints, the individual effect of either an increase in carbon concentration or an increase in porosity could not be determined experimentally.

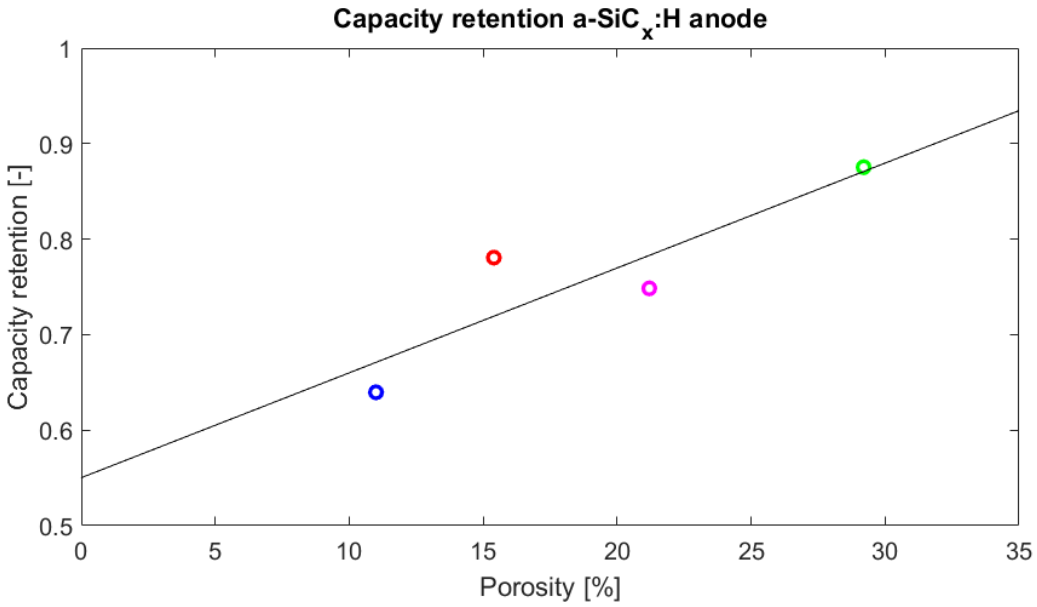

Figure 51: The capacity retention as a function of porosity from cycles 5 - 64.

In Figure 52 the trend of increased capacity retention is also visualized for the retention of the **specific** capacity of the different samples. From the figure, it can be deduced that the specific capacity retention follows a linear relation with increasing carbon concentration. Thereby suggesting that this capacity retention increases with increasing carbon concentration. Furthermore, it can be seen that there is less deviation of the trendline. This can be attributed to the exclusion of the carbon fiber paper (CFP) substrate, which was taken into account in the total capacity retention. These data are in agreement with Huang et al.[41] who showed that the addition of carbon to silicon increases the capacity retention from 5.2% to 41% after 100 cycles at 0.3C.

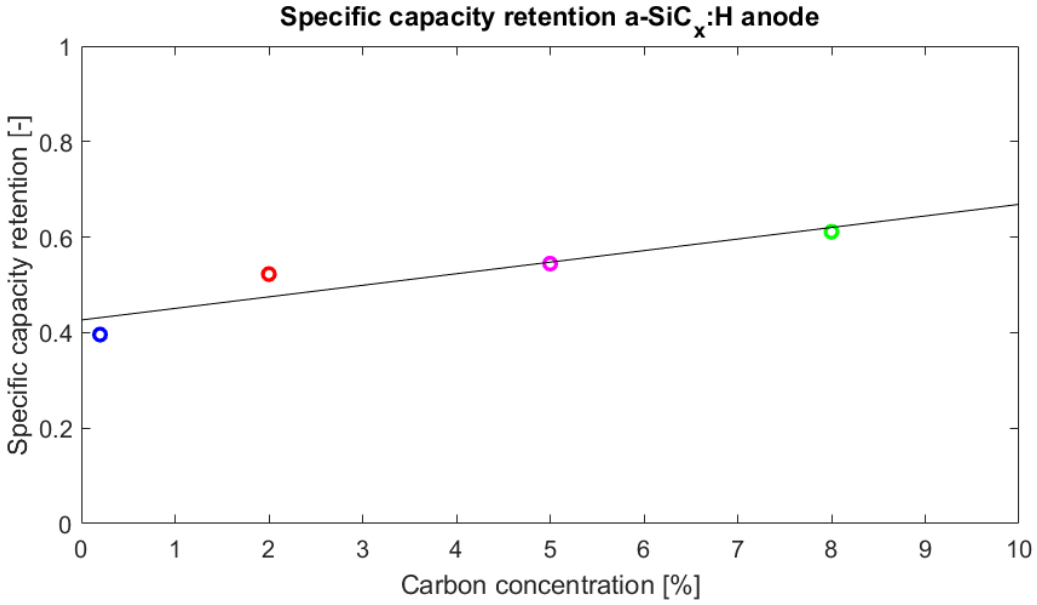

Figure 52: The specific capacity retention as a function of carbon concentrations from cycles 5 - 64.

The same trend of specific capacity retention also holds for the retention based on the porosity of the sample. Once again the relation of the specific capacity retention follows a linearly ascending trendline. Like the specific capacity retention based on the variation carbon concentration, the data follows the linear trend more closely compared to the trend of the whole battery.

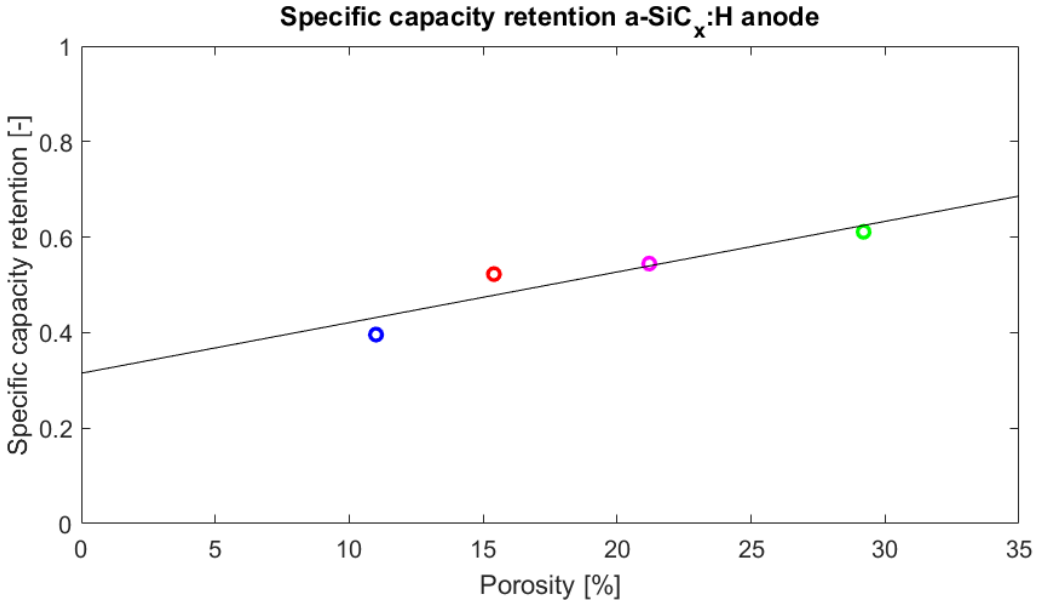

Figure 53: The specific capacity retention as a function of porosity from cycles 5 - 64.

To isolate the effect of a varying porosity simulations can be performed. Simulation results from Wang [38] indicate that an increase in porosity from 15% to 25% results in an increase in capacity retention of 7%. Furthermore, research by Mingyuan et al. [32] indicated that silicon nano-wire samples with high porosity and high pore size could retain specific capacities above 2000 mAh/g. Thereby indicating the importance of a high porosity for stable cycling performance.

Since the individual effect of porosity has not been experimentally verified conclusions about the individual effects can not be made. However, literature findings indicate that both the addition of carbon and high porosity in the material gives rise to increased capacity retention.

The results of this research can be further refined in the future by cycling additional samples in an orthogonal manner. The effect of the carbon concentration can be evaluated by creating and testing samples with varying carbon concentrations while keeping a similar porosity. However, not only the individual effect of the different carbon concentrations and porosity values are improvements to this research.

9 Conclusion and Outlook

During this research, multiple tests have been performed to evaluate the potential of hydrogenated amorphous silicon carbide (a-SiC$_x$:H) as an anode material. a-SiC$_x$:H compositions containing 0.2% up to 8% carbon concentration have been tested at C-rates varying from 0.1C up to 1C. During these tests the a-SiC$_x$:H anode was part of a coin-cell battery which was tested in a half-cell test configuration, thereby pairing the deposited a-SiC$_x$:H cathode with a lithium metal plate anode. This tested the sole performance of the a-SiC$_x$:H electrode since the lithium-metal electrode was not a limiting factor in the capacity.

The study on the rate capability showed that the a-SiC$_x$:H deposited on carbon fiber paper (CFP) can be cycled at various C-rates. When this rate is increased the capacity that can be stored in the battery decreases. After cycling at 1C the batteries were cycled at 0.1C again which resulted in a restored capacity, with only a 5% loss during the 0.1C cycles before and after cycling with the higher C-rates. The low capacity values that were measured during the cycling at 1C were a result of the rate of charging and discharging. The structural changes during this high charging and discharging rates (0.5C and 1C) were limited because the capacity that was measured during the last 0.1C cycles was comparable to the initial 0.1C cycles.

Besides testing the batteries at various rates the stability of the material is evaluated. After 100 cycles at 0.3C, the battery with the best capacity retention was the sample of 8% carbon concentration with a porosity of 29%, while the capacity fade was the greatest in the 0.2% carbon concentration sample with a porosity of 11%.

With an increase in carbon concentration, the porosity of the sample increases with a similar trend. Therefore the capacity retention can not be solely attributed to the increase in carbon concentration.

Furthermore, the charging and discharging curves of the batteries have been analyzed. The bare CFP has a charging voltage window of 0.1 V to 0.3 V. This is extended for the CFP with deposited a-SiC$_x$:H to a charging voltage window of 0.1 V to 0.6 V. This voltage window is constant during cycling. However, when cycles have passed the amount of lithium ions that were stored in the a-SiC$_x$:H cathode decreased, resulting in a decrease in capacity of the battery.

The results of this work can be refined in several ways, this was not possible during this research because of time and resource limitations, but can provide insights for future research in this topic.

First, the results that were obtained during this research were obtained by single coin cell battery tests. The results were verified by a second set of batteries, thereby ensuring that the trend in capacity fade was similar to the initial set of results. However, two batteries are still too small of a sample size to make definitive conclusions about absolute values in the capacity fade. Initial conclusions about global trends such as the capacity fade over 100 cycles can however be made.

Besides that, several different mass-loads of a-SiC$_x$:H should be tested. In the current test setup, the capacity of the batteries is predominantly based on the capacity of the CFP substrate. When the mass loading is increased this will shift the capacity contributions of the sample. This increase in mass loading would affect the rate of cycling of the battery when the capacity of the a-SiC$_x$:H starts to fade. Besides depositing higher mass loadings of a-SiC$_x$:H, another option is to deposit the a-SiC$_x$:H on a substrate without electrochemical capacity, for example copper foil. In this way, the change in the capacity of the a-SiC$_x$:H can be evaluated more precisely.

Furthermore, it must be noted that the ambient conditions during which the batteries were cycled varied between samples since the batteries were not cycled in a climate-controlled room. Not all batteries were cycled at the same time so individual conditions will vary between samples. These varying conditions should be monitored or the batteries should be cycled at constant conditions to remove these variations.

Lastly, the batteries in this research were cycled 100 times at 0.3C. Most battery applications require varying charge and discharge rates and a stable capacity for more than 100 cycles. The effect of extended stability cycling and cycling with a multitude of different currents would give insights into the capacity retention for everyday use.

References

[1] S.-B. Tsai, Y. Xue, J. Zhang, Q. Chen, Y. Liu, J. Zhou, and W. Dong, "Models for forecasting growth trends in renewable energy," *Renewable and Sustainable Energy Reviews*, vol. 77, pp. 1169–1178, 2017.

[2] I. G. R. Outlook, "Energy transformation 2050," *IRENA: Abu Dhabi, UAE*, 2020.

[3] A. Schröder, F. Kunz, J. Meiss, R. Mendelevitch, and C. Von Hirschhausen, "Current and prospective costs of electricity generation until 2050," tech. rep., DIW data documentation, 2013.

[4] H. L. Ferreira, R. Garde, G. Fulli, W. Kling, and J. P. Lopes, "Characterisation of electrical energy storage technologies," *Energy*, vol. 53, pp. 288–298, 2013.

[5] L. Urbanucci, F. D'Ettorre, and D. Testi, "A comprehensive methodology for the integrated optimal sizing and operation of cogeneration systems with thermal energy storage," *Energies*, vol. 12, no. 5, p. 875, 2019.

[6] T. Li, R. Wang, J. K. Kiplagat, and Y. Kang, "Performance analysis of an integrated energy storage and energy upgrade thermochemical solid–gas sorption system for seasonal storage of solar thermal energy," *Energy*, vol. 50, pp. 454–467, 2013.

[7] A. Züttel, A. Remhof, A. Borgschulte, and O. Friedrichs, "Hydrogen: the future energy carrier," *Philosophical Transactions of the Royal Society A: Mathematical, Physical and Engineering Sciences*, vol. 368, no. 1923, pp. 3329–3342, 2010.

[8] *Lithium ion battery schematic*, 2021.

[9] J. W. Fergus, "Recent developments in cathode materials for lithium ion batteries," *Journal of power sources*, vol. 195, no. 4, pp. 939–954, 2010.

[10] M. Yoshio, H. Wang, and K. Fukuda, "Spherical carbon-coated natural graphite as a lithium-ion battery-anode material," *Angewandte Chemie International Edition*, vol. 42, no. 35, pp. 4203–4206, 2003.

[11] P. Lian, X. Zhu, S. Liang, Z. Li, W. Yang, and H. Wang, "Large reversible capacity of high quality graphene sheets as an anode material for lithium-ion batteries," *Electrochimica Acta*, vol. 55, no. 12, pp. 3909–3914, 2010.

[12] A. Casimir, H. Zhang, O. Ogoke, J. C. Amine, J. Lu, and G. Wu, "Silicon-based anodes for lithium-ion batteries: Effectiveness of materials synthesis and electrode preparation," *Nano Energy*, vol. 27, pp. 359–376, 2016.

[13] R. Wang, W. Cui, F. Chu, and F. Wu, "Lithium metal anodes: Present and future," *Journal of Energy Chemistry*, vol. 48, pp. 145–159, 2020.

[14] S. J. An, J. Li, C. Daniel, D. Mohanty, S. Nagpure, and D. Wood, "Cheminform abstract: The state of understanding of the lithium-ion-battery graphite solid electrolyte interphase (sei) and its relationship to formation cycling," *ChemInform*, vol. 47, 06 2016.

[15] M. S. Dresselhaus, G. Dresselhaus, P. Eklund, and A. Rao, "Carbon nanotubes," in *The physics of fullerene-based and fullerene-related materials*, pp. 331–379, Springer, 2000.

[16] H.-Q. Li, R.-L. Liu, D.-Y. Zhao, and Y.-Y. Xia, "Electrochemical properties of an ordered mesoporous carbon prepared by direct tri-constituent co-assembly," *Carbon*, vol. 45, no. 13, pp. 2628–2635, 2007.

[17] Y. Zhao, L. P. Wang, M. T. Sougrati, Z. Feng, Y. Leconte, A. Fisher, M. Srinivasan, and Z. Xu, "A review on design strategies for carbon based metal oxides and sulfides nanocomposites for high performance li and na ion battery anodes," *Advanced Energy Materials*, vol. 7, no. 9, p. 1601424, 2017.

[18] J. Ni, Y. Huang, and L. Gao, "A high-performance hard carbon for li-ion batteries and supercapacitors application," *Journal of Power Sources*, vol. 223, pp. 306–311, 2013.

[19] F.-M. Wang, M.-H. Yu, Y.-J. Hsiao, Y. Tsai, B.-J. Hwang, Y.-Y. Wang, and C.-C. Wan, "Aging effects to solid electrolyte interface (sei) membrane formation and the performance analysis of lithium ion batteries," *Int. J. Electrochem. Sci*, vol. 6, no. 1014, p. e1026, 2011.

[20] X.-B. Cheng, R. Zhang, C.-Z. Zhao, F. Wei, J.-G. Zhang, and Q. Zhang, "A review of solid electrolyte interphases on lithium metal anode," *Advanced science*, vol. 3, no. 3, p. 1500213, 2016.

[21] M. B. Pinson and M. Z. Bazant, "Theory of sei formation in rechargeable batteries: capacity fade, accelerated aging and lifetime prediction," *Journal of the Electrochemical Society*, vol. 160, no. 2, p. A243, 2012.

[22] K. Xu, "Nonaqueous liquid electrolytes for lithium-based rechargeable batteries," *Chemical reviews*, vol. 104, no. 10, pp. 4303–4418, 2004.

[23] Y.-P. Wu, C.-R. Wan, C.-Y. Jiang, S.-B. Fang, and Y.-Y. Jiang, "Mechanism of lithium storage in low temperature carbon," *Carbon*, vol. 37, no. 12, pp. 1901–1908, 1999.

[24] Y. Wu, E. Rahm, and R. Holze, "Carbon anode materials for lithium ion batteries," *Journal of power sources*, vol. 114, no. 2, pp. 228–236, 2003.

[25] D. Zhang, S. Zhang, Y. Jin, T. Yi, S. Xie, and C. Chen, "Li2sno3 derived secondary li–sn alloy electrode for lithium-ion batteries," *Journal of alloys and compounds*, vol. 415, no. 1-2, pp. 229–233, 2006.

[26] C. Liang, M. Gao, H. Pan, Y. Liu, and M. Yan, "Lithium alloys and metal oxides as high-capacity anode materials for lithium-ion batteries," *Journal of alloys and compounds*, vol. 575, pp. 246–256, 2013.

[27] C.-H. Doh, J.-S. Kim, B.-S. Jin, and S.-I. Moon, "Lithium alloying potentials of silicon as anode of lithium secondary batteries," in *Proceedings of International Meeting on Lithium Batteries.(June 27–July 2, 2010, Montreal, Canada).–Abstr*, vol. 42, 2010.

[28] A. Franco Gonzalez, N.-H. Yang, and R.-S. Liu, "Silicon anode design for lithium-ion batteries: progress and perspectives," *The Journal of Physical Chemistry C*, vol. 121, no. 50, pp. 27775–27787, 2017.

[29] M. Ashuri, Q. He, and L. L. Shaw, "Silicon as a potential anode material for li-ion batteries: where size, geometry and structure matter," *Nanoscale*, vol. 8, no. 1, pp. 74–103, 2016.

[30] S. P. Nadimpalli, V. A. Sethuraman, S. Dalavi, B. Lucht, M. J. Chon, V. B. Shenoy, and P. R. Guduru, "Quantifying capacity loss due to solid-electrolyte-interphase layer formation on silicon negative electrodes in lithium-ion batteries," *Journal of Power Sources*, vol. 215, pp. 145–151, 2012.

[31] N. Liu, Z. Lu, J. Zhao, M. T. McDowell, H.-W. Lee, W. Zhao, and Y. Cui, "A pomegranate-inspired nanoscale design for large-volume-change lithium battery anodes," *Nature nanotechnology*, vol. 9, no. 3, pp. 187–192, 2014.

[32] M. Ge, J. Rong, X. Fang, and C. Zhou, "Porous doped silicon nanowires for lithium ion battery anode with long cycle life," *Nano letters*, vol. 12, no. 5, pp. 2318–2323, 2012.

[33] Z. Lu, N. Liu, H.-W. Lee, J. Zhao, W. Li, Y. Li, and Y. Cui, "Nonfilling carbon coating of porous silicon micrometer-sized particles for high-performance lithium battery anodes," *ACS nano*, vol. 9, no. 3, pp. 2540–2547, 2015.

[34] A. Franco Gonzalez, N.-H. Yang, and R.-S. Liu, "Silicon anode design for lithium-ion batteries: Progress and perspectives," *The Journal of Physical Chemistry C*, vol. 121, no. 50, pp. 27775–27787, 2017.

[35] M. Raić, L. Mikac, I. Marić, G. Štefanić, M. Škrabić, M. Gotić, and M. Ivanda, "Nanostructured silicon as potential anode material for li-ion batteries," *Molecules*, vol. 25, no. 4, p. 891, 2020.

[36] T. D. Bogart, X. Lu, M. Gu, C. Wang, and B. A. Korgel, "Enhancing the lithiation rate of silicon nanowires by the inclusion of tin," *RSC Adv.*, vol. 4, pp. 42022–42028, 2014.

[37] Y. Zhang, X. Zhang, H. Zhang, Z. Zhao, F. Li, C. Liu, and H. Cheng, "Composite anode material of silicon/graphite/carbon nanotubes for li-ion batteries," *Electrochimica acta*, vol. 51, no. 23, pp. 4994–5000, 2006.

[38] S. Wang, "Study of n-type amorphous silicon alloy as the anode in li-ion batteries," Master's thesis, TU Delft, 2020.

[39] S. Janz, *Amorphous silicon carbide for photovoltaic applications*. PhD thesis, 2006.

[40] H. Zhang and H. Xu, "Nanocrystalline silicon carbide thin film electrodes for lithium-ion batteries," *Solid State Ionics*, vol. 263, pp. 23–26, 2014.

[41] X. Huang, F. Zhang, X. Gan, Q. Huang, J. Yang, P. Lai, and W. Tang, "Electrochemical characteristics of amorphous silicon carbide film as a lithium-ion battery anode," *RSC advances*, vol. 8, no. 10, pp. 5189–5196, 2018.

[42] J. Yang, R. C. De Guzman, S. O. Salley, K. S. Ng, B.-H. Chen, and M. M.-C. Cheng, "Plasma enhanced chemical vapor deposition silicon nitride for a high-performance lithium ion battery anode," *Journal of Power Sources*, vol. 269, pp. 520–525, 2014.

[43] S. Gani, "Analysis of porosity on the discharge of silicon-air batteries," Master's thesis, TU Delft, 2021.

[44] Q. Si, M. Matsui, T. Horiba, O. Yamamoto, Y. Takeda, N. Seki, and N. Imanishi, "Carbon paper substrate for silicon–carbon composite anodes in lithium-ion batteries," *Journal of power sources*, vol. 241, pp. 744–750, 2013.

[45] D. Wang, W. Liu, X. Zhang, Y. Huang, M. Xu, and W. Xiao, "Review of modified nickel-cobalt lithium aluminate cathode materials for lithium-ion batteries," *International Journal of Photoenergy*, vol. 2019, 2019.

[46] N. P. Wagner, K. Asheim, F. Vullum-Bruer, and A. M. Svensson, "Performance and failure analysis of full cell lithium ion battery with lini0. 8co0. 15al0. 05o2 and silicon electrodes," *Journal of Power Sources*, vol. 437, p. 226884, 2019.

[47] C. R. Birkl, E. McTurk, M. Roberts, P. G. Bruce, and D. A. Howey, "A parametric open circuit voltage model for lithium ion batteries," *Journal of The Electrochemical Society*, vol. 162, no. 12, p. A2271, 2015.

[48] J.A. Woollam, Lincoln, USA, *J.A Woollam Ellipsometer M-2000*, manual ed., 2021.

[49] M. Khardani, M. Bouaïcha, and B. Bessaïs, "Bruggeman effective medium approach for modelling optical properties of porous silicon: comparison with experiment," *physica status solidi c*, vol. 4, no. 6, pp. 1986–1990, 2007.

[50] L. Weinstein, "Electromagnetic waves," *Radio i svyaz', Moscow*, 1988.

[51] H. Fujiwara, *Spectroscopic ellipsometry: principles and applications*. John Wiley & Sons, 2007.

[52] J. A. Woollam, B. D. Johs, C. M. Herzinger, J. N. Hilfiker, R. A. Synowicki, and C. L. Bungay, "Overview of variable-angle spectroscopic ellipsometry (vase): I. basic theory and typical applications," in *Optical Metrology: A Critical Review*, vol. 10294, p. 1029402, International Society for Optics and Photonics, 1999.

[53] G. A. Niklasson, C. Granqvist, and O. Hunderi, "Effective medium models for the optical properties of inhomogeneous materials," *Applied Optics*, vol. 20, no. 1, pp. 26–30, 1981.

[54] J. Li, L. Wang, X. He, and J. Wang, "Effect of pore size distribution of carbon matrix on the performance of phosphorus@ carbon material as anode for lithium-ion batteries," *ACS Sustainable Chemistry & Engineering*, vol. 4, no. 8, pp. 4217–4223, 2016.

[55] D. F. Edwards and E. Ochoa, "Infrared refractive index of silicon," *Applied optics*, vol. 19, no. 24, pp. 4130–4131, 1980.

[56] M. E. Levinshtein, S. L. Rumyantsev, and M. S. Shur, *Properties of Advanced Semiconductor Materials: GaN, AIN, InN, BN, SiC, SiGe*. John Wiley & Sons, 2001.

[57] A. Sproul and M. Green, "Improved value for the silicon intrinsic carrier concentration from 275 to 375 k," *Journal of applied physics*, vol. 70, no. 2, pp. 846–854, 1991.

[58] R. C. Dorf, *CRC handbook of engineering tables*. CRC Press, 2003.

[59] Armgate, Latvia, *Ultra-high Resolution Scanning Electron Microscope REGULUS Series*, manual ed., 2021.

[60] C. Scordilis-Kelley and R. T. Carlin, "Lithium and sodium standard reduction potentials in ambient-temperature chloroaluminate molten salts," *Journal of the Electrochemical Society*, vol. 140, no. 6, p. 1606, 1993.

[61] C. Chen, P. Li, T. Wang, S. Wang, and M. Zhang, "S-doped carbon fibers uniformly embedded with ultrasmall tio2 for na+/li+ storage with high capacity and long-time stability," *Small*, vol. 15, no. 38, p. 1902201, 2019.

[62] "Bond Enthalpies," aug 22 2020. [Online; accessed 2021-10-18].

[63] P. Timms, "The chemistry of volatile waste from silicon wafer processing," *Journal of the Chemical Society, Dalton Transactions*, no. 6, pp. 815–822, 1999.

[64] J. Hagberg, S. Leijonmarck, and G. Lindbergh, "High precision coulometry of commercial pan-based carbon fibers as electrodes in structural batteries," *Journal of The Electrochemical Society*, vol. 163, no. 8, p. A1790, 2016.

[65] J. R. Szczech and S. Jin, "Nanostructured silicon for high capacity lithium battery anodes," *Energy & Environmental Science*, vol. 4, no. 1, pp. 56–72, 2011.

[66] K. Qian, C. Zhou, Y. Yuan, and M. Allan, "Temperature effect on electric vehicle battery cycle life in vehicle-to-grid applications," in *CICED 2010 Proceedings*, pp. 1–6, IEEE, 2010.

[67] COMSOL Myltiphysics, United States, *Capacity Fade of a Lithium-Ion Battery*, manual ed., 2021.

[68] COMSOL Myltiphysics, United States, *Lithium-Ion Battery with Multiple Intercalating Electrode Materials*, manual ed., 2021.

[69] H. Ekström and G. Lindbergh, "A model for predicting capacity fade due to sei formation in a commercial graphite/lifepo4 cell," *Journal of The Electrochemical Society*, vol. 162, no. 6, p. A1003, 2015.

[70] P. Kar and J. W. Evans, "A model for the electrochemical reduction of metal oxides in molten salt electrolytes," *Electrochimica acta*, vol. 54, no. 2, pp. 835–843, 2008.

[71] M. Doyle, T. F. Fuller, and J. Newman, "Modeling of galvanostatic charge and discharge of the lithium/polymer/insertion cell," *Journal of the Electrochemical society*, vol. 140, no. 6, p. 1526, 1993.

[72] R. Chandrasekaran and T. F. Fuller, "Analysis of the lithium-ion insertion silicon composite electrode/separator/lithium foil cell," *Journal of The Electrochemical Society*, vol. 158, no. 8, p. A859, 2011.

[73] S. Dhillon, G. Hernández, N. P. Wagner, A. M. Svensson, and D. Brandell, "Modelling capacity fade in silicon-graphite composite electrodes for lithium-ion batteries," *Electrochimica Acta*, vol. 377, p. 138067, 2021.